

Subaru weak-lensing mass measurement  
of a high-redshift SZ cluster  
ACT-CL J0022–0036 discovered  
by the Atacama Cosmology Telescope Survey

Hironao Miyatake  
Department of Physics, University of Tokyo

December 2011

## Abstract

Several optical surveys aiming to improve cosmological parameters will be carried out within the next few years. Among them, Hyper Suprime-Cam (HSC), the next-generation prime focus camera of the Subaru Telescope, will open a window to explore the universe through weak lensing (WL) measurements. One promising cosmological probe is cluster abundance that will be measurable by combining Atacama Cosmology Telescope (ACT), the millimeter-wave Sunyaev-Zel'dovich (SZ) survey, with the HSC survey. For this, it is important to observationally study scaling relations between the SZ effect and WL mass estimates. One concern is that the WL mass measurement of high-redshift clusters is not yet established by using the data of Suprime-Cam, the current prime focus camera of the Subaru Telescope.

We carried out follow-up observations of ACT-CL J0022-0036 through the Suprime-Cam. This cluster was discovered in 200-deg<sup>2</sup> of early data from equatorial region of the ACT Survey through the SZ effect. The cluster has the strongest SZ signal in the survey region, and lies at  $z = 0.81$ . Thus this cluster is suitable to test the feasibility of WL measurements of high-redshift clusters.

For data analysis, we use a suite of new data reduction software and WL measurement algorithms which are being developed for the HSC. Photometric redshifts are used for a clean separation of background galaxies from cluster members and foreground galaxies. The total signal-to-noise ratio of WL signal against statistical error is about 3.6, showing significant detection despite such a high-redshift cluster using ground-based data.

After careful investigation of systematic uncertainties, we obtain the mass of the cluster, which is defined as the three-dimensional mass within a spherical region of a given radius inside of which the mean interior density is 200 times the mean mass density, as

$$M_{200} = (0.72^{+0.33}_{-0.27}(\text{stat.})^{+0.12}_{-0.06}(\text{syst.})) \times 10^{15} M_{\odot}/h.$$

The result of our study has proved that WL mass measurements of high-redshift galaxy clusters are possible and provides the first step to improve cosmological constraints with survey data of the ACT and HSC in the future.

We also test the  $\Lambda$ CDM paradigm through the mass of the high-redshift massive cluster. We find that this high-redshift massive cluster is consistent with the  $\Lambda$ CDM.

# Acknowledgement

First of all, I would like to express my sincere appreciation to Prof. H. Aihara, for giving me a great opportunity to work on this research and his important supervision. His enthusiasm ranging from particle physics to cosmology inspired me a lot.

I am indebted to Prof. M. Yokoyama and Prof. Y. Onuki for their helpful advice. I enjoyed discussions with Mr. S. Mineo about cosmology and weak lensing measurements. Mr. C. Ng kindly corrected my English in this thesis. I am grateful to the other members, students and alumni of our group for my daily life in Hongo: Prof. M. Iwasaki, Prof. H. Kakuno, Dr. T. Abe, Dr. D. Epifanov, Dr. N. Hastings, Dr. T. Uchida, and Ms. K. Kono: Mr. J. Wang, Mr. Y. Kanazawa, Dr. A. Kusaka, Dr. K. Tanabe, Dr. Y. Nakahama, Dr. H. Nakayama, Mr. K. Yamada, Mr. H. Fujimori, and Mr. S. Sugihara.

I would like to express my great gratitude to members in the Institute for the Physics and Mathematics of the Universe (IPMU). Especially, Prof. M. Takada taught me the basics about cosmology and patiently discussed with me shape measurement and data analysis. Prof. N. Yasuda kindly taught me the basics of data reduction with the HSC pipeline, and Dr. A. Nishizawa worked with me on photometric redshift measurements of this research. Dr. M. Tanaka, Prof. K. Bundy, and Dr. A. Leauthaud gave me useful ideas on the photometric redshift measurement. I enjoyed discussion with Prof. M. Oguri about weak lensing measurements. I thank to students and alumni in IPMU: Dr. T. Nishioka, Dr. T. Kobayashi, Dr. W. Klemm, Dr. S. Mandel, Mr. R. Nishio, Mr. K. Tobioka, Mr. Y. Kamiya, Mr. A. Kamada, Mr. T. Moriya, Mr. K. Nakajima, Mr. T. Ugajin, Mr. K. Harigaya, Mr. T. Fujita, Mr. G. Chiaki, Mr. M. Shirasaki, and Mr. W. Yin.

I am deeply grateful to members in the Department of Astrophysical Sciences, Princeton University. Dr. R. Mandelbaum patiently discussed with me shape measurement and data analysis. The Princeton software team consisting of Dr. R. Lupton, Dr. C. Loomis, Dr. S. Bickerton, Dr. P. Price, Dr. D. Lang, and Dr. J. Bosch provided me the HSC pipeline and kindly discussed with me how to improve the pipeline. I thank Prof. J. Gunn, Prof. M. Strauss, and Prof. D. Spergel for their great advice. All the Princeton members kindly allowed me to visit frequently,

and supported my life in Princeton.

In this thesis I used SDSS-III data. Funding for SDSS-III has been provided by the Alfred P. Sloan Foundation, the Participating Institutions, the National Science Foundation, and the U.S. Department of Energy Office of Science. The SDSS-III web site is <http://www.sdss3.org/>. SDSS-III is managed by the Astrophysical Research Consortium for the Participating Institutions of the SDSS-III Collaboration including the University of Arizona, the Brazilian Participation Group, Brookhaven National Laboratory, University of Cambridge, Carnegie Mellon University, University of Florida, the French Participation Group, the German Participation Group, Harvard University, the Instituto de Astrofísica de Canarias, the Michigan State/Notre Dame/JINA Participation Group, Johns Hopkins University, Lawrence Berkeley National Laboratory, Max Planck Institute for Astrophysics, New Mexico State University, New York University, Ohio State University, Pennsylvania State University, University of Portsmouth, Princeton University, the Spanish Participation Group, University of Tokyo, University of Utah, Vanderbilt University, University of Virginia, University of Washington, and Yale University.

Finally, I am deeply indebted to my family. My parents, Hisatada and Toshiko, gave me the seed from which my interest in science grew and supported my higher education. My brothers, Hiroto and Hiromasa, always cheered me up. Without them I could not have accomplished this work.

# Contents

<b>1</b>	<b>Introduction</b>	<b>13</b>
<b>2</b>	<b>Cluster Cosmology and Weak Lensing Mass Measurement</b>	<b>17</b>
2.1	$\Lambda$ CDM Model . . . . .	17
2.1.1	Smooth, Expanding Universe . . . . .	17
2.1.2	Structure Formation . . . . .	21
2.2	Testing $\Lambda$ CDM Model with a Massive, High-redshift Cluster . . . . .	23
2.2.1	Theory . . . . .	23
2.2.2	Sample Selection . . . . .	27
2.2.3	Cluster Mass Indicators . . . . .	29
2.3	Estimation of Cluster Mass through Weak Lensing . . . . .	29
2.3.1	Basics of Weak Lensing . . . . .	29
2.3.2	Cluster Mass Reconstruction . . . . .	32
<b>3</b>	<b>Observational Apparatus</b>	<b>35</b>
3.1	Subaru Telescope . . . . .	35
3.2	Suprime-Cam . . . . .	39
3.2.1	Overview . . . . .	39
3.2.2	CCD and Electronics . . . . .	42
<b>4</b>	<b>Development of High Precision Weak Lensing Measurement Algorithm</b>	<b>49</b>
4.1	General Description of Weak Lensing Measurement . . . . .	49
4.1.1	Measuring Ellipticity of Each Galaxy Image . . . . .	49
4.1.2	Extracting Weak Lensing Signal . . . . .	50
4.2	Overview of High Precision Weak Lensing Measurement Algorithm . . . . .	53
4.2.1	Gauss-Laguerre Basis Functions . . . . .	53
4.2.2	Modelling PSF . . . . .	54
4.2.3	Modelling Galaxy to Extract Shear Estimator . . . . .	56
4.2.4	Covariance and Signal-to-noise Ratio . . . . .	59
4.2.5	Summary of Elliptical Gauss-Laguerre Method . . . . .	59

4.3	Testing the Weak Lensing Measurement Algorithm . . . . .	60
4.3.1	Ring Test . . . . .	60
4.3.2	Image Simulation . . . . .	61
4.3.3	Results . . . . .	64
<b>5</b>	<b>Mass measurement of the High-redshift Massive Galaxy Cluster</b>	
	<b>ACT-CL J0022-0036</b>	<b>74</b>
5.1	Data . . . . .	74
5.2	Analysis Overview . . . . .	75
5.3	Data Reduction . . . . .	78
5.3.1	Data Format of HSC Pipeline . . . . .	78
5.3.2	Chip-based Data Reduction . . . . .	78
5.3.3	Image Stacking . . . . .	84
5.4	Photometry and Redshift Estimation . . . . .	86
5.4.1	Photometry . . . . .	87
5.4.2	Photometric Redshift . . . . .	89
5.5	Weak Lensing Analysis . . . . .	93
5.5.1	Simultaneous Multiple-exposure Analysis . . . . .	93
5.5.2	PSF Determination . . . . .	96
5.5.3	Star/galaxy Separation . . . . .	104
5.5.4	Residual Correlation . . . . .	104
5.6	Mass Reconstruction . . . . .	108
5.6.1	Model-dependent Estimate of Cluster Mass . . . . .	108
5.6.2	Results . . . . .	110
5.6.3	Validity Check for Error Bars . . . . .	111
5.6.4	Systematic Uncertainties . . . . .	116
<b>6</b>	<b>Discussion</b>	<b>123</b>
6.1	Comparison with Previous High-redshift Cluster Lensing Measurement	123
6.2	Concentration Parameter . . . . .	124
6.3	Systematic Uncertainties from Physics . . . . .	125
6.3.1	Halo Triaxiality . . . . .	125
6.3.2	Off-Centering Effect . . . . .	125
6.3.3	Projection Effect . . . . .	126
6.4	Comparison with Observation by Sunyaev-Zel'dovich Array . . . . .	127
6.5	Scaling Relation . . . . .	128
6.6	Cosmological Implications . . . . .	129
6.6.1	Exclusion Curve . . . . .	129
6.6.2	Comparison with previous works . . . . .	131
<b>7</b>	<b>Conclusions</b>	<b>134</b>

<b>A</b>	<b>Hyper Suprime-Cam</b>	<b>136</b>
<b>B</b>	<b>Details of Elliptical Gauss-Laguerre Method</b>	<b>138</b>
	B.1 Rising and Lowering Operator for Gauss-Laguerre Function . . . . .	139
	B.2 Convolution Matrix for Gauss Laguerre Function . . . . .	139
	B.3 Transformation Matrices . . . . .	141
	B.4 Formulae of Transformation Matrices . . . . .	143
	B.4.1 Dilution . . . . .	143
	B.4.2 Shear . . . . .	144
<b>C</b>	<b>Sunyaev-Zel'dovich Effect</b>	<b>148</b>
	C.1 What is the Sunyaev-Zel'dovich Effect? . . . . .	148
	C.2 Atacama Cosmology Telescope . . . . .	151

# List of Figures

2.1	The three sets of points denote measured mass function with $\Delta = 200$ , 800, and 3200 (from top to bottom) for simulations based on WMAP first year results. Solid curves denote mass function Tinker et al. [95] derived. This figure is taken from Tinker et al. [95]. . . . .	24
2.2	$M$ - $z$ exclusion curves taken from Mortonson et al. [62] and slightly modified. Even a single massive cluster above the curve falsifies the $\Lambda$ CDM model at 95% CL. <i>upper panel</i> : The exclusion curve in three cases of sky coverage. <i>lower panel</i> : Observed cluster mass with the exclusion curve of 300-deg <sup>2</sup> ; SPT-CL J0546-5345 ( $M_{200} = (8.23 \pm 1.21) \times 10^{14} M_{\odot}$ ) and XMMU J2235.3-2557 ( $M_{200} = 7.7_{-3.1}^{+4.4} \times 10^{14} M_{\odot}$ ). Red open points are without Eddington bias correction, and black solid points are with Eddington bias correction. . . . .	26
2.3	Sensitivity maps around an equatorial region surveyed by the ACT. This figure is taken from Hand et al. [31]. The gray-scale encodes the noise rms in $\mu$ K of a map match-filtered for cluster detection. Red point shows a position of luminous red galaxy that is irrelevant to our study. . . . .	28
2.4	Typical weak lensing system in the limit of thin lens approximation. This figure is taken from Bartelmann and Schneider [9] and slightly modified. . . . .	30
2.5	Illustration of how WL maps a source. . . . .	32
2.6	Definition of E-mode and B-mode. . . . .	33
3.1	Schematic view of structure of Subaru Telescope. . . . .	36
3.2	Indicative reflectivity of primary mirror, which is actually measured from microscope mirrors coated in the same condition as primary mirror in August, 2010. . . . .	37
3.3	Picture of actuators which actively support the primary mirror. . . . .	37
3.4	Aerial view of Subaru enclosure. . . . .	38

3.5	Seeing statistics measured by auto guider camera. The squares, triangles, circles show the measurement time before 21:00, 21:00-26:00, and after 26:00 Hawaiian standard time, respectively. The data was taken from May 2000 to Nov. 2008. . . . .	39
3.6	Atmospheric transmittance curve at the summit of Mauna Kea when airmass is 1.2. . . . .	40
3.7	Picture of Suprime-Cam. . . . .	41
3.8	Schematic of Suprime-Cam. . . . .	43
3.9	Transmittance of wide field corrector. . . . .	44
3.10	Actual filter response of Suprime-Cam. ( <i>left</i> ): $B, V, R_c, I_c$ from the Johnson-Morgan-Cousins system. ( <i>right</i> ): $g', r', i', z'$ from the SDSS system. The reddest band $Y$ is added. . . . .	44
3.11	Alignment of CCDs on the focal plane of Suprime-Cam. . . . .	45
3.12	Quantum efficiency of CCD. Solid line denotes quantum efficiency of CCD used by Suprime-Cam which was upgraded in July 2008. This CCD was manufactured by Hamamatsu Photonics K.K. Dashed line denotes quantum efficiency of CCD used by Suprime-Cam before the upgrade, which was manufactured by MIT Lincoln Laboratory. . . . .	46
3.13	Nonlinearity of Suprime-Cam readout system. Dashed line denotes the nonlinearity of MFront2. Solid line denotes nonlinearity combined with a CCD. . . . .	48
4.1	Illustration of forward process. This figure is taken from Bridle et al. [15]. . . . .	50
4.2	Gauss-Laguerre basis functions. They are used for modelling PSF. . . . .	55
4.3	Elliptical Gauss-Laguerre basis functions convolved with PSF that is shown at upper right. They are used for modelling a galaxy. . . . .	57
4.4	PSF profiles. FWHM is fixed to 3.5 pixels over all profiles. For a Moffat profile, $\alpha$ is calculated from the FWHM and $\beta = 4.0$ . For a double Gaussian, $FHWM_1 = 3.5$ pixels, $f_I = 0.1$ , and $f_\alpha = 2.0$ . A Gaussian and a double Gaussian are used for this simulation. . . . .	63
4.5	Exmaples of generated images for ring test. Exponential galaxies whose $r_e = 0.875$ pixel and $e = 0.1$ convolved with circular double Gaussian PSF whose $FHWM_1=3.5$ pixel are shown. Left panel is images without noise, while right panel is images with noise ( $S/N = 20$ ). For each panel, a galaxy whose position angle is 0 deg, 45 deg, 90 deg, and 135 deg is shown in lower left, lower right, upper left, and upper right, respectively. . . . .	65

4.6	Shear recovery accuracy when PSF is Gaussian with FWHM=3.5 pixel as a function of $N_{\text{gal}}$ , the order of GL function used for galaxy fitting. Other parameters of the EGL fit are fixed to $N_{\text{PSF}} = 12$ , $N_{\text{in}} = 20$ , and $f_p = 1.2$ . For galaxy model, exponential profile having various ellipticity and size is used. The half light radius of galaxy is set to half, equal, and one and half of that of PSF (0.875 pixel, 1.750 pixel, and 2.625 pixel, respectively). Input shear to the simulation image is (0.02, 0) as shown in dotted line. . . . .	67
4.7	Same plot as Fig. 4.6, but PSF is double Gaussian profile whose FWHM of the first component is 3.5 pixel. . . . .	68
4.8	Same plot as Fig. 4.7, but $f_p$ is increased to 3.0. . . . .	68
4.9	Same plot as Fig. 4.7, but PSF has anisotropy, $e^* = (0.01, 0)$ . Note that the anisotropy is half of the input shear. . . . .	69
4.10	Same plot as Fig. 4.9, but $f_p$ is increased to 3.0. . . . .	69
4.11	<i>upper panel:</i> A double Gaussian PSF profile (black-bold line) and the residual between PSF modeled by the GLs and the double Gaussain (other thin lines). The former is plotted in log scale as shown in the right vertical axis, while the latter is in linear scale. The double Gaussian profile is normalized by the peak of the profile, and configured with $r_I = 0.1$ , $r_\sigma=2$ , and $\text{FWHM}_1 = 3.5$ pixels. Blue-solid, green-dashed, red-dashed-dotted, cyan-dotted lines show the case of $N_{\text{PSF}}$ is 2,4,6,8, respectively. <i>lower panel:</i> A double Gaussian profile and GL PSF model integrated from the center to radius $r$ . Notations for lines are same as the upper panel. . . . .	71
4.12	Configuration of the galaxy image is same as Fig. 4.7 except that noise is added as described in Section 4.3.2. Parameters of the EGL method are $(N_{\text{gal}}, N_{\text{PSF}}, N_{\text{in}}, f_p) = (2, 8, 12, 1.2)$ . The dots at $S/N = 150$ is not the value obtained by fitting a image with $S/N = 150$ , but that without noise. . . . .	73
4.13	Same plot as Fig. 4.12, but parameters of the EGL method is $(N_{\text{gal}}, N_{\text{PSF}}, N_{\text{in}}, f_p) = (8, 12, 20, 3.0)$ . . . . .	73
5.1	Analysis Overview. . . . .	76
5.2	Example of principal component analysis of PSF. The lower left image is 0th order of principal components which corresponds to mean of data. The order of principal component increases, as an image goes from the lower center to lower right and then from the upper left to upper right. . . . .	82
5.3	One example of reduced image. This image is $\sim 700$ pixel $\times$ $\sim 450$ pixel of the center part of chip ID = 126932. For details about colors and numbers, see text. . . . .	85

5.4	RGB image of ACTJ0022 which consists of $r'i'z'$ stacked images processed by the HSC pipeline. $\sim 8 \times \sim 8$ arcmin <sup>2</sup> region around the center is trimmed. . . . .	86
5.5	The scatter plot between photometric and true redshift. Blue and green dots denote the scatter before and after magnitude zeropoint calibration, respectively. . . . .	92
5.6	Redshift distribution of our field after objects whose flux in 3'' aperture is 5 times larger than its error are selected. . . . .	93
5.7	Color-magnitude diagram of the center part of our image. The region enclosed by red lines denote bright end of red sequence of ACTJ0022. . . . .	94
5.8	Redshift distribution of the red sequence selected in Fig. 5.7. . . . .	95
5.9	Stellar ellipticity and size across chips of exposure ID = 126932. . . . .	99
5.10	PSF ellipticity and size across chips of exposure ID = 126932. . . . .	100
5.11	Residual ellipticity and size between stars and PSF across chips of exposure ID = 126932. . . . .	101
5.12	Ellipticity distribution on chips of exposure ID = 126932. Blue dots denote stellar ellipticity and green dots denote residual ellipticity between stars and PSF. . . . .	102
5.13	Correlation between residual ellipticity and stellar ellipticity on chips of exposure ID = 126932. . . . .	103
5.14	Mean ellipticity distribution of all chips used for WL analysis. . . . .	105
5.15	Size-magnitude diagram for star/galaxy separation. . . . .	106
5.16	Residual correlation to test quality of exposure. Since we use ten exposures in total, there are ten cases of residual correlation. Black horizontal line of each correlation shows zero correlation. ID of the removed exposure is shown at the upper right of each correlation. . . . .	107
5.17	Tangential shear of ACTJ0022. . . . .	112
5.18	Contour map of $\chi^2$ . The contours show 68% and 95% confidence limits (corresponding to $\Delta\chi^2 = 2.3, 6.17$ , respectively). . . . .	113
5.19	Dependency of tangential shear distribution on the number of galaxies used for calculating the tangential shear. We used $10^5$ realizations to calculate the distribution of each case. . . . .	115
5.20	Tangential shear distribution of each bin obtained from $10^5$ realization. Bin ID shown at upper left of each panel increases from the inner bin to outer bin in Fig. 5.17. . . . .	117
5.21	Distribution of cluster mass obtained by propagating the distribution of tangential shear obtained by simulations. . . . .	118
5.22	Bias map of shape measurement. . . . .	122

6.1	Scaling relations between cluster mass and integrated Compton- $y$ parameter. A cyan dashed line is the scaling relation derived by Marrone et al. [53]. Cyan dots show clusters used for deriving the scaling relation. A blue dot is ACTJ0022 whose WL mass is measured by this work and integrated Compton- $y$ parameter is taken from Reese et al. [82]. A green dot is again ACTJ0022 whose integrated Compton- $y$ parameter is same as the blue dot but mass is inferred from integrated Compton- $y$ parameter. A red dot is also ACTJ0022 whose integrated Compton- $y$ parameter is same as the blue dot but mass is inferred from scaling relation between cluster richness and weak lensing mass. The latter two dots are shifted by a factor of 1.04 from the blue dot. A black dashed line is the scaling relation between integrated Compton- $y$ parameter and mass derived from X-ray observables that is derived by using clusters selected by the SPT [6]. A black dotted line is the scaling relation between integrated Compton- $y$ parameter calculated from X-ray observables and mass also derived from X-ray observables [7]. . . . .	130
6.2	$\Lambda$ CDM exclusion curve for joint 95% CL with sky coverage 200 deg <sup>2</sup> and the WL mass of ACTJ0022 which is measured by this work. Circle and diamond points denote the mass without and with the concentration parameter fixed, respectively, and red open and black solid points denote with and without Eddington bias correction. Each point is offset in redshift by 0.01 for clarity. The mass of ACTJ0022 is within the $\Lambda$ CDM paradigm. . . . .	132
A.1	Cross section of the HSC. . . . .	137
A.2	Focal plane of the HSC. . . . .	137
C.1	Schematic of thermal SZ effect. . . . .	148
C.2	CMB spectrum of original (dashed line) and distorted by SZ effect (solid line). This figure is taken from Carlstrom et al. [20]. . . . .	149
C.3	Spectral distortion of CMB radiation due to SZ effect. The left panel shows intensity and the right panel shows temperature. Thick solid line shows thermal SZ effect and dashed line shows kinetic SZ effect. For reference thermal spectrum of CMB scaled by 0.0005 is shown by the dotted line in the left panel. The assumed cluster properties are an electron temperature of 10 keV, a Compton- $y$ parameter of $10^{-4}$ , and a peculiar velocity of 500 km/s. This figure is taken from Carlstrom et al. [20]. . . . .	149
C.4	Picture of ACT. The height of the telescope is 12 m. . . . .	151

C.5 The Compton- $y$  parameter observed by the ACT. This figure is taken from Reese et al. [82]. . . . . 152

# List of Tables

3.1	Specification of CCD employed by Suprime-Cam. . . . .	47
3.2	Specification of Suprime-Cam readout system. . . . .	47
5.1	Summary of exposure time of each band. . . . .	74
5.2	Size and ellipticity before and after PSF is matched. . . . .	88
5.3	Estimated dust extinction around the field of ACTJ0022-0036. . . . .	90
5.4	Photo- $z$ statistics before and after re-calibration of magnitude zero-point. . . . .	91
5.5	Results of NFW profile fitting. . . . .	111
5.6	Estimates of error of tangential shear signals. . . . .	116
5.7	Contamination rates. . . . .	120
5.8	Estimated true mean distance ratio. Values in the parenthesis are the distance ratio calculated by using photo- $z$ . . . . .	120
5.9	Systematic bias. . . . .	122
A.1	Survey layers of HSC. . . . .	137
C.1	Summary of beam parameters of ACT. This table is taken from Swetz et al. [94]. . . . .	152

# Chapter 1

## Introduction

In a past decade, the tremendous progress of observation techniques has helped to enable precision cosmology, establishing the standard paradigm of structure formation, known as the  $\Lambda$ CDM model. Cold dark matter (CDM) plays a central role in structure formation of the universe through gravity. In the CDM model, small objects collapse first and then merge to form more massive objects. The accelerating expansion of the universe was observed. To explain the acceleration, a cosmological constant  $\Lambda$  was introduced into Einstein's equation, which is now generalized as dark energy.

The cosmic acceleration was discovered by a series of supernovae surveys in late 1990s [84, 79], and several ambitious projects were carried out to measure cosmological parameters to establish the  $\Lambda$ CDM model, such as precise measurement of the temperature anisotropies in the cosmic microwave background (CMB) radiation by Wilkinson Microwave Anisotropy Probe (WMAP) [47], and baryon acoustic oscillations (BAO) through the large scale galaxy clustering observed by Sloan Digital Sky Survey (SDSS) [78], and so on. Some optical surveys aiming to put a more stringent constraint on cosmological parameters including the nature of dark energy will be carried out in the coming decade. Hyper Suprime-Cam (HSC)<sup>1</sup> and Dark Energy Survey (DES)<sup>2</sup> plan to start several thousand square-degree survey by ground-based telescope within a few years. The Large Synoptic Survey Telescope (LSST)<sup>3</sup> will carry out even wider ground-based telescope survey covering more than twenty thousand square degrees in the coming decade. These wide, deep optical surveys will make it possible to introduce newer cosmological probes such as cosmic shear, the tiny weak gravitational lensing (WL) effect induced by cosmic structure, and cluster abundance, the number of clusters as a function of mass and redshift.

To improve the cosmological constraints through the cluster abundance, the

---

<sup>1</sup><http://www.naoj.org/Projects/HSC/index.html>

<sup>2</sup><http://www.darkenergysurvey.org/>

<sup>3</sup><http://www.lsst.org/lsst/science/development>

cutting-edge millimeter-wave surveys such as Atacama Cosmology Telescope (ACT[28][94]) and South Pole Telescope (SPT[21]) have already started. Their high angular resolution and temperature sensitivity make it possible to detect clusters by Sunyaev-Zel'dovich (SZ) effect [102][93] (for short summary, see Appendix C) which is caused by inverse Compton scattering between CMB photons and electrons in hot gas of a cluster. The SZ effect is independent of redshift of a cluster, meaning that very distant clusters are as easy to detect as nearby clusters. Thus the SZ effect is the powerful tool to explore early universe ( $z \sim 0.7$ ) when the cosmic acceleration begins.

However, the SZ effect itself does not provide robust mass estimates of clusters since physical assumptions such as dynamical equilibrium and hydrostatic equilibrium are needed. Thus it is necessary to observationally develop the a relationship between the SZ observable and cluster mass, so-called the cluster mass-observable scaling relations. Among several observables used for estimating cluster mass, including X-ray and optical, WL is unique since it does not need any physical assumptions described above and does provide mass estimates including dark matter. WL requires general relativity only. Therefore WL mass estimates will give a robust scaling relation between the SZ effect and cluster mass.

Since the HSC is in collaboration with the ACT, it is possible to study the scaling relation. The HSC is the next-generation prime focus camera of the 8.2-m Subaru Telescope [35] located at the summit of Mauna Kea, which covers 1.5-deg diameter field of view. The unique capabilities of the Subaru Telescope such as photon collecting power and excellent image quality enable us to carry out precise WL measurements. The HSC will start its survey from 2013 to observe 1500 deg<sup>2</sup>, spending five years. The ACT has already observed more than 1500 deg<sup>2</sup>, and its successive survey, ACTPol[69], plans to observe 4000 deg<sup>2</sup> in first three observing seasons which overlaps with the HSC survey region. It is expected to have  $\mathcal{O}(10^2)$  SZ-selected clusters with mass limit  $M > 10^{14}M_{\odot}$  in the HSC survey region. Improvement to the cosmological constraints should be obtained by applying the scaling relation obtained by clusters in the overlapped region to the entire survey area of the ACT/ACTPol. Although the SPT is in collaboration with the DES, they will not be able to probe the early universe since the DES is not as deep as the HSC.

One outstanding concern lies in WL measurements of high-redshift clusters. By using the Suprime-cam[60], the current prime focus camera of the Subaru Telescope whose field of view is about one seventh of that of the HSC, WL mass measurements of nearby clusters ( $z \sim 0.2$ ) and intermediate redshift ( $z \sim 0.5$ ) have been established[76][75]. However, the feasibility of WL measurements on high-redshift clusters ( $z \sim 0.8$ ) is not clear yet.

We test the feasibility of the high-redshift WL mass measurement by carrying out follow-up observations of a cluster, ACT-CL J0022–0036 (hereafter ACTJ0022), by the Suprime-Cam. ACTJ0022 was discovered by the ACT through the SZ effect.

This cluster has the highest signal-to-noise ratio in 200-deg<sup>2</sup> of equatorial region that was observed by the ACT in 2009. In addition the cluster has one of the brightest SZ signals. These facts imply the cluster is extremely massive,  $\sim 10^{15}h^{-1}M_{\odot}$ , and at high redshift. In fact, long slit spectroscopy of the brightest cluster galaxy (BCG) using the Apache Point and Gemini South Observatories gave a cluster redshift of  $z = 0.81$ . Therefore ACTJ0022 is an appropriate sample to test the feasibility of the WL mass measurement on high-redshift clusters.

In addition to the feasibility test, the cluster will provide cosmological implications. Based on the cluster abundance, Mortonson et al. [62] developed a framework which enables us to test the  $\Lambda$ CDM model before the surveys produce their large amount of data. In this framework, even a single massive cluster can rule out the  $\Lambda$ CDM model at a certain confidence level (CL). Since a cluster at high redshift provides a high level of exclusion, the ACTJ0022 is an appropriate sample to test the  $\Lambda$ CDM model through the framework.

To give a robust estimate of cluster mass through WL, it is important to select background galaxies carefully. One or two colors (difference of magnitudes between two bands) have been often used for low- and mid- redshift clusters [76][75]. However, since our cluster is at high redshift, we must define a reliable catalog of background galaxies using photometric redshifts. For this purpose we took data in  $Br'i'z'Y$ .

We applied the WL measurement algorithm, which we are developing for future wide field surveys such as the HSC, to the cluster image data. The shearing effect caused by WL is too small to measure from a single galaxy, but it can be extracted by summing up an adequate number of observed galaxy shapes to cancel out their intrinsic shapes. Currently measurement of WL signal is limited by statistics. However, a large amount of data become available after the wide-field surveys are carried out in the coming decade. At this stage, it is important to suppress systematics of WL measurement. It is pointed out the WL measurement method which has been widely used, such as KSB [40], has 10 – 20% systematic errors. We implemented another method proposed by Bernstein and Jarvis [10] and later improved by Nakajima and Bernstein [64], so-called EGL method.

In addition, we extended the EGL method for the multiple-exposure analysis in a straightforward way. Traditionally, a stacked image is used for WL analysis. However, image stacking mixes different signatures of each exposure, which is embedded in point spread function (PSF), and lose the original information. The EGL method can perform simultaneous multiple-exposure fitting, combining the likelihoods constructed by using a PSF model of each exposure. In this thesis, we provide a new prescription to remove exposures which do not have enough quality for WL measurements.

We made use of the HSC pipeline, the software suite being developed for the data reduction of HSC survey data. Since the Suprime-Cam uses same CCDs as the HSC, it is valuable to test and improve the pipeline with the cluster data.

The outline of this thesis is as follows. First, we will give an overview of the  $\Lambda$ CDM model, and describe details of the framework to test the  $\Lambda$ CDM model and basics of WL in Chapter 2. In Chapter 3, an overview of observational apparatus will be presented. The EGL method and its test will be described in Chapter 4. The analysis of ACTJ0022 and discussions of the result will be presented in Chapter 5 and Chapter 6, respectively. Finally we will conclude our study in Chapter 7.

# Chapter 2

## Cluster Cosmology and Weak Lensing Mass Measurement

### 2.1 $\Lambda$ CDM Model

In this section, we briefly review the  $\Lambda$ CDM model, the standard model of the universe that has been in good agreement with a series of observations.  $\Lambda$  stands for the cosmological constant that explains the current accelerating universe. CDM is in abbreviation for cold dark matter that plays an important role in structure formation. In section 2.1.1, we describe smooth, expanding universe including fundamental equations, dynamics of the universe, and the cosmological constant. Then in Section 2.1.2, we explain the structure formation including cold dark matter and formation of astronomical objects such as galaxies and clusters.

#### 2.1.1 Smooth, Expanding Universe

##### Fundamental Equations of Expanding Universe

We assume a homogeneous and isotropic universe. “Homogeneous” means that there are no special places in the universe, and “isotropic” means that there are no special directions in the universe. This assumption is based on the fact that there are no special observers; human beings are not special at all. This is called the cosmological principle. The assumption is the case for very large scale of the universe ( $\gtrsim 1\text{Gpc}$ ), and has been supported by many observational facts such as Cosmic Background Explorer (COBE) [90]. Under this assumption, the metric of the universe is written as

$$ds^2 = -c^2 dt^2 + a^2(t) \left[ \frac{dr^2}{1 - Kr^2} + r^2 (d\theta^2 + \sin^2 \theta d\phi^2) \right], \quad (2.1)$$

which is called Robertson-Walker metric. Here  $c$  is the speed of light,  $a(t)$  is the scale factor, and  $K$  is the spatial curvature.  $x^i = (r, \theta, \phi)$  is called comoving coordinates, which is invariant with the expansion of the universe. For instance, a galaxy moving with the expansion of the universe is fixed on the comoving coordinates. The scale factor  $a(t)$  is normalized to unity at present  $t_0$  (hereafter we use subscription “0” for denoting a quantity at present):

$$a_0 \equiv a(t_0) = 1, \quad (2.2)$$

and related with the redshift

$$z \equiv \frac{\lambda_0 - \lambda_e}{\lambda_e}, \quad (2.3)$$

where  $\lambda_e$  is the wavelength of an emission line at source and  $\lambda_0$  is that at an observer, as follows:

$$1 + z = \frac{1}{a}. \quad (2.4)$$

In addition, the scale factor is related to Hubble parameter as

$$H = \frac{\dot{a}}{a}. \quad (2.5)$$

For energy-momentum tensor, the following form of perfect fluid is used

$$T_{\mu\nu} = (\rho c^2 + P)u_\mu u_\nu + P g_{\mu\nu}, \quad (2.6)$$

where  $u_\mu$  denotes 4-velocity, and  $\rho$  and  $P$  denotes energy density and pressure of the fluid, respectively. Substituting Eq. (2.1) and (2.6) into the Einstein equation

$$R_{\mu\nu} - \frac{1}{2}Rg_{\mu\nu} + \Lambda g_{\mu\nu} = \frac{8\pi G}{c^4}T_{\mu\nu}, \quad (2.7)$$

where  $R_{\mu\nu}$  is Ricci tensor,  $R$  is Ricci scalar,  $\Lambda$  is cosmological constant, and  $G$  is gravitational constant, the following equations are obtained:

$$\left(\frac{\dot{a}}{a}\right)^2 = \frac{8\pi G}{3}\rho - \frac{Kc^2}{a^2} + \frac{\Lambda c^2}{3}, \quad (2.8)$$

$$\frac{\ddot{a}}{a} = -\frac{4\pi G}{3c^2}(\rho c^2 + 3P) + \frac{\Lambda c^2}{3}. \quad (2.9)$$

The former equation is often called the Friedmann equation. To characterize the perfect fluids, the following form of the equation of state is often assumed:

$$P = w\rho c^2. \quad (2.10)$$

Relativistic particles, or radiation, have  $w = 1/3$ , while non-relativistic particles, or matter, have  $w = 0$ . With Eq. (2.8) and (2.9), the energy density depends on the evolution of the universe as

$$\rho = \rho_0 a^{-3(1+w)} = \rho_0 (1+z)^{3(1+w)}. \quad (2.11)$$

Thus matter density and radiation density depends on the scale factor as  $\rho_m = \rho_{m,0} a^{-3}$  and  $\rho_r = \rho_{r,0} a^{-4}$ , respectively. The matter density depends on the physical volume of the universe, while the radiation distance has an additional factor of  $a$  since its wavelength becomes longer as the universe expands. If the cosmological constant is regarded as energy-moment tensor, its energy density and pressure is written as

$$\rho_\Lambda = \frac{\Lambda c^2}{8\pi G}, \quad (2.12)$$

$$P_\Lambda = -\frac{\Lambda c^4}{8\pi G}. \quad (2.13)$$

Thus the cosmological constant can be regarded as the perfect fluid having equation of state  $P_\Lambda = -\rho_\Lambda c^2$ , and its energy density no longer depends on the scale factor. In general, the perfect fluid having the equation state

$$P_{\text{DE}} = w \rho_{\text{DE}} c^2 \quad (w < -\frac{1}{3}) \quad (2.14)$$

is called dark energy. From (2.9), dark energy accelerates expansion of the universe. Next, we derive the evolution of Hubble parameter. Hereafter we ignore radiations since their energy fraction is sufficiently small at present. We introduce the critical density

$$\rho_c = \frac{3H^2}{8\pi G}, \quad (2.15)$$

and density parameters are defined as

$$\Omega_m = \frac{\rho_m}{\rho_c}, \quad (2.16)$$

$$\Omega_\Lambda = \frac{\rho_\Lambda}{\rho_c}. \quad (2.17)$$

Then Eq. (2.8) is written as

$$H^2(z) = H_0^2 \left[ \Omega_{m,0} (1+z)^3 - \frac{Kc^2}{H_0^2} (1+z)^2 + \Omega_{\Lambda,0} \right] \equiv H_0^2 E(z)^2. \quad (2.18)$$

From observational results, the universe is almost flat, i.e,  $K \sim 0$ . Combined with Baryon acoustic oscillation and Hubble constant measurement, WMAP[47] yielded

$H_0 = 70.2 \pm 1.4$  km/s/Mpc,  $\Omega_{m,0} = 0.275 \pm 0.015^1$ ,  $\Omega_{\Lambda,0} = 0.725 \pm 0.016$ . The dark energy equation of state parameter,  $w$ , is  $-1.10 \pm 0.14$ . A time-dependent equation of state in the form of  $w = w_0 + w(1 - a)$ , with Type Ia supernovae data,  $w_0 = -0.93 \pm 0.13$  and  $w_a = -0.41_{-0.71}^{+0.72}$ . The present value of Hubble parameter is often written as

$$h \equiv \frac{H_0}{100 \text{kms}^{-1} \text{Mpc}^{-1}}. \quad (2.19)$$

### Cosmological Distances

In the universe, definition of distance is no longer unique. Therefore it is necessary to define cosmological distance. Here we introduce two definitions, comoving distance and angular diameter distance.

**Comoving Distance** Comoving distance is defined as the distance between observer to source measured in present cosmological time:

$$\chi(z) \equiv \int_0^r \frac{dr}{\sqrt{1 - Kr^2}} = \int_t^{t_0} \frac{cdt}{a(t)} = \int_0^z \frac{cdz}{H(z)}. \quad (2.20)$$

Using comoving distance, Eq. (2.1) can be rewritten as

$$ds^2 = -c^2 dt^2 + a^2(t) [d\chi^2 + r^2(\chi)(d\theta^2 + \sin^2 \phi)], \quad (2.21)$$

where

$$r(\chi) = \begin{cases} \frac{1}{\sqrt{-K}} \sinh [\sqrt{-K}\chi] & (K < 0) \\ \chi & (K = 0) \\ \frac{1}{\sqrt{K}} \sin [\sqrt{K}\chi] & (K > 0). \end{cases} \quad (2.22)$$

**Angular Diameter Distance** Suppose we measure the distance  $ds$  between  $(r, \theta, \phi)$  and  $(r, \theta + d\theta, \phi)$ . From Eq. (2.1),

$$ds^2 = a^2(t)r^2 d\theta^2. \quad (2.23)$$

Angular diameter distance is defined as

$$D_A(z) = \frac{ds}{d\theta} = a(t)r = \frac{r[\chi(z)]}{1+z}. \quad (2.24)$$

---

<sup>1</sup>This value is calculated by combining baryon density and dark matter density.

## 2.1.2 Structure Formation

So far we have considered the homogeneous, isotropic universe. However, at small scales, there exist highly concentrated structures such as galaxies and clusters of galaxies. If the universe were perfectly homogeneous at early times, these structures would not exist. In fact, primordial small fluctuations exist in the early universe. Then gravitational instability amplifies the fluctuations, and structures begin to form. In the process of structure formation, it is known that dark matter plays an important role. Dark matter occupies about 80% of matter in the universe, and helps to form highly concentrated objects, galaxies and clusters. Dark matter can be classified into some categories. Among them, we will explain hot dark matter and cold dark matter. Then we will describe how the highly concentrated objects are formed.

### Hot Dark Matter and Cold Dark Matter

At early times the universe is dominated by radiation. As described in Section 2.1.1, the energy density of radiation falls down earlier than that of matter. Thus after the epoch when these densities are equal  $a_{\text{eq}}$ , matter dominates the universe, and then structure formation begins. Since dark matter does interact only through gravity or weak force, in relativistic epoch relativistic dark matter particles have relativistic velocity. As a result smaller fluctuations than horizon at  $a_{\text{eq}}$ ,  $\sim 30$  Mpc, are disappeared. This effect is known as free streaming, and such a dark matter is called hot dark matter. This model predicts super-cluster size structures are formed first, which is called the “top-down” scenario. On the other hand, cold dark matter becomes non-relativistic at early stage, and does not cause free streaming. As a result, small scale structures are formed first, and then they grow towards large scale. This is called the “bottom-up” scenario, and is strongly supported by current observational results.

### Formation of Astronomical Objects and Prediction of its Abundance

The mass density fluctuation is defined as

$$\delta(\mathbf{x}, t) \equiv \frac{\rho_m(\mathbf{x}, t) - \bar{\rho}_m(t)}{\bar{\rho}_m(t)}, \quad (2.25)$$

which defined in comoving coordinates. Here  $\rho_m(\mathbf{x}, t)$  denotes matter density at position  $\mathbf{x}$  and time  $t$  and  $\bar{\rho}_m(t)$  denotes mean matter density at time  $t$ . It is known that a probability distribution function of the density fluctuation follow Gaussian in high precision. Following fluid dynamics, within the regime of “linear” fluctuation,

$\delta \ll 1$ , the time evolution of density fluctuation is written as<sup>2</sup>

$$\ddot{\delta}_{\mathbf{k}} + 2\frac{\dot{a}}{a}\dot{\delta}_{\mathbf{k}} - 4\pi G\bar{\rho}_m\delta_{\mathbf{k}} = 0, \quad (2.26)$$

where  $\delta_{\mathbf{k}}(t)$  is the Fourier transformation of  $\delta(\mathbf{x}, t)$ :

$$\delta_{\mathbf{k}}(t) = \int \delta(\mathbf{x}, t)e^{-i\mathbf{k}\cdot\mathbf{x}}d^3x. \quad (2.27)$$

Note that Eq. (2.26) does not depend on  $\mathbf{k}$ . Thus fluctuation of different  $\mathbf{k}$  evolves independently, which is the advantage of linear theory. The solution of Eq. (2.26) is written as

$$\delta_{\mathbf{k}}(t) = C_1(\mathbf{k})D_1(t) + C_2(\mathbf{k})D_2(t), \quad (2.28)$$

where  $C_1(\mathbf{k})$  and  $C_2(\mathbf{k})$  is arbitrary time-independent function,  $D_1(t)$  is a growing solution, and  $D_2(t)$  is a decaying solution. As the universe evolves, the  $D_2$  decays. Thus the time evolution of matter fluctuation is described by  $D_1(t)$ , which is called linear growth factor. The Fourier counterpart of correlation function  $\langle\delta(\mathbf{x})\delta(\mathbf{x}')\rangle$  becomes

$$\langle\delta_{\mathbf{k}}\delta_{\mathbf{k}'}\rangle = (2\pi)^3P(k)\delta(\mathbf{k} + \mathbf{k}'), \quad (2.29)$$

where  $P(k)$  is called power spectrum. Note that the power spectrum does not depend on the direction of  $\mathbf{k}$ , because the universe is isotropic. The power spectrum reflects statistical nature of matter fluctuation, and is extremely sensitive to cosmological parameters, which has been used by various observations.

At scale smaller than  $\lesssim 10$  Mpc, the linear perturbation theory is no longer applicable. Thus the formation of astronomical objects such as clusters and galaxies should be described by “non-linear” fluctuation, where analytical approach is difficult. Press and Schechter [80] predicted how many galaxies and clusters are formed, combining the linear perturbation theory and spherical collapse model, a simple model to investigate the non-linear theory. This prediction indicates that the number of astronomical objects exponentially decreases at high mass end and thus the number of massive clusters is sensitive to a cosmological model. Based on this theory, a lot of works have been done to find a fitting function to describe result of N-body simulations. Here we show one example by Tinker et al. [95]. In general, the mass function is often written as

$$\frac{dn}{d\ln M} = \frac{\bar{\rho}_{m,0}}{M} \left| \frac{d\ln \sigma}{d\ln M} \right| f(\sigma, z), \quad (2.30)$$

where  $\sigma(M, z)$  is the rms of linear density fluctuation smoothed over spheres of comoving radius  $R = (3M/4\pi\rho_{m,0})^{1/3}$ , i.e., for the smoothed fluctuation

$$\delta_R(\mathbf{x}, z) = \int \delta(\mathbf{x}')W(\mathbf{x} - \mathbf{x}'; R)d^3x', \quad (2.31)$$

---

<sup>2</sup>We assumed pressure is negligible since we are interested in the matter dominated universe.

where  $W(\mathbf{x}; R)$  is a smoothing function,

$$\sigma^2(M, z) = \langle |\delta_R(\mathbf{x}, z)|^2 \rangle \quad (2.32)$$

$$= \frac{1}{(2\pi)^3} \int P(k, z) \tilde{W}^2(kR) d^3k \quad (2.33)$$

$$= \left[ \frac{D(z)}{D(0)} \right]^2 \frac{1}{(2\pi)^3} \int P(k, 0) \tilde{W}^2(kR) d^3k \quad (2.34)$$

$$= \left[ \frac{D(z)}{D(0)} \right]^2 \sigma^2(M, 0), \quad (2.35)$$

where  $\tilde{W}$  is the smoothing function in Fourier space, for which Tinker et al. [95] used a top-hat function. Practically  $\sigma^2(M, 0)$  is often calculated through  $P(k, 0)$  which is given by a software called CAMB<sup>3</sup>. Tinker et al. [95] found the following fitting function for simulations based on WMAP first year results [91]

$$f(\sigma, z) = A \left[ \left( \frac{\sigma}{b} \right)^{-a} + 1 \right] e^{-c/\sigma^2}, \quad (2.36)$$

where  $A = 0.186(1+z)^{-0.14}$ ,  $a = 1.47(1+z)^{-0.06}$ ,  $b = 2.57(1+z)^{-0.011}$ , and  $c = 1.19$ . The cluster mass is defined as

$$M_\Delta = \Delta \frac{4\pi r_\Delta^3}{3} \bar{\rho}_{m,0}, \quad (2.37)$$

which means halo mass within a spherical region with comoving radius  $r_\Delta$  that is defined as the average density of the enclosure is equal to  $\Delta$  times the mean matter density at present,  $\bar{\rho}_{m,0}$ . The fitting function is shown in Fig. 2.1.

## 2.2 Testing $\Lambda$ CDM Model with a Massive, High-redshift Cluster

### 2.2.1 Theory

Clusters of galaxies are the most massive structures in the universe, and they reflect the growth of structure in the universe. For example, cluster abundance, which describes how many clusters exist at a given mass and redshift, can be predicted by a cosmological model, as described in Section 2.1.2. Comparing the prediction with observed cluster abundance, one can constrain the cosmological model. For example, one of the pioneering works to constraint cosmological parameters by cluster abundance was done by Kitayama and Suto [45], and the recent constraint was provided

---

<sup>3</sup><http://camb.info/>

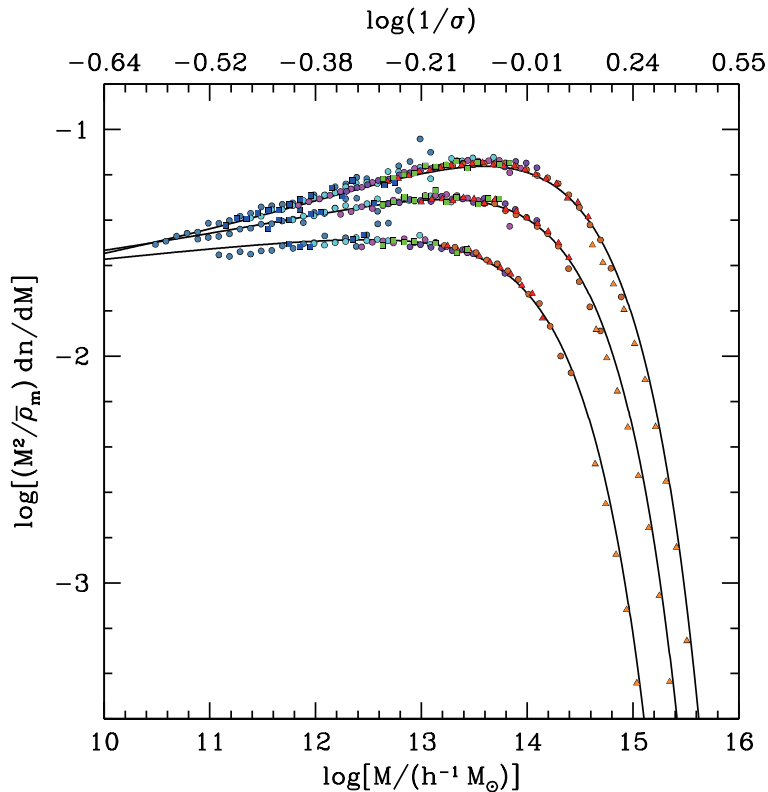


Figure 2.1: The three sets of points denote measured mass function with  $\Delta = 200$ , 800, and 3200 (from top to bottom) for simulations based on WMAP first year results. Solid curves denote mass function Tinker et al. [95] derived. This figure is taken from Tinker et al. [95].

by Vikhlinin et al. [99], both of which were based on X-ray observables. Sehgal et al. [88] presented constraints on cosmological parameters based on SZ-selected galaxy clusters detected by millimeter-wave survey conducted out by ACT, using scaling relation between SZ signal and cluster mass. They used 9 optically confirmed high-mass clusters in 455 square degrees of sky. A lot of surveys including optical, X-ray, and millimeter aim to constrain cosmological parameters by observing more clusters.

On the other hand, it is possible to test the  $\Lambda$ CDM paradigm by using a single extreme massive cluster. This test is based on the fact that exponential suppression of the cluster abundance at high mass gives robust upper bounds on the number of high mass clusters. Mortonson et al. [62] provides the framework to give the confidence level (CL) at which the observation of a cluster of mass  $M$  and redshift

$z$  can falsify the  $\Lambda$ CDM model<sup>4</sup>. The framework tells a tension the newly observed cluster mass has against the probability of the number of the cluster derived from a known data set, such as CMB, SNe, BAO and so on. In this section, we summarize their framework.

They quantified two types of CL for statistical uncertainties. The first is called *parameter variance*, which is associated with the uncertainties on the mean cluster number  $> M$  and  $> z$ ,  $\bar{N}(M, z)$ . The uncertainty is represented by probability distribution function which is derived by propagating the uncertainty of a given data set through the  $\Lambda$ CDM model. They take the one-tailed  $100p\%$  CL upper limits on the mean number  $\bar{N}_{Pp}(M, z)$ . For example, the mean number of clusters  $\bar{N}(M, z)$  is less than  $\bar{N}_{P,95}(M, z)$  with 95% probability.

The second CL is called *sample variance*. They assumed the distribution of the cluster number in a sample follows Poisson statistics. For a mean cluster number  $\bar{N}$ , the probability that no cluster is observed in a random sample of sky  $f_{\text{sky}}$  is  $s \equiv e^{-\bar{N}f_{\text{sky}}}$ . They defined the sample variance  $100s\%$  CL and the corresponding mean cluster number in full sky as

$$\bar{N}_{Ss}(f_{\text{sky}}) \equiv -f_{\text{sky}}^{-1} \ln s. \quad (2.38)$$

If the  $\Lambda$ CDM model predicts the mean number of cluster above  $M$  and  $z$  is  $\bar{N}_{Ss}$  in the full sky, and if one or more such clusters are observed in a survey covering  $f_{\text{sky}}$  of full sky, the  $\Lambda$ CDM model is excluded at  $100s\%$  CL.

Next, they combined these two types of uncertainties. The mass and redshift limit within a certain area of sky which corresponds to  $100s\%$  sample CL and  $100p\%$  parameter CL can be found by solving

$$\int_{-\infty}^{\log(-f_{\text{sky}}^{-1} \ln s)} d \log \bar{N} P(\log \bar{N} | M, z) = p, \quad (2.39)$$

where  $P(\log \bar{N} | M, z)$  is the probability distribution of the cluster number density above  $M$  and  $z$  for the  $\Lambda$ CDM model. They defined *joint* CL where  $s = p$ , and hereafter when we write CL, it means the joint CL. Plotting  $M$  and  $z$  satisfying this equation with  $s = p = 0.95$  gives an exclusion curve of the  $\Lambda$ CDM model at 95% CL on  $M$ - $z$  plane.

For computing the expected mean number of clusters with  $> M$  and  $> z$  for a full sky,  $\bar{N}(M, z)$ , they integrated the product of mass function  $dn/d \ln M$  and comoving volume element  $dV(z) = r^2 dr d\Omega / \sqrt{1 - Kr^2} = cr^2(\chi(z)) dz d\Omega / H(z)$ :

$$\bar{N}(M, z) = \int_z^\infty dz' \frac{4\pi cr^2(\chi(z'))}{H(z')} \int_M^\infty \frac{dM'}{M'} \frac{dn}{d \ln M}(M', z'). \quad (2.40)$$

For the mass function, they adopted the fitting function provided by Tinker et al. [95] that is written in Section 2.1.2. They used  $M_{200}$  for cluster mass.

<sup>4</sup>Actually their framework can be extended to test quintessence.

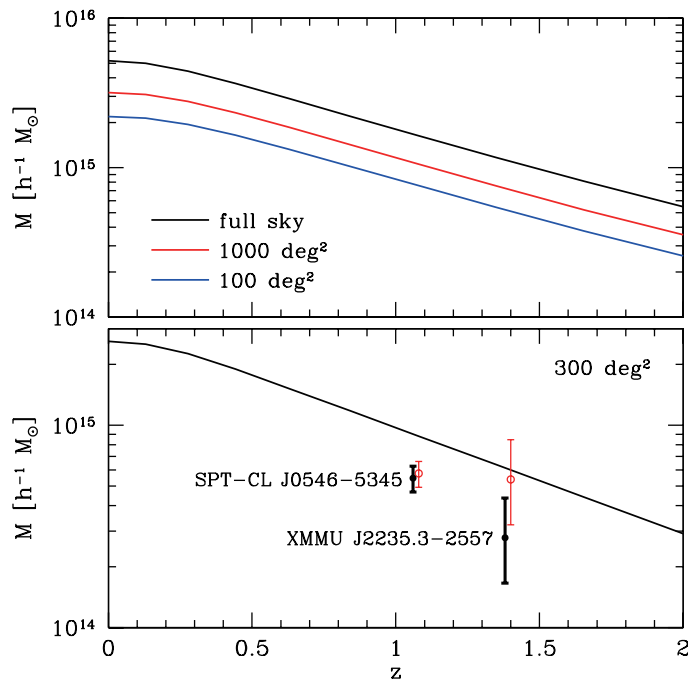


Figure 2.2:  $M$ - $z$  exclusion curves taken from Mortonson et al. [62] and slightly modified. Even a single massive cluster above the curve falsifies the  $\Lambda$ CDM model at 95% CL. *upper panel*: The exclusion curve in three cases of sky coverage. *lower panel*: Observed cluster mass with the exclusion curve of 300-deg<sup>2</sup>; SPT-CL J0546-5345 ( $M_{200} = (8.23 \pm 1.21) \times 10^{14} M_{\odot}$ ) and XMMU J2235.3-2557 ( $M_{200} = 7.7^{+4.4}_{-3.1} \times 10^{14} M_{\odot}$ ). Red open points are without Eddington bias correction, and black solid points are with Eddington bias correction.

Using the constraints from Type Ia SN [44], CMB [49], BAO [77], and Hubble constant measurement [85], they drew the  $M$ - $z$  exclusion curves of 95% CL for the  $\Lambda$ CDM model as shown in Fig. 2.2. The upper panel shows the exclusion curves for three cases of sky coverage. As the sky coverage becomes larger, the probability to find massive clusters becomes higher. Thus a more massive cluster is needed to rule out the  $\Lambda$ CDM model. As the redshift goes higher, the exclusion curve goes down. This is because in early universe the structure does not grow enough to form a lot of massive clusters. In the lower panel, they plotted mass estimation of two massive clusters with the exclusion curve of 300-deg<sup>2</sup> sky coverage. The one is SPT-CL J0546-5345 [18] at  $z = 1.07$  whose mass is determined by  $Y_X$  (the product of gas mass and temperature), the estimator from X-ray observation. The cluster is

the first  $z > 1$  cluster discovered through SZ survey by the SPT in 2008 covering 175 deg<sup>2</sup>. The other is XMMU J2235.3-2557 [92] observed by XMM-Newton whose mass is estimated from  $T_x$  (temperature). The survey covered 283 deg<sup>2</sup>.

When plotting an observed mass, we should correct Eddington bias which is the combined effect of a steep mass function and measurement uncertainty. Since the mass function is steep at high mass end, scattering from low masses to high observables is more likely than scattering from high masses to low observables. Therefore, Eddington bias correction always reduces the observed mass. In the lower panel of Fig. 2.2, the cluster masses with and without Eddington bias correction are shown in black solid points and red open points, respectively. Both of the cluster mass of SPT-CL J0546-5345 and XMMU J2235.3-2557 do not exclude  $\Lambda$ CDM model.

Their framework is being currently widely used. Williamson et al. [101] tested  $\Lambda$ CDM by using their cluster samples found in 2500-deg<sup>2</sup> survey conducted by the SPT. Jee et al. [36] applied the framework to high-redshift clusters at  $z \gtrsim 1$ .

## 2.2.2 Sample Selection

To test the  $\Lambda$ CDM model with the framework provided by Mortonson et al. [62], it is important to select a massive, high-redshift cluster of galaxies in a survey region. For example, collecting follow-up observations of such clusters is not appropriate to use the framework, since it is impossible to reasonably define the survey area.

We selected a cluster of galaxies, ACTJ0022<sup>5</sup>, discovered by a survey conducted by the ACT<sup>6</sup>. Since the SZ effect is independent of redshift, the ACT is able to efficiently find high-redshift clusters. ACTJ0022 has the highest signal-to-noise ratio (SN) of all clusters found in the 200-deg<sup>2</sup> survey around equatorial region<sup>7</sup> that overlaps with SDSS Stripe-82 [2]. It is among the largest of the SZ signals, but there are others with comparable amplitudes. The high SN suggests a compact SZ profile. If a cluster is large, the SZ profile is contaminated by the CMB and thus SN is decreased. The size of the SZ signal suggests the cluster is massive. The combination of compact and massive means high redshift. Note that a low-redshift cluster can be compact if it is not massive. Long slit spectroscopy of the BCG using the Apache Point and Gemini South Observatories are carried out to give a cluster redshift. It is revealed that the cluster is in fact at high redshift,  $z = 0.81$ .

Surveys conducted by the ACT are reasonably uniform. Sensitivity maps of the surveys are shown in Fig. 2.3 for the illustrative purpose, which is taken from Hand et al. [31]. Note that this map does not completely coincide with the 200-deg<sup>2</sup>

<sup>5</sup>Information of ACTJ0022 is provided by Tobias Marriage in private communication.

<sup>6</sup>Summary for the instrumental aspect of the ACT can be found in Appendix C.2.

<sup>7</sup>The details of the survey are not able to be presented in this thesis, since they are not published yet.

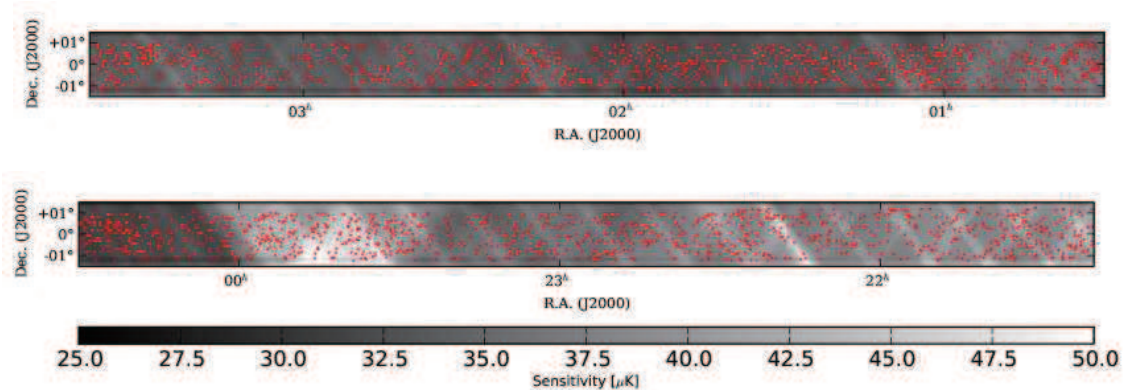


Figure 2.3: Sensitivity maps around an equatorial region surveyed by the ACT. This figure is taken from Hand et al. [31]. The gray-scale encodes the noise rms in  $\mu\text{K}$  of a map match-filtered for cluster detection. Red point shows a position of luminous red galaxy that is irrelevant to our study.

equatorial region where ACTJ0022 has the highest SN. The mean sensitivity of this 200-deg<sup>2</sup> is  $\sim 40 \mu\text{K}$  and the sensitivity is within only a few factors.

When the cluster is used for the test of the  $\Lambda\text{CDM}$  model in the framework, the most conservative limits are obtained by assuming full sky survey. In this case, the cluster is considered to be the one that is most likely above the exclusion curve, although there is high possibility that more massive or distant clusters exist in regions other than the 200-deg<sup>2</sup> equatorial region. We can obtain the second most conservative limits by assuming that the 200-deg<sup>2</sup> is observed, considering that the completeness at mass and redshift level of ACTJ0022 is essentially unity since the cluster has the highest SN and the high SZ signal, and the noise level is rather uniform in the survey<sup>8</sup>. In this study, we considered the cluster to be most likely above the exclusion curve in the 200-deg<sup>2</sup> region, although there is possibility that more massive or distant clusters may exist in region where noise level is higher than that of the position of ACTJ0022. In fact, we could shrink the survey area and draw the exclusion curve by removing the regions with high noise level. However, we take 200-deg<sup>2</sup> since this is reasonably conservative and the removal of higher noise regions would not drastically change the exclusion curve.

<sup>8</sup>Completeness is defined as the ratio between the number of clusters that intrinsically exist in the sky and the number of clusters that are actually observed. In general, clusters with high SN has high completeness. In SZ surveys, massive and high-redshift clusters have high SN. Note that high-redshift clusters are compact, less contaminated by the CMB as described in text, and thus have high SN.

### 2.2.3 Cluster Mass Indicators

There are several mass indicators of a cluster of galaxies (for a detailed review, see Voit [100]). For example, SZ signals itself can be used for estimating mass, since it represents gas pressure. Similarly X-ray observables (luminosity and temperature) and velocity dispersions of member galaxies can be used as a mass estimator. However, from these observables, cluster mass can be estimated under an assumption of dynamical equilibrium or hydrostatic equilibrium.

Another mass indicator is optical richness, the number of member galaxies that are above some luminosity threshold. However, since most of the cluster mass is from dark matter, it is not straightforward to convert this observable to cluster mass.

WL is a unique indicator since it directly gives mass estimate including dark matter. Both dark matter and baryons contribute to WL, and we do not need any physical assumptions except for general relativity. We used WL for estimating mass of the cluster to test the  $\Lambda$ CDM model with the framework.

## 2.3 Estimation of Cluster Mass through Weak Lensing

### 2.3.1 Basics of Weak Lensing

Figure 2.4 shows a typical lensing system of thin lens approximation, where the distances between source galaxies, a lens, and an observer are much larger than the size of lens. Although in general there are a lot of gravitational lenses between the observer and the source galaxies, thin lens approximation works well in the WL caused by a cluster, so-called cluster-galaxy lensing. Assuming that angles appearing in Fig. 2.4 are small,  $D_s\theta = D_s\beta + D_{ls}\hat{\alpha}$ , where  $D_s$  and  $D_{ls}$  is the angular diameter distance between the observer and source, the lens and source, respectively. Thus light from a source is distorted as

$$\boldsymbol{\beta} = \boldsymbol{\theta} - \boldsymbol{\alpha}(\boldsymbol{\theta}), \quad (2.41)$$

where  $\boldsymbol{\beta}$  is the position of the source in absence of the lens,  $\boldsymbol{\theta}$  is the position of the lensed, (or observed) source, and  $\boldsymbol{\alpha}$  is scaled deflection angle  $\boldsymbol{\alpha} \equiv D_{ls}/D_s\hat{\boldsymbol{\alpha}}$ . Equation (2.41) is called lens equation. The deflection angle is written as

$$\boldsymbol{\alpha}(\boldsymbol{\theta}) = \frac{D_{ls}}{D_s}\hat{\boldsymbol{\alpha}}(\boldsymbol{\theta}) = \frac{2}{c^2} \frac{D_{ls}}{D_s} \int dz \nabla_L \Phi, \quad (2.42)$$

where  $\Phi$  is Newton potential,  $z$  is a physical coordinate along the line of sight, and  $\nabla_L$  is derivative along the direction perpendicular to the line of sight, i.e.,

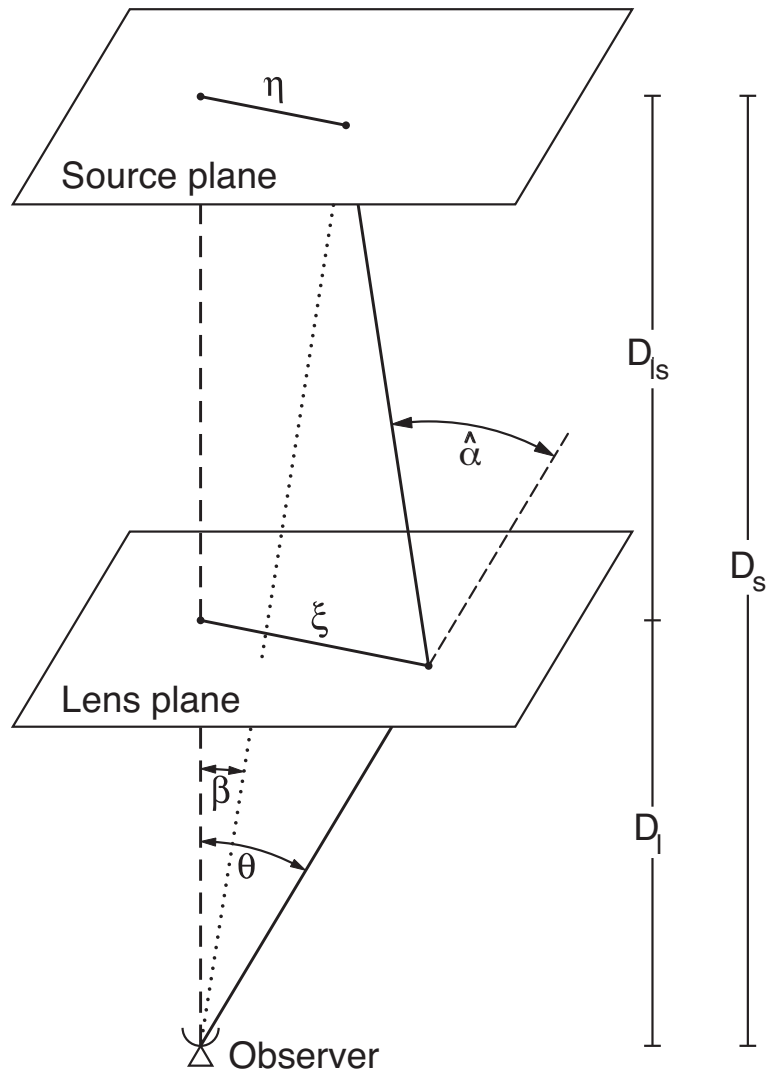


Figure 2.4: Typical weak lensing system in the limit of thin lens approximation. This figure is taken from Bartelmann and Schneider [9] and slightly modified.

$\nabla_L = D_l^{-1} \nabla_\theta$ , where  $D_l$  is angular diameter distance between the observer and lens. The lens potential  $\psi$  is defined as

$$\boldsymbol{\alpha}(\boldsymbol{\theta}) = \nabla_\theta \psi. \quad (2.43)$$

Next, let us consider how a source having finite size is mapped by the gravitational lensing. The center of source is mapped as

$$\boldsymbol{\beta}_0 = \boldsymbol{\theta}_0 - \boldsymbol{\alpha}(\boldsymbol{\theta}_0). \quad (2.44)$$

The small deviation from this center in the source plane,  $\delta\boldsymbol{\beta}$ , is mapped to the lens plane as

$$\delta\boldsymbol{\beta} = A_{ij}(\boldsymbol{\theta}_0) \delta\boldsymbol{\theta}, \quad (2.45)$$

where  $A_{ij}(\boldsymbol{\theta}_0)$  is called Jacobian matrix;

$$A_{ij}(\boldsymbol{\theta}) = \delta_{ij} - \psi_{,ij}(\boldsymbol{\theta}). \quad (2.46)$$

We define convergence  $\kappa \equiv \frac{1}{2}(\psi_{,11} + \psi_{,22})$  and shear  $\boldsymbol{\gamma} \equiv (\frac{1}{2}(\psi_{,11} - \psi_{,22}), \psi_{,12})$ . Using these parameters,

$$A = \begin{pmatrix} 1 - \kappa - \gamma_1 & -\gamma_2 \\ -\gamma_2 & 1 - \kappa + \gamma_1 \end{pmatrix}. \quad (2.47)$$

The WL regime is defined as the limit of  $\kappa \ll 1$  and  $\boldsymbol{\gamma} \ll 1$ . WL maps a source as shown in Fig. 2.5. Convergence  $\kappa$  just changes the size of the source, and shear  $\boldsymbol{\gamma}$  distorts the source. The first component of shear elongates the source along x-axis and the second component elongates it along the axis rotated by 45 degrees from x-axis. Shear is spin-2 quantity, i.e.,  $\boldsymbol{\gamma} = \gamma \exp(2\phi i)$ , where  $\phi$  is position angle of the ellipse.

WL magnifies the flux of source. Since WL does not generate any photons, surface brightness of the source  $b(\boldsymbol{\beta})$  is conserved. Thus the magnification effect  $\mu(\boldsymbol{\theta})$  is represented as

$$\mu(\boldsymbol{\theta}) \equiv \frac{\int d^2\boldsymbol{\theta} b(\boldsymbol{\theta})}{\int d^2\boldsymbol{\beta} b(\boldsymbol{\beta})} = \frac{1}{|\det(A)|} \frac{\int d^2\boldsymbol{\theta} b(\boldsymbol{\theta})}{\int d^2\boldsymbol{\theta} b(\boldsymbol{\theta})} \quad (2.48)$$

$$= \frac{1}{(1 - \kappa)^2 - \gamma^2}. \quad (2.49)$$

Note that the direct observable from galaxy shape measurement is so-called reduced shear  $\boldsymbol{g} = \boldsymbol{\gamma}/(1 - \kappa)$ , and Eq. (2.47) is written as

$$A = (1 - \kappa) \begin{pmatrix} 1 - g_1 & -g_2 \\ -g_2 & 1 + g_1 \end{pmatrix}. \quad (2.50)$$

Actually the matrix in Eq. (2.50) is elliptical coordinate transformation.

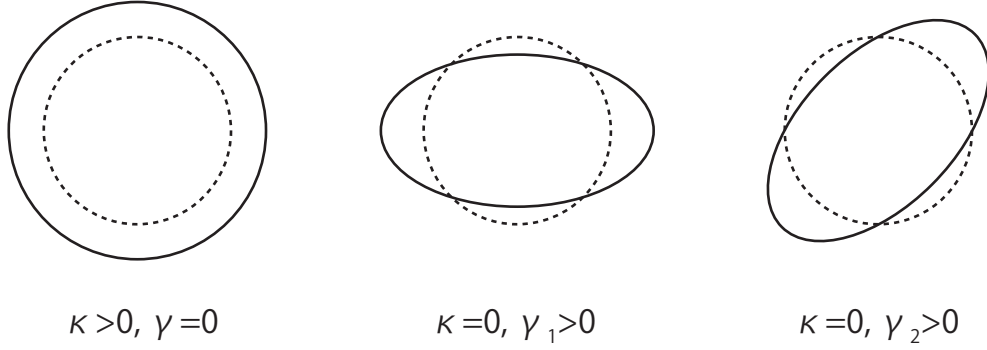


Figure 2.5: Illustration of how WL maps a source.

### 2.3.2 Cluster Mass Reconstruction

In this section, we show how the WL observable, shear, is connected to mass of a cluster.

First, convergence  $\kappa$  is related to mass density of the lens object projected to lens plane,  $\Sigma(D_l \boldsymbol{\theta})$ , via

$$\kappa(\boldsymbol{\theta}) = \frac{4\pi G}{c^2} \frac{D_{ls} D_l}{D_s} \Sigma(D_l \boldsymbol{\theta}) \quad (2.51)$$

$$\equiv \frac{\Sigma(D_l \boldsymbol{\theta})}{\Sigma_{\text{cr}}}, \quad (2.52)$$

where  $\Sigma_{\text{cr}}$  is called critical surface mass density.

Next, we reconstruct the convergence from observed shear. Taking a polar coordinate  $(\theta, \phi)$  whose origin is the center of cluster, we define E-mode,  $\gamma_+$ , and B-mode,  $\gamma_\times$ , as shown in Fig. 2.6.  $\gamma_+$  is the tangential/radial component. When it is tangential,  $\gamma_+$  is positive.  $\gamma_\times$  is the component rotated by 45 degrees from  $\gamma_+$ . In this coordinate, convergence and shear is written as

$$\kappa = \frac{1}{2} \left( \frac{\partial^2 \psi}{\partial \theta^2} + \frac{1}{\theta} \frac{\partial \psi}{\partial \theta} + \frac{1}{\theta^2} \frac{\partial^2 \psi}{\partial \phi^2} \right), \quad (2.53)$$

$$\gamma_+ = -\frac{1}{2} \left( \frac{\partial^2 \psi}{\partial \theta^2} - \frac{1}{\theta} \frac{\partial \psi}{\partial \theta} - \frac{1}{\theta^2} \frac{\partial^2 \psi}{\partial \phi^2} \right), \quad (2.54)$$

$$\gamma_\times = \frac{\partial}{\partial \theta} \left( \frac{1}{\theta} \frac{\partial \psi}{\partial \phi} \right). \quad (2.55)$$

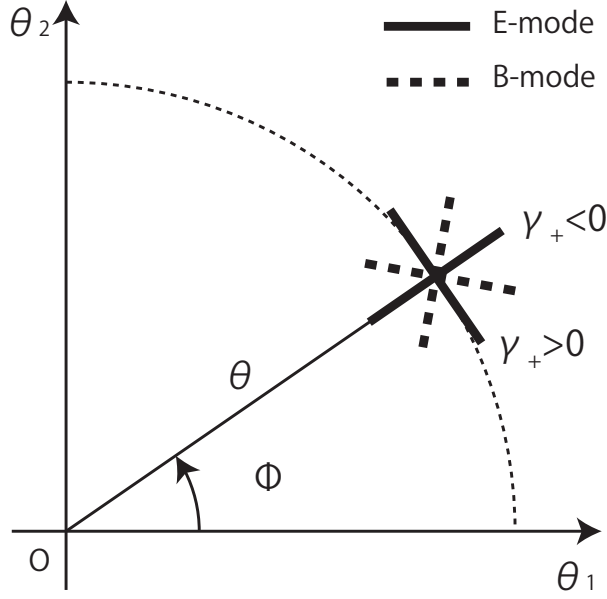


Figure 2.6: Definition of E-mode and B-mode.

The average of  $\gamma_+$  within an annulus  $[\theta, \theta + \delta\theta]$  yields

$$\langle \gamma_+ \rangle(\theta) \equiv \frac{1}{2\pi} \int_0^{2\pi} d\phi \gamma_+(\theta, \phi) \Big|_{\theta=\text{const.}} \quad (2.56)$$

$$= -\frac{1}{2} \left[ \frac{d^2 \langle \psi \rangle(\theta)}{d\theta^2} - \frac{1}{\theta} \frac{d \langle \psi \rangle(\theta)}{d\theta} \right], \quad (2.57)$$

where  $\langle \psi \rangle \equiv \int_0^{2\pi} \frac{d\phi}{2\pi} \psi$ . In a similar way,

$$\langle \kappa \rangle(\theta) = \frac{1}{2} \left[ \frac{d^2 \langle \psi \rangle(\theta)}{d\theta^2} + \frac{1}{\theta} \frac{d \langle \psi \rangle(\theta)}{d\theta} \right]. \quad (2.58)$$

Also we define the average of the convergence within a circle whose radius is  $\theta$  as

$$\bar{\kappa}(< \theta) \equiv \frac{1}{\pi\theta^2} \int_0^\theta \theta' d\theta' \int_0^{2\pi} d\phi \kappa(\theta', \phi) \quad (2.59)$$

$$= \frac{1}{\theta^2} \int_0^\theta d\theta' \frac{d}{d\theta'} \left( \theta' \frac{d \langle \psi \rangle(\theta')}{d\theta'} \right) \quad (2.60)$$

$$= \frac{1}{\theta} \frac{d \langle \psi \rangle(\theta)}{d\theta}. \quad (2.61)$$

Thus for arbitrary mass distribution, the following relation is satisfied;

$$\langle \gamma_+ \rangle = -\langle \kappa \rangle(\theta) + \bar{\kappa}(< \theta). \quad (2.62)$$

When  $\theta$  is sufficiently outside of the cluster,  $\langle \kappa \rangle \sim 0$ , so that Eq. (2.62) becomes

$$\langle \gamma_+ \rangle = \bar{\kappa}(< \theta) = \frac{\bar{\Sigma}(< \theta)}{\Sigma_{\text{cr}}}. \quad (2.63)$$

The projected mass of the cluster inside of  $\theta$  can be estimated as

$$M_{2\text{D}}(< \theta) = \pi (D_l \theta)^2 \Sigma_{\text{cr}}(\langle \gamma_+ \rangle). \quad (2.64)$$

This mass estimate is independent from model. We do not rely on any physical assumption such as hydrostatic equilibrium, and directly measure the mass including dark matter. However, There are two concerns. First, what we actually observe is *reduced shear*, not *shear* itself, as described in Section 2.3.1. Since the convergence is large around the center of the cluster, there is a discrepancy between reduced shear and shear. Second, since  $\langle \gamma_+ \rangle$  (or more precisely  $\langle g_+ \rangle$ ), is invariant under the transformation  $\kappa \rightarrow \kappa + \lambda$  ( $\kappa \rightarrow \lambda \kappa + (1 - \lambda)$ ) where  $\lambda$  is constant number, there also exists degeneracy when we estimate the cluster mass from shear.

Another important relation is that the average of B-mode becomes zero:

$$\langle \gamma_{\times} \rangle = 0. \quad (2.65)$$

This relation originates from the fact that gravitational lensing is induced by a scalar potential. This quantity can be used for a systematic test of analysis.

# Chapter 3

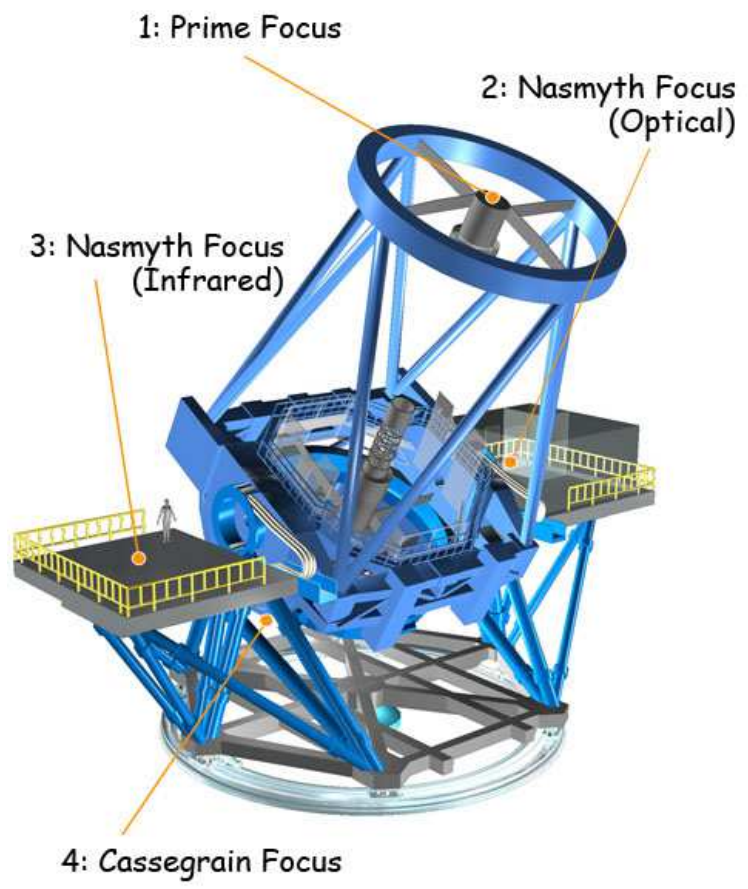
## Observational Apparatus

In this chapter we describe the observational apparatus of the Subaru Telescope/Suprime-Cam. The observatory is located at the summit of Mauna Kea, Hawaii. The Subaru Telescope/Suprime-Cam is a unique combination able to provide deep and wide imaging with high image quality, and has been leading wide field imaging astronomy.

### 3.1 Subaru Telescope

The Subaru Telescope [35, 1] is a 8.2-m optical-infrared telescope located at a latitude of  $19^{\circ}49'43''\text{N}$ , longitude of  $155^{\circ}28'50''\text{W}$ , and altitude of 4139m. The structure of telescope is shown in Fig. 3.1. It has a height of 22.2 m, width of 27.2 m, and weight of the moving assembly of 555 tonnes. The Subaru Telescope has four foci; a prime focus, Cassegrain focus, optical Nasmyth focus, and infrared Nasmyth focus. The wide-field prime focus where the Suprime-Cam is mounted, is a unique feature among 8-10 m telescopes, which offers a  $\sim 30'$  field of view with an excellent image quality better than  $0.''23$  and extremely small vignetting right up to the edge of the field.

The primary mirror is a monolithic mirror whose physical diameter is 8.3 m, thickness is 20 cm, and weight is 22.8 tonnes. The mirror is made of Ultra Low Expansion (ULE) glass coated with aluminum. The diameter of effective reflecting surface is 8.2 m and the focal length is 15 m, which corresponds to  $F/1.83$ . The reflectivity of a number of microscope slides, which was placed in the coating chamber together with primary mirror when the re-aluminization is conducted in August of 2010, is shown in Fig 3.2. They indicates the reflectivity of the primary mirror. The primary mirror is actively supported by 261 actuators which undistorts the mirror distortion induced by elevation angle (Fig. 3.3). The support force is updated every 100 ms. This feature allows for a mean surface error of 14 nm.



(c) MBTA Corporation, Japan. #150132

Figure 3.1: Schematic view of structure of Subaru Telescope.

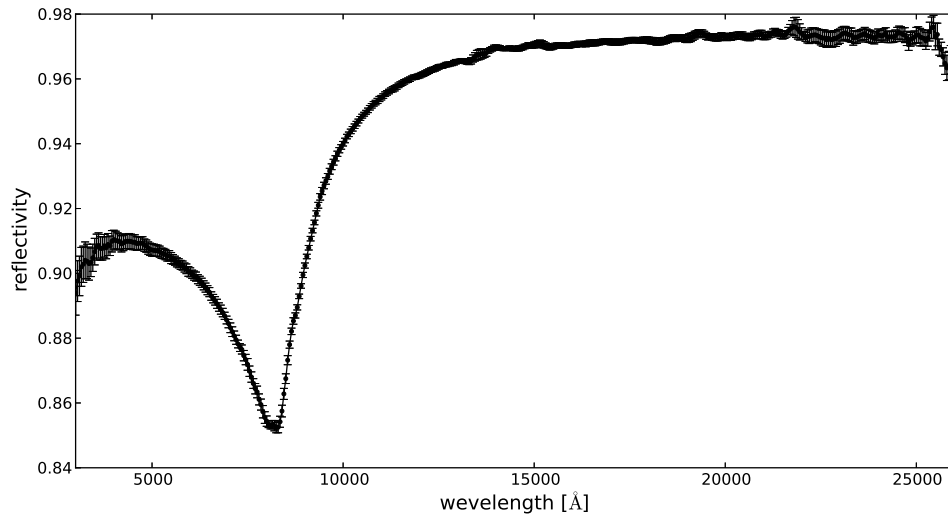


Figure 3.2: Indicative reflectivity of primary mirror, which is actually measured from microscope mirrors coated in the same condition as primary mirror in August, 2010.

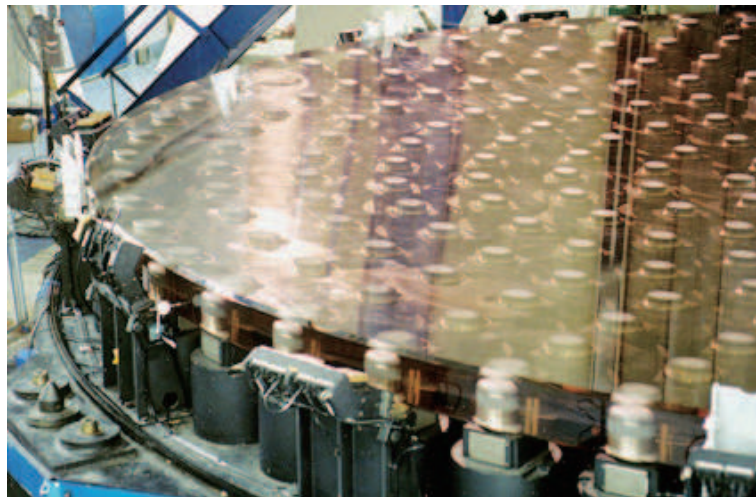


Figure 3.3: Picture of actuators which actively support the primary mirror.



Figure 3.4: Aerial view of Subaru enclosure.

The Subaru Telescope adopted a cylindrical enclosure rather than a traditional hemi-spherical dome as shown in Fig. 3.4. This helps to prevent the turbulent flow from growing along the enclosure and degrading observation condition. The height and diameter at base of the enclosure is 43 m and 40 m, respectively. The outer wall is covered with aluminum panels to reduce the temperature difference between the enclosure and the ambient air.

Although it is possible for the telescope to be pointed at elevation angles of  $89^\circ \geq El \geq 15^\circ$ , it is recommend to observe in elevation angles of  $85^\circ \geq El \geq 30^\circ$  to avoid fast movement of the telescope near to the zenith and extinction around lower elevation angles. The telescope can be slewed until  $270^\circ$  in each azimuth direction from south. The maximum slew rate of the telescope is  $0.5^\circ/\text{s}$ . The blind positioning error is less than  $1.0''$ . The field of view of auto guider camera is  $30''$  with the pointing accuracy of  $0.07''$ . The guiding error is less than  $0.1$  rms, including seeing effect, with a guide star brighter than magnitude 16.

Figure 3.5 shows statistics of FWHM seeing size measured by the auto guider camera. The median seeing is  $0.6\text{--}0.7$  FWHM. This figure shows that seeing of the later half of night is better. This is probably because better thermal equilibrium between the inside of enclosure and the ambient air is achieved. The clear sky ratio at the summit of Mauna Kea is around 60-80% according to statistics from May 2000 to 2011. The atmospheric transmittance curve at the summit in the case of

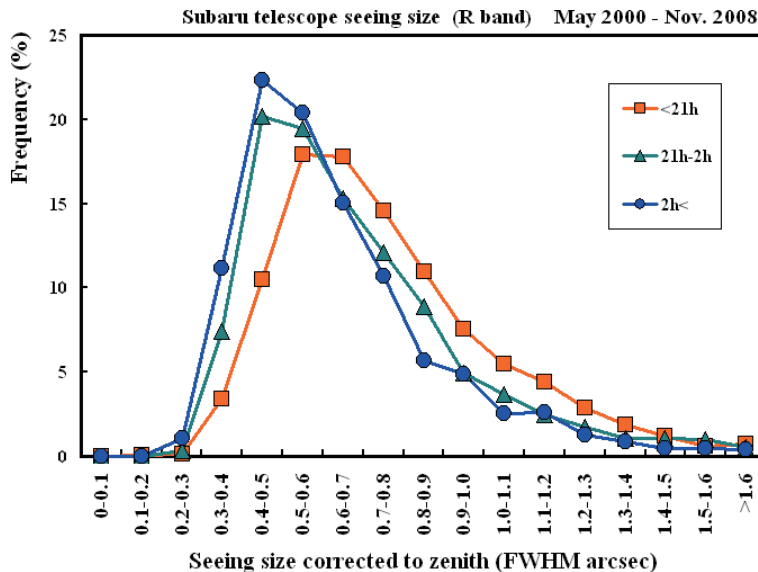


Figure 3.5: Seeing statistics measured by auto guider camera. The squares, triangles, circles show the measurement time before 21:00, 21:00-26:00, and after 26:00 Hawaiian standard time, respectively. The data was taken from May 2000 to Nov. 2008.

airmass<sup>1</sup> 1.2 is shown in Fig. 3.6<sup>2</sup>.

## 3.2 Suprime-Cam

### 3.2.1 Overview

The Suprime-Cam[60], which stands for **S**ubaru **P**rime Focus **C**amera, covers the field of view as wide as  $34' \times 27'$  with sub-arcsec imaging of  $0.''2$  per pixel, since it is mounted at the prime focus of the Subaru Telescope. The prime focus is a

<sup>1</sup>When measuring magnitude, atmospheric extinction is taken into account as

$$m(\lambda) = m_0(\lambda) + \kappa(\lambda)X(z), \quad (3.1)$$

where  $m(\lambda)$  is the magnitude of the observed object at the surface of the earth,  $m_0(\lambda)$  is the magnitude of the observed object after the light goes through the atmosphere,  $\kappa(\lambda)$  is called extinction coefficient, and  $X(z)$  is airmass. Airmass, which is a function of zenith distance of the object  $z$ , represents the number of times the quantity of the atmosphere along the line of sight to the object greater than the quantity of the atmosphere in the direction of zenith.  $X$  is approximated by  $\sec(z)$ . The second term can be calculated by integrating the atmospheric transmittance curve.

<sup>2</sup><http://www.astro.caltech.edu/~capak/cosmos/filters/>

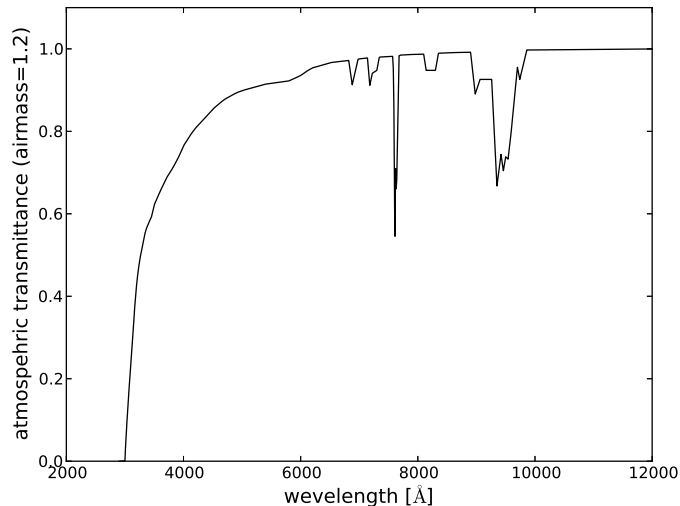


Figure 3.6: Atmospheric transmittance curve at the summit of Mauna Kea when airmass is 1.2.

notable and unique feature among 8-10 m class telescopes. While the seeing of the Suprime-Cam is routinely better than  $0.''7$ , which is one of the best seeing of ground-based telescopes and only 10 times larger than that of WFPC2 on board the Hubble Space Telescope, the Suprime-Cam realizes more than 100-times wider field of view than WFPC2. This feature has presented many unique opportunities to research in various fields. The picture of Suprime-Cam is shown in Fig. 3.7.

Since the Suprime-Cam saw first light in 1999, various components have been upgraded. The most major upgrade was done in July 2008, when its CCDs and electronics were replaced. In this section, we describe the latest specification of Suprime-Cam which was used for taking data in this thesis.

The schematic of Suprime-Cam which describes its main components is shown in Fig. 3.8. The prime focus unit (PFU) is mounted on the top ring of the telescope. The Suprime-Cam is loaded from the top of the PFU. The light reflected from the 8.2-m primary mirror first goes through the optics called wide field corrector, and then comes into Suprime-Cam. The wide field corrector is fixed to the PFU, while the camera is rotated by an instrument rotator together with an auto-guider. The design of the wide field corrector consists of three main lens and atmospheric dispersion corrector (ADC). The ADC corrects chromatic aberration especially caused when effective thickness of atmosphere becomes larger at lower elevations, which realizes high image quality across the field while maintaining  $34' \times 27'$  field of view. For instance, at a zenith distance of  $60^\circ$  or less, the diameter which contains 80%

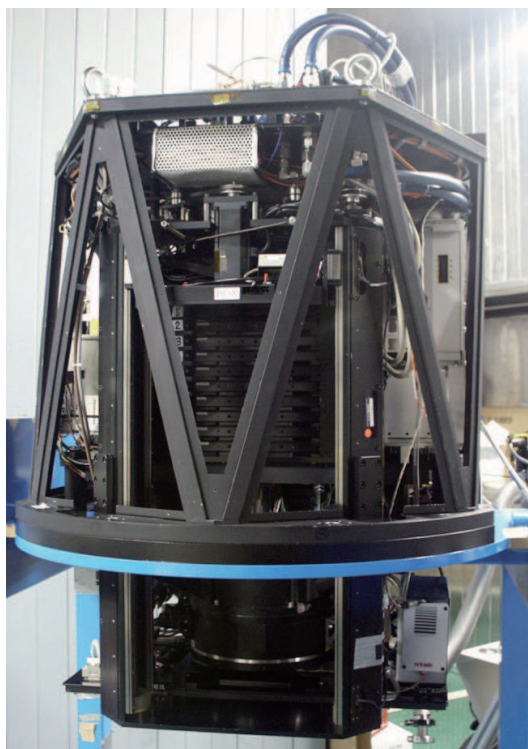


Figure 3.7: Picture of Suprime-Cam.

of energy of a point source on an image plane is less than  $22 \mu\text{m}$  ( $0.''30$ ) for the wavelength of 400 nm,  $13 \mu\text{m}$  ( $0.''18$ ) for the wavelength of 546.1 nm, and  $23 \mu\text{m}$  ( $0.''31$ ) for the wavelength of 1000 nm. The transmittance of the wide field corrector is shown in Fig. 3.9.

The shutter has two sliding doors. The one is used when opening the shutter and the other is used when closing the shutter, which makes the exposure time uniform over the field of view. The shortest exposure time is 1.2 s.

Then the light goes through a filter and photons having a certain range of wavelength are selected. The Suprime-Cam adopts two photometric filter systems; the one is the Johnson-Morgan-Cousins system [38][25][12], and the other is Sloan Digital Sky Survey (SDSS) system[30]. The available broadband filters are  $B$ ,  $V$ ,  $R_c$ ,  $I_c$  from the Johnson-Morgan-Cousins system, and  $g'$ ,  $r'$ ,  $i'$ ,  $z'$  of the SDSS system. In addition, a redder filter called  $Y$  which covers around  $10000 \text{ \AA}$  was added. The actual filter response is shown in Fig. 3.10.

Finally, the light arrives at CCDs through a window of the dewar. 10 CCDs are mounted on a focal plane which is actively cooled down to  $-100^\circ\text{C}$  inside of the dewar to suppress dark current of the CCDs. A cooler and vacuum device are used to realize the temperature. Holes converted from the photons are read-out from the CCD, and then are processed and converted into digital signal in the readout electronics called Mfront2[67]. The CCDs and readout electronics were replaced in July 2008, as described above. The digitized signal is then comes into the CCD/Instrument Controller called Messia-V[66], and then sent to the remote workstation in the observation room via Gigabit Ethernet. Details of CCDs, Mfront2, and Messia-V are described in Section 3.2.2. The length of the cable is required to be about 500 m long, so that optical fiber is employed. The remote workstation is connected to the data archive system where the data is actually stored. It is also connected to the telescope control system.

### 3.2.2 CCD and Electronics

The Suprime-Cam employs 10 chips of p-type  $2k \times 4k$  fully-depleted CCD, which is developed by the collaboration of NAOJ and Hamamatsu Photonics K.K (HPK)[41], to cover  $34' \times 27'$  field of view. Figure 3.11 shows the alignment of the CCDs on the focal plane. The gap between neighboring CCDs is  $14'' - 16''$ . Each CCD has DET\_ID, which is a one-digit detector ID, and DETECTOR, which is a name of detector.

The specification of the CCD is summarized in Table 3.1. Each CCD has 4 outputs, and each output reads out  $512 \times 4096$  pixels. The operating temperature is set to  $-100^\circ\text{C}$  to suppress dark current, as described in the previous subsection, which realizes the dark current of a few e/hour/pixel.

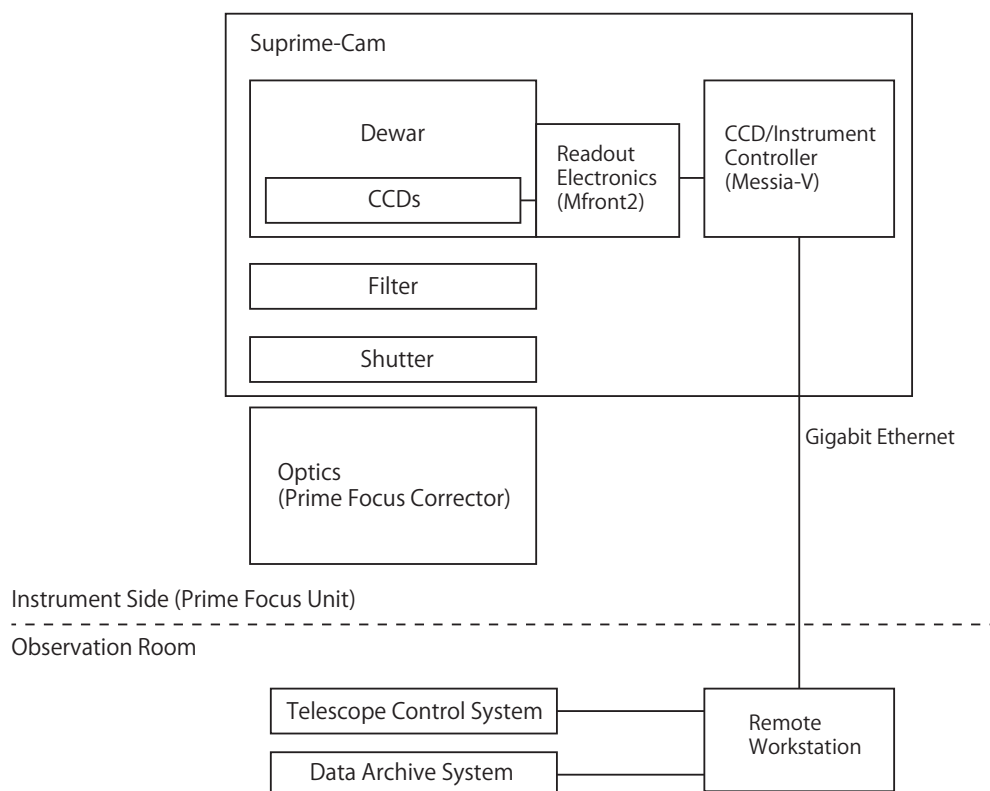


Figure 3.8: Schematic of Suprime-Cam.

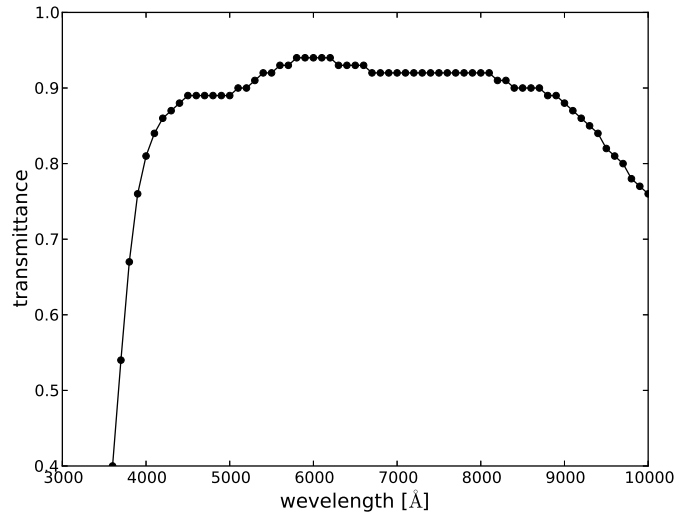


Figure 3.9: Transmittance of wide field corrector.

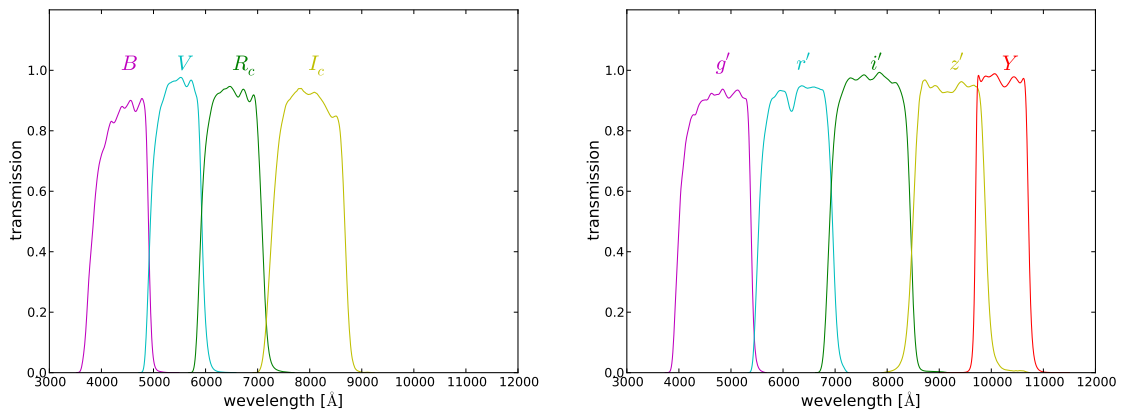


Figure 3.10: Actual filter response of Suprime-Cam. (*left*):  $B$ ,  $V$ ,  $R_c$ ,  $I_c$  from the Johnson-Morgan-Cousins system. (*right*):  $g'$ ,  $r'$ ,  $i'$ ,  $z'$  from the SDSS system. The reddest band  $Y$  is added.

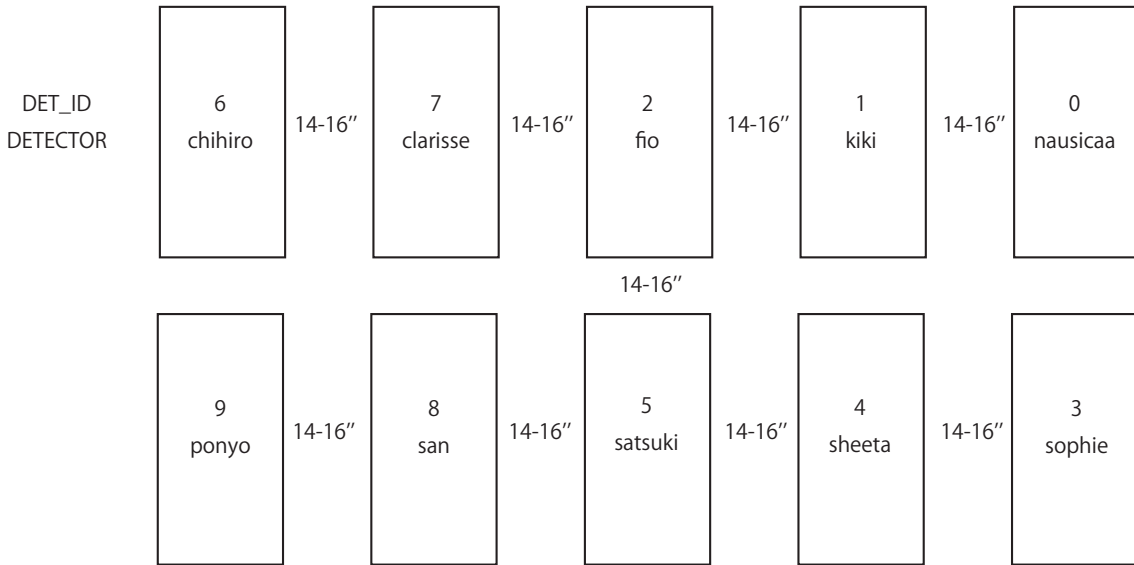


Figure 3.11: Alignment of CCDs on the focal plane of Suprime-Cam.

The CCD is back illuminated and fully depleted to realize high quantum efficiency (QE). Figure 3.12 shows QE of CCDs. The solid line denotes QE of a CCD currently used by the Suprime-Cam, while dashed line denotes a CCD used by the Suprime-Cam until July 2008 which was manufactured by MIT Lincoln Laboratory (MIT/LL). Although the MIT/LL CCD is also back illuminated and depleted, HPK CCD realizes 40% higher QE at redder wavelength. This is because HPK CCD adopts thicker depletion; HPK CCD has 200  $\mu\text{m}$  thick, while MIT/LL has 40  $\mu\text{m}$  thick.

The Messia-V issues CCD readout clock following the command from the remote workstation in the observation room. The readout clock is driven by the Mfront2 and sent to the CCDs. Signals from each CCD output come out of the dewar and comes back to Mfront2. First, the signals are amplified by a factor of 3.0, processed in correlated double sampling (CDS) to remove kTC noise, and digitized into 16 bit by analog digital converter (ADC). The integration period of CDS is set to 2  $\mu\text{s}$ . The conversion factor, or gain of CCD, is  $\sim 3.0$  e/ADU. Finally the digitized signals are sent to the Messia-V, sent to the remote workstation via the Gigabit Ethernet, and stored in the data archive system in fits format<sup>3</sup>. The current readout speed is set to 133 kpixels/sec with the 2 $\mu\text{s}$  of the CDS integration period, which realizes 18 sec for reading out a whole exposure. The total readout noise of the CCD and readout electronics is  $\sim 10$  e. The nonlinearity of the system is shown in Fig. 3.13.

<sup>3</sup>[http://fits.gsfc.nasa.gov/fits\\_standard.html](http://fits.gsfc.nasa.gov/fits_standard.html)

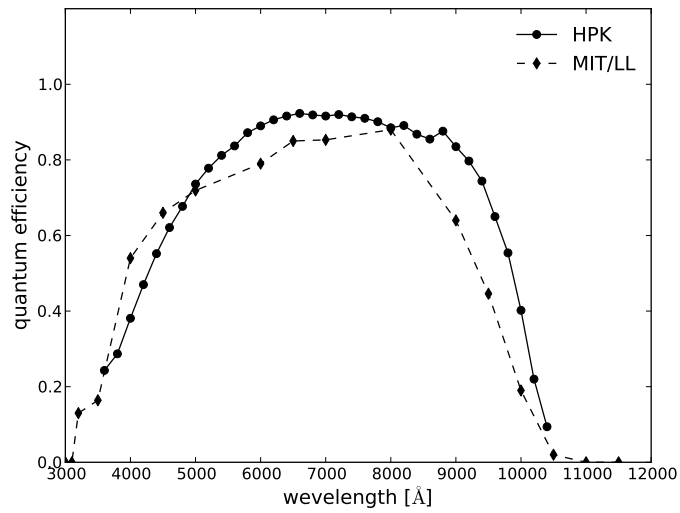


Figure 3.12: Quantum efficiency of CCD. Solid line denotes quantum efficiency of CCD used by Suprime-Cam which was upgraded in July 2008. This CCD was manufactured by Hamamatsu Photonics K.K. Dashed line denotes quantum efficiency of CCD used by Suprime-Cam before the upgrade, which was manufactured by MIT Lincoln Laboratory.

Format		2048×4096
Pixel size		15 $\mu$ m
Pixel scale		0."2
Signal outputs		4
Charge transfer efficiency	0.999999(parallel), 0.999998(serial)	
Node sensitivity		$\sim 5\mu$ V/e
Full-well capacity		>150,000e
Operating temperature		-100°C
Dark current at operating temperature		a few e/hour/pixel

Table 3.1: Specification of CCD employed by Suprime-Cam.

This shows the nonlinearity mainly comes from the CCD. The specification of the readout system is summarized in Table. 3.2

Number of CCD		10
Number of total signal outputs		40
Readout speed	133 kpixels/sec/output	
Readout time		18 sec
Data resolution		16 bit
Image size		173 Mbytes
Data rate		10 Mbytes/sec
Gain		2.5-3.7 e/ADU
Readout noise		10 e

Table 3.2: Specification of Suprime-Cam readout system.

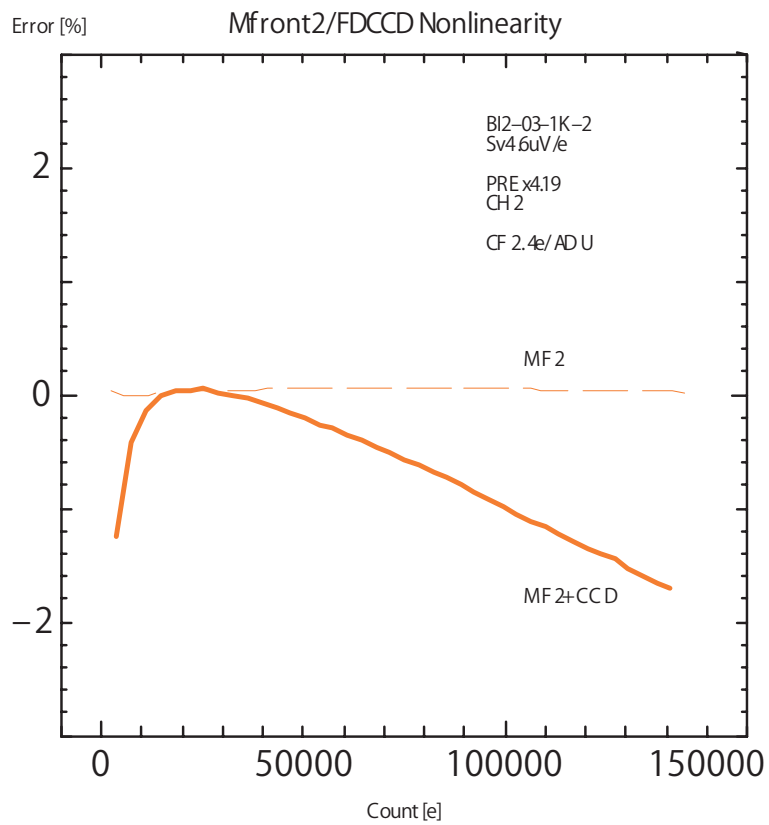


Figure 3.13: Nonlinearity of Suprime-Cam readout system. Dashed line denotes the nonlinearity of MFront2. Solid line denotes nonlinearity combined with a CCD.

# Chapter 4

## Development of High Precision Weak Lensing Measurement Algorithm

### 4.1 General Description of Weak Lensing Measurement

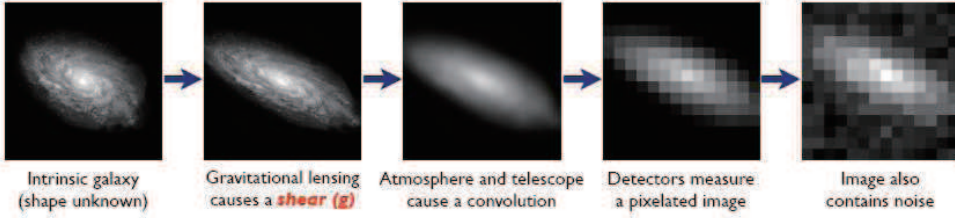
In this section, we describe a procedure to measure the distortion effect due to WL, so-called shear. We focus on a general procedure which is commonly done by WL measurement. The shearing effect due to WL is small and hidden by the intrinsic ellipticity of a galaxy. Thus one cannot obtain the shear from a single galaxy. Shear is extracted by averaging ellipticities of an adequate number of galaxies to cancel out their intrinsic ellipticities. We first describe how to measure ellipticity of a observed galaxy image in Section 4.1.1, and then how to extract the shear signal from the ensemble of galaxy ellipticities in Section 4.1.2

#### 4.1.1 Measuring Ellipticity of Each Galaxy Image

Figure 4.1 shows a forward process, i.e., how an object is observed after it is sheared by WL and/or affected by other observational effects. A galaxy having intrinsic shape is sheared by WL. Mathematically this is an elliptical coordinate transformation as described in Eq. (2.50). When the light passes through the atmosphere (unless the telescope is in space) and optics, photons are scattered. As a result, the image is smeared and distorted. Emission from the sky and detector noise causes a background which is added to the whole image. The detector sums up the photons in each pixel. The observed image is noisy due to Poisson noise in the number of photons coming into each pixel. The atmospheric dispersion, optical aberration, and

## The Forward Process.

**Galaxies:** Intrinsic galaxy shapes to measured image:



**Stars:** Point sources to star images:

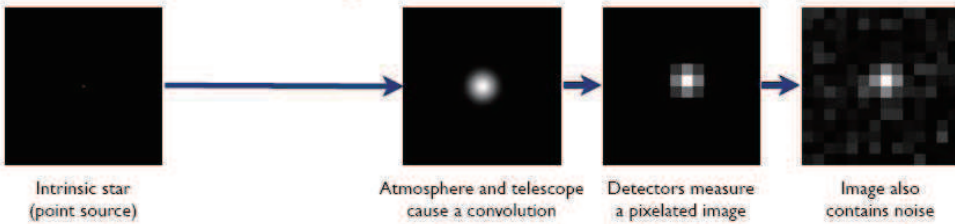


Figure 4.1: Illustration of forward process. This figure is taken from Bridle et al. [15].

pixelation is called the point spread function (PSF)<sup>1</sup>, which is mathematically represented by convoluting a kernel to the sheared galaxy. Note that optical distortion is not convolution, so that it should be treated as coordinate transformation.

The atmospheric dispersion and optical aberration smears and distorts the galaxy image. Thus it is necessary to correct PSF to obtain galaxy ellipticity. For correction of PSF, star images are used. Stars are considered to be a delta function so that stellar images are the impulse response of PSF. In general, any weak measurement method extracts shape information from PSF such as second order moments, and then perform PSF correction.

### 4.1.2 Extracting Weak Lensing Signal

Suppose that one has galaxy ellipticities after PSF correction. Shear signals can be extracted by averaging the ellipticities to cancel out the intrinsic ellipticities galaxies have.

However, before going into details, let us define ellipticity in different ways.

<sup>1</sup>There is another definition which does not include the pixelation into PSF. In this thesis, We treat this effect as a part of PSF.

Given that an ellipse has major axis  $a$  and minor axis  $b$ , ellipticity can be defined as

$$g = \frac{a - b}{a + b}. \quad (4.1)$$

Note that this is same as WL shearing effect, i.e, reduced shear  $\mathbf{g}$  as defined in Section 2.3.1. We call this definition *shear* with italics. Another possible definition is

$$e = \frac{a^2 - b^2}{a^2 + b^2}, \quad (4.2)$$

which corresponds to a quantity derived from second order moments measured on the ellipse

$$e = \frac{I_{xx} - I_{yy}}{I_{xx} + I_{yy}}, \quad (4.3)$$

where the direction of  $x$ -axis is taken along the major axis. We call the definition *distortion* with italics. There is a useful equation to convert between them;

$$g = \tanh \left( \tanh^{-1} (e) / 2 \right). \quad (4.4)$$

Since the shearing effect is an elliptical coordinate transformation, the observed ellipticity  $\mathbf{e}'$  can be written as

$$\mathbf{e}' = \mathbf{e} \oplus \boldsymbol{\delta}, \quad (4.5)$$

where  $\mathbf{e}$  and  $\boldsymbol{\delta}$  is the intrinsic ellipticity of the galaxy and lensing shear, respectively. We use  $\oplus$  as the addition operator for ellipticity and shear. Note that this operation corresponds to applying a coordinate transformation twice, so that it is no longer a simple linear operation. When the ellipticity, or shear, is defined in *distortion*, and each component is represented as

$$\mathbf{e} = (e_1, e_2) = (e \cos 2\theta, e \sin 2\theta), \quad (4.6)$$

where  $\theta$  is position angle, Eq. (4.5) is written as

$$e'_1 = \frac{e_1 + \delta_1 + (\delta_2/\delta^2) [1 - \sqrt{1 - \delta^2}] (e_2\delta_1 - e_1\delta_2)}{1 + \mathbf{e} \cdot \boldsymbol{\delta}}, \quad (4.7)$$

$$e'_2 = \frac{e_2 + \delta_2 + (\delta_1/\delta^2) [1 - \sqrt{1 - \delta^2}] (e_1\delta_2 - e_2\delta_1)}{1 + \mathbf{e} \cdot \boldsymbol{\delta}}, \quad (4.8)$$

which is derived by Miralda-Escude [59]. Next, we define the shear estimator as

$$\hat{\boldsymbol{\delta}} = \langle \mathbf{e}' \rangle. \quad (4.9)$$

Note that the shear estimator does not give shear itself since adding ellipticities is not simple linear addition as shown in Eq. (4.7) and (4.8). Given that  $\delta \ll 1$ , we consider how to approximate shear up to the first order. Taylor expansion of Eq. (4.9) is

$$\hat{\delta} = \langle e \rangle + \left. \frac{de'}{d\delta} \right|_{\delta=0} \delta \quad (4.10)$$

Since the distribution of galaxy shapes is assumed to be intrinsically isotropic, the first term of Eq. (4.10) is zero. Thus shear can be written as

$$\delta = \frac{\hat{\delta}}{\mathcal{R}}, \quad (4.11)$$

where  $\mathcal{R}$  is called responsivity. Note that when we assume isotropic distribution of galaxy shape,  $\mathcal{R}$  becomes scalar. When we adopt simple average for  $\langle \rangle$  in Eq. (4.9), the responsivity becomes

$$\mathcal{R} = 1 - \frac{\langle e^2 \rangle}{2}. \quad (4.12)$$

Here, we used Eq. (4.7) and (4.8). In the real measurement, the number of galaxies used for shear estimate is finite. Thus, statistical variance due to galaxy intrinsic shapes exists, which is written as

$$\text{Var}(\hat{\delta}) = \frac{\langle e^2 \rangle}{N}. \quad (4.13)$$

This noise is called shape noise, and is often a major source of error in cluster-galaxy lensing analysis. Note that the derived  $\delta$  is in the definition of *distortion*, so that we have to convert it into *shear* to obtain reduced shear.

In real analysis, since there is a measurement error of galaxy ellipticity, the responsivity can be optimized by down-weighting ellipticities having noisier measurement. In addition, it can be further optimized using the information of intrinsic galaxy distribution. For example, galaxies having larger ellipticity can be down-weighted compared to the ones with smaller ellipticity since the former has larger shape noise. Bernstein and Jarvis [10] derived the following optimum responsivity

$$\mathcal{R} = \frac{\sum \left[ w \left( 1 - k_0 - \frac{k_1 e^2}{2} \right) + \frac{e}{2} \frac{dw}{de} (1 - k_0 - k_1 e^2) \right]}{\sum w}, \quad (4.14)$$

where

$$k_0 = (1 - f) \sigma_{SN}^2, \quad (4.15)$$

$$k_1 = f^2, \quad (4.16)$$

$$f = \frac{\sigma_{SN}^2}{\sigma_{SN}^2 + \sigma_e^2}, \quad (4.17)$$

and  $w$  is weight function

$$w = \frac{1}{\sqrt{e^2 + (1.5\sigma_e/(1 - e^2))^2}}. \quad (4.18)$$

Here,  $\sigma_{SN}^2 = \langle e^2 \rangle / 2$ , where  $\langle \rangle$  denotes simple average and  $\sigma_e$  is measurement noise of each galaxy. Note that ellipticity appearing in these equations are in *distortion* definition. Although they assumed Gaussian distribution for intrinsic galaxy ellipticity, it is confirmed that this responsivity yields a few percent accuracy on shear estimate.

## 4.2 Overview of High Precision Weak Lensing Measurement Algorithm

In this thesis, we use the Elliptical Gauss-Laguerre (EGL) method originally developed by Bernstein and Jarvis [10] and modified by Nakajima and Bernstein [64] for galaxy shape measurement. Here we will briefly explain the method; for details, see the aforementioned papers.

### 4.2.1 Gauss-Laguerre Basis Functions

The EGL method attempts to extract shape information from any object by representing the observed image as a linear combination of complete orthogonal basis functions [also see 83, 54]. The basis function used in the EGL method is a set of Gauss-Laguerre (GL) basis functions, which is given in two-dimensional polar coordinates  $(r, \theta)$  with respect to the reference center:

$$\psi_{pq}^\sigma(r, \theta) = \frac{(-1)^q}{\sqrt{\pi}\sigma^2} \sqrt{\frac{q!}{p!}} \left(\frac{r}{\sigma}\right)^m e^{im\theta} e^{-r^2/2\sigma^2} L_q^{(m)}\left(\frac{r^2}{\sigma^2}\right) \quad (p \geq q), \quad (4.19)$$

where  $m \equiv p - q$  and  $L_q^{(m)}(x)$  are the Laguerre polynomials [3];

$$L_0^{(m)}(x) = 1, \quad (4.20)$$

$$L_1^{(m)}(x) = (m + 1) - x, \quad (4.21)$$

$$(q + 1)L_{q+1}^{(m)}(x) = [(2q + m + 1) - x]L_q^{(m)}(x) - (q + m)L_{q-1}^{(m)}(x). \quad (4.22)$$

The basis functions also satisfy  $\bar{\psi}_{pq}^\sigma = \psi_{qp}^\sigma$ , where  $\bar{\phantom{x}}$  denotes the complex conjugate. The lowest order function  $\psi_{00}^\sigma$  is a Gaussian function with width  $\sigma$ . In general, an

image (surface brightness distribution)  $I(\boldsymbol{\theta})$  is represented as

$$I(\boldsymbol{\theta}) = \sum_{p,q} b_{pq} \psi_{pq}^\sigma(\boldsymbol{\theta}). \quad (4.23)$$

Since  $I(\boldsymbol{\theta})$  is real, it can be proven that  $\bar{b}_{pq} = b_{pq}$ .

Figure 4.2 shows real parts and imaginary parts of the GL functions. The functions  $\psi_{pq}^\sigma$  with  $p = q$  are circularly symmetric, with  $p$  zero-crossing nodes in the radial functions. On the other hand, the functions  $\psi_{pq}^\sigma$  with  $p \neq q$  represent angular anisotropies; for example, the dipole anisotropies are described by  $\Re(\psi_{10}^\sigma)$  and  $\Im(\psi_{10}^\sigma)$ , and the quadruple anisotropies are by  $\Re(\psi_{20}^\sigma)$  and  $\Im(\psi_{20}^\sigma)$ , where  $\Re$  and  $\Im$  denotes real part and imaginary part of a complex number, respectively. Including the higher-order GL functions allows for more degrees of freedom to represent complex radial and angular dependencies of an image.

## 4.2.2 Modelling PSF

By using the orthogonal, complete set of GL basis functions (Eq. (4.19)), we can model an image of a star as

$$I^*(\boldsymbol{\theta}) = \sum_i b_i^* \psi_i^{\sigma^*}(\boldsymbol{\theta} - \boldsymbol{\theta}_0), \quad (4.24)$$

where we have used the collapsed notation  $i \equiv (p, q)$  for simplicity and  $\boldsymbol{\theta}_0$  is the centroid of a star. The coefficients  $b_i^*$  can be estimated via  $\chi^2$  fitting by comparing the observed image of a given star with the model;

$$\chi^2 = \sum_{\alpha=1}^{N_{\text{pix}}} \frac{[I^*(\boldsymbol{\theta}_\alpha) - \sum_i b_i^* \psi_i^{\sigma^*}(\boldsymbol{\theta}_\alpha - \boldsymbol{\theta}_0)]^2}{\sigma_\alpha^2}, \quad (4.25)$$

where  $\boldsymbol{\theta}_\alpha$  denotes the  $\alpha$ -th pixel in the image, the summation runs over pixels used in the fitting,  $\sigma_\alpha$  is the noise of the  $\alpha$ -th pixel. This fitting is a linear algebra problem, so the best-fit coefficients can be obtained analytically, which is computationally fast.

However, to do this  $\chi^2$  minimization, we must first determine the Gaussian width  $\sigma^*$  and the centroid for the basis functions. First, the width  $\sigma^*$  is computed by searching for the best-fit Gaussian function to the star image, varying the width parameter  $\sigma^*$ . Secondly, the centroid is determined by searching for the coordinate satisfying the condition  $b_{10}^* = 0$ , so that it does not have dipole. We use the ‘‘dogleg’’ algorithm [51] for this non-linear minimization, analytically calculating derivatives of  $b_{10}$  with respect to the centroid.

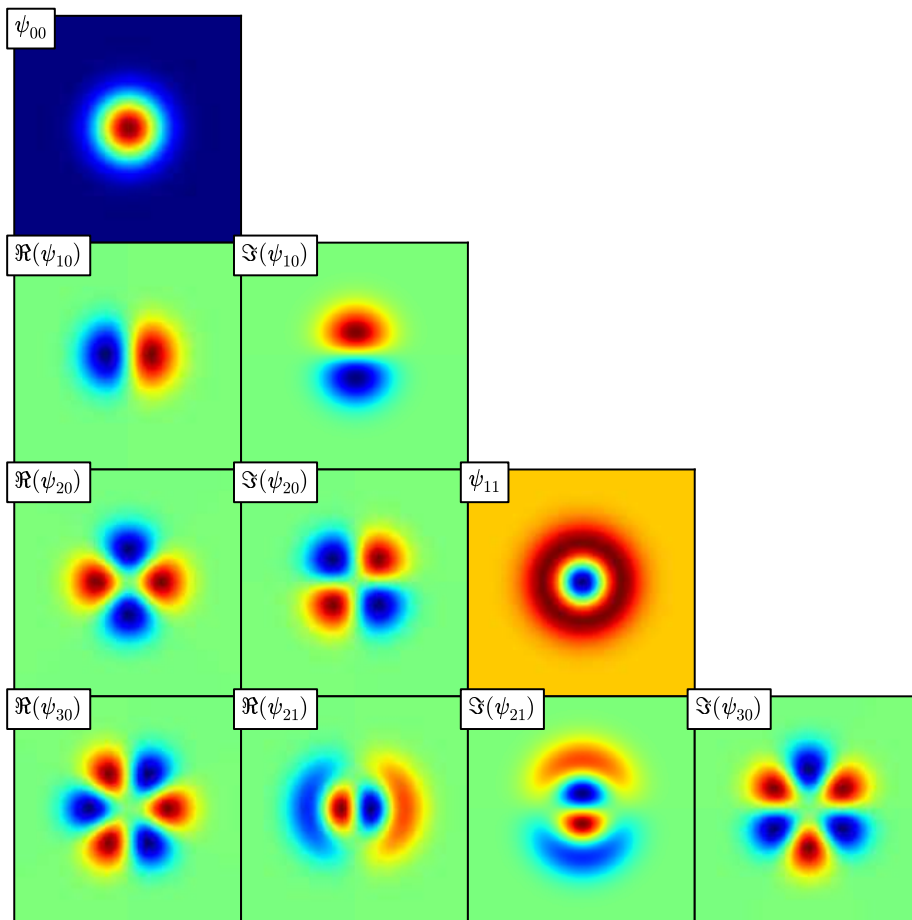


Figure 4.2: Gauss-Laguerre basis functions. They are used for modelling PSF.

In principle, any PSF can be represented by the GL expansion. However, in reality a typical PSF is more extended in the radial profile than the lowest-order GL basis functions (e.g., Gaussian), and it is necessary to include the GL functions up to much higher orders to adequately represent the stellar image.

### 4.2.3 Modelling Galaxy to Extract Shear Estimator

Given our PSF estimate, the ellipticity of a galaxy, which gives an estimator of weak lensing shear, is estimated as follows. Since the lensing shear distortion is equivalent to an elliptical coordinate transformation, a galaxy image is modelled in a *sheared* coordinate system rather than in the sky plane (the observed coordinate system). We can define a new set of basis functions in the new coordinate system via transformation:

$$\psi_i^{\sigma_g E}(\boldsymbol{\theta}) \equiv \psi_i^{\sigma_g}(\mathbf{E}^{-1}\boldsymbol{\theta}). \quad (4.26)$$

Here  $\mathbf{E}$  represents a coordinate transformation from the sky plane that includes a two-dimensional translation  $\mathbf{x}_0$ , a shear  $\mathbf{g}$ , and a dilution  $\mu$ :

$$\mathbf{E}^{-1}\boldsymbol{\theta} = \frac{e^{-\mu}}{\sqrt{1-g^2}} \begin{pmatrix} 1-g_1 & -g_2 \\ -g_2 & 1+g_1 \end{pmatrix} (\boldsymbol{\theta} - \mathbf{x}_0). \quad (4.27)$$

Thus the coordinate transformation is specified by 5 parameters. For instance, if an isophote of  $\psi$  is a unit circle, then the remapping  $\mathbf{E}$ , parametrized by  $\{\mathbf{x}_0, \mathbf{g}, \mu\}$ , leads the isophote of  $\psi^E$  to be an ellipse with center, ellipticity, and width given by the parameters  $\{\mathbf{x}_0, \mathbf{g}, \mu\}$ . Including the PSF convolution, an image of a galaxy is modelled as

$$I^{\text{model}}(\boldsymbol{\theta}) = \sum_{i,j} b_i^* b_j \left[ \psi_i^{\sigma_*} \otimes \psi_j^{\sigma_g E} \right] (\boldsymbol{\theta}), \quad (4.28)$$

where  $\otimes$  denotes convolution. In the equation above, we assumed that the PSF at the galaxy position can be properly obtained by interpolating the PSFs at positions of stars. Making use of the nature of this complete orthogonal system, the convolution of two GL functions can be carried out as follows:

$$\left[ \psi_i^{\sigma_*} \otimes \psi_j^{\sigma_g} \right] (\boldsymbol{\theta}) = \sum_k C_{ij}^k \psi_k^{\sigma_o}(\boldsymbol{\theta}), \quad (4.29)$$

where  $\sigma_o^2 = \sigma_g^2 + \sigma_*^2$ . To calculate the convolution in Eq. (4.28), we conform the coordinate of  $\psi^{\sigma_*}(\boldsymbol{\theta})$  to that of  $\psi^{\sigma_g E}(\boldsymbol{\theta})$  (i.e.  $\psi^{\sigma_g}(\mathbf{E}^{-1}\boldsymbol{\theta})$ ):

$$\psi_i^{\sigma_*}(\boldsymbol{\theta}) = \sum_j E_{ij}^{-1} \psi_j^{\sigma_*}(\mathbf{E}^{-1}\boldsymbol{\theta}). \quad (4.30)$$

For details of these two equations, see Bernstein and Jarvis [10] and Appendix B. Using these equations, the convolution in Eq. (4.28) is analytically calculated (although

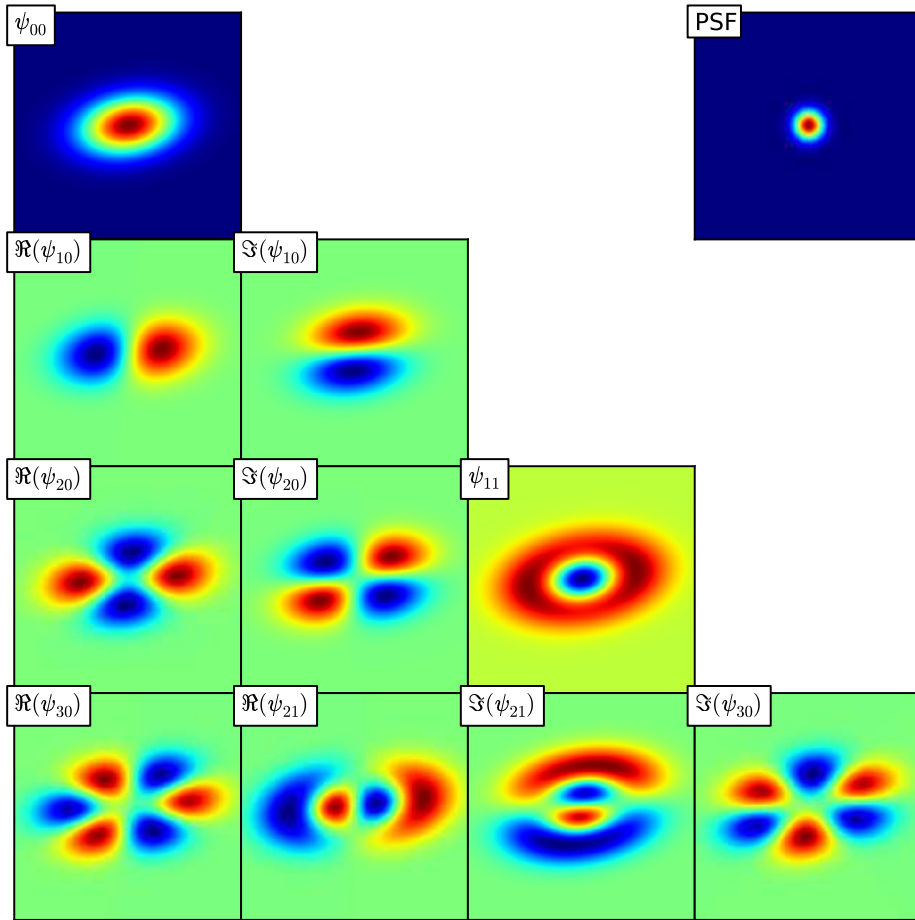


Figure 4.3: Elliptical Gauss-Laguerre basis functions convolved with PSF that is shown at upper right. They are used for modelling a galaxy.

a Jacobian depending on  $\mu$  exists due to the convolution in the *sheared* coordinate system, which can be absorbed in the galaxy coefficients  $b_i$ ). The observed galaxy image is fitted to the model shape as

$$\chi^2 = \sum_{\alpha=1}^{N_{\text{pix}}} \frac{[I^{\text{obs}}(\boldsymbol{\theta}_\alpha) - \sum_i b_i \Phi_i^{\sigma_o E}(\mathbf{b}^*; \boldsymbol{\theta}_\alpha)]^2}{\sigma_\alpha^2}, \quad (4.31)$$

where

$$\Phi_i^{\sigma_o E}(\mathbf{b}^*; \boldsymbol{\theta}) \equiv \sum_{jkl} b_j^* E_{jk}^{-1} C_{ki}^l \psi_l^{\sigma_o}(\mathbf{E}^{-1} \boldsymbol{\theta}). \quad (4.32)$$

This is a linear algebra problem, and therefore the  $\chi^2$  minimization for a given elliptical coordinate can be done via the linear algebra calculation to obtain the galaxy coefficients  $b_i$ , given the PSF coefficients  $b_i^*$ .

To find best fit parameters  $\{\mathbf{x}_0, \mathbf{g}, \mu\}$ , we carry out the circularity test that is defined in Nakajima and Bernstein [64] as follows. Relying on the fact that (in the weak lensing limit) a shear looks like an elliptical coordinate transformation of the galaxy image, we search for the elliptical coordinate for which the best-fit coefficients  $b_{20} = 0$  to find  $\mathbf{g}$ , where quadrupole anisotropy of the galaxy image vanish. Note that  $\Re(b_{20}) = 0$  and  $\Im(b_{20}) = 0$  corresponds to  $g_1 = 0$  and  $g_2 = 0$ , respectively. Similarly, the condition for finding  $\mathbf{x}_0$  and  $\mu$  is  $b_{10} = 0$  and  $b_{11} = 0$ . The former vanishes dipole anisotropy of the galaxy image on the elliptical coordinate, as used in PSF modelling, and the latter requires that the size of the galaxy is most confined to the lowest-order function, the Gaussian function with the coefficient  $b_{00}$ . In practice, we again use the ‘‘dogleg’’ algorithm for this non-linear least squares problem of finding the best-fit parameters ( $\sum_i |b_i|^2 = 0$ ), where  $i$  runs over coefficients which we want to constrain. To find the best-fit solution based on a numerical computation sufficiently quickly for each galaxy, the allowed tolerance is that the absolute value of real part and imaginary part of each coefficient should be smaller than  $10^{-5}$ :  $|\Re(b_{10})| < 10^{-5}$  and so on.

In practice, we fix the size parameter  $\mu$  in Eq. (4.31). This is needed especially for fitting galaxies as small as PSF. In this case, if we do not fix  $\mu$ , the fitter tries to shrink the model function to fit the central part of the object. However, the central part does not have enough number of pixels to give a shape information, which leads to misestimation of ellipticity. Instead of matching the size by minimizing Eq. (4.31) with changing  $\mu$ , we determine  $\sigma_g$  in Eq. (4.29) as follows and fix  $\mu$ . First, to estimate apparent (or observed) size, we fit the galaxy with non-convolved elliptical GL function by minimizing

$$\chi^2 = \sum_{\alpha=1}^{N_{\text{pix}}} \frac{[I^{\text{obs}}(\boldsymbol{\theta}_\alpha) - \sum_i b_i \psi_i^{\sigma_o^{\text{ini}} E}(\boldsymbol{\theta}_\alpha)]^2}{\sigma_\alpha^2}, \quad (4.33)$$

where  $E = \{\mathbf{x}, \mathbf{g}, \mu\}$  and  $\sigma_o^{\text{ini}}$  is the initial guess for the observed galaxy size which we set to 3.5 pixels, the typical size of PSF. Then we obtain apparent galaxy size,  $\sigma_o^{\text{ini}} e^\mu$ , and  $\sigma_g$  is calculated as

$$\sigma_g^2 = (\sigma_o^{\text{ini}} e^\mu)^2 - (f_p - 2) \sigma_*^2. \quad (4.34)$$

Here we introduced parameter  $f_p$  to further enlarge the galaxy size. Note that  $f_p = 1$  gives the galaxy size naturally defined from observed galaxy size and PSF size if Gaussian profile is assumed for them. We use  $f_p = 1.2$  as a default value to enlarge galaxy size. The effect of  $f_p$  will be discussed in Section 4.3.3.

#### 4.2.4 Covariance and Signal-to-noise Ratio

Since we carry out linear  $\chi^2$  minimization for both of the PSF fitting and galaxy fitting to obtain  $\mathbf{b}$ , the covariance of  $\mathbf{b}$  is estimated as

$$\text{Cov}(b_i, b_j) = [A^{-1}]_{ij}, \quad (4.35)$$

where

$$A_{ij} \equiv \sum_{\alpha}^{N_{\text{pix}}} \frac{I_i^{\text{model}}(\boldsymbol{\theta}_\alpha) I_j^{\text{model}}(\boldsymbol{\theta}_\alpha)}{\sigma_\alpha^2}. \quad (4.36)$$

Here  $I_i^{\text{model}}$  is the model basis functions of PSF or galaxy described above. Then this covariance is propagated to that of fitting parameters  $\mathbf{E} = \{\mathbf{x}_0, \mathbf{g}, \mu\}$  as

$$\text{Cov}(E_i, E_j) = \left( \frac{d\mathbf{b}}{d\mathbf{E}} \right)_{ik}^{-1} \text{Cov}(b_k, b_l) \left( \frac{d\mathbf{b}}{d\mathbf{E}} \right)_{jl}^{-1}. \quad (4.37)$$

Signal-to-noise ratio is defined as

$$\nu = \frac{f}{\sqrt{\text{Var}(f)}}, \quad (4.38)$$

$$f = \sum_p b_{pp}. \quad (4.39)$$

Note that  $f$  picks up all flux of the model.

#### 4.2.5 Summary of Elliptical Gauss-Laguerre Method

This EGL method is a so-called ‘‘forward-fitting method,’’ since the measured galaxy image is compared with a model image that is convolved with the PSF, where PSF is *a priori* estimated from images of stars. Hence this method does not involve a deconvolution of the seeing effect.

The advantage of this method is that any image can, in principle, be accurately modeled when including sufficiently high orders of the GL eigenfunctions. Another advantage of this method is, as emphasized in Nakajima and Bernstein [64], the forward-fitting procedure can handle pixelization, finite sampling, aliasing, and masking due to cosmic rays and bad pixels. Furthermore, the method can straightforwardly be extended to a simultaneous fitting of multiple exposures in modelling the images of the same galaxy, where the different PSFs in each image are properly taken into account.

However, when applying the method to real data, we can include only a finite set of basis functions and need to truncate the expansion at some order. More precisely, we have several truncations in our model fitting. First, for both the PSF and galaxy image fitting, we need to truncate the higher-order GL basis functions in the presence of noise. In the following, we will include the functions up to the  $N_{\text{PSF}}$ - or  $N_{\text{gal}}$ -th order, respectively (note that  $N_{\text{PSF}} = p + q$  in Eq. (4.19) and so on). Secondly, we employ the truncation for the GL basis functions used for the convolution and coordinate transformation in Eq. (4.29) and (4.30). These calculations involve the summation of the basis functions, and we do not necessarily stop at the same order used for the PSF and galaxy image fitting. We can instead include higher orders in the summations to achieve higher precision, and will include up to  $N_{\text{in}}$ -th order. These truncations generally cause systematic errors in modelling the object image [see also 14, 56, for a similar discussion].

## 4.3 Testing the Weak Lensing Measurement Algorithm

In this section we evaluate the accuracy of the EGL method by using simple images. The image of each object is in a separated tile, which allows us to avoid any effects of object blending. We made PSF and galaxy separately and then convolve the galaxy with the PSF. Several mathematical models are provided for generating the PSF and the galaxy. One can add weak lensing shear and make so-called “ring test” images which are convenient for testing the shape measurement accuracy. In addition, noise can be added to test S/N dependence of a shape measurement algorithm. In this section, we describe the concept of the ring test first, and then details about how to make a galaxy image convolved with the PSF.

### 4.3.1 Ring Test

The concept of the ring test was firstly proposed by Nakajima and Bernstein [64], and was used in the Shear TEsting Programme 2 (STEP2) that is a collaborative project to improve the accuracy and reliability of weak lensing measurement[55].

The ring test dramatically improves the efficiency of accuracy test of weak lensing measurement.

The main source of statistical error in “real” weak lensing measurements is the intrinsic ellipticity called “shape noise”. Assuming the orientation of galaxies are random and we have a finite number,  $N$ , of galaxies, the shape noise is naively<sup>2</sup> represented as

$$\sigma = \sqrt{\frac{\langle e_{\text{int}}^2 \rangle}{N}}, \quad (4.40)$$

where  $e_{\text{int}}$  is the intrinsic ellipticity of a galaxy. Given that the typical value of  $e_{\text{int}}$  is 0.3,  $\sim 10^7$  galaxies are needed for the accuracy test to reach up to  $10^{-4}$  level in ellipticity, which corresponds to testing 1% accuracy in typical cosmological weak lensing signals ( $10^{-2}$  level in ellipticity).

The ring test reduces the number of the galaxy by preparing two images of each galaxy whose ellipticity is  $\mathbf{e}_{\text{int}} \oplus \boldsymbol{\gamma}$  and  $-\mathbf{e}_{\text{int}} \oplus \boldsymbol{\gamma}$ , where  $\boldsymbol{\gamma}$  is weak lensing signal. When a shear estimate for two galaxies are averaged, the intrinsic ellipticity is cancelled out<sup>3</sup>, and thus statistical error only comes from measurement error that is propagated from photon noise of each pixel. For instance, when measurement error of a galaxy is 0.05, only  $\sim 10^5$  galaxies are required to sufficiently reduce the statistical error to  $10^{-4}$  level in ellipticity.

### 4.3.2 Image Simulation

#### Simulation of PSF Image

We employ the following two PSF models.

- Gaussian profile
- double Gaussian profile

The PSF of most ground-based telescopes is dominated by atmospheric turbulence, which can be described well by Kolmogorov statistics[29]. The Kolmogorov PSF has a wing outside of PSF due to the atmospheric dispersion. A simple and commonly used approximation for PSF is a Gaussian

$$G(r; \alpha) = \exp(-r^2/2\alpha^2), \quad (4.41)$$

---

<sup>2</sup>In real measurement, we often use weight function when summing up galaxy shapes. Thus the shape noise is no longer as simple as Eq.(4.40). However, this simplified equation will help to understand a benefit of ring test.

<sup>3</sup>More precisely, we need four galaxies whose intrinsic ellipticity is rotated by 45 degrees, which can be proven by using Eq. (4.7) and (4.8). However, this is needed only when one wants to investigate  $10^{-5}$  level in ellipticity.

which is not adequate to obtain an accurate modelling of a real PSF, since a single Gaussian is not able to model both the core and the wing of the PSF. However, we use a Gaussian profile for PSF modelling as the simplest case, which has the desirable property of being perfectly represented by the GL basis functions.

The more realistic and commonly-used PSF model is Moffat function[61]

$$M(r; \alpha, \beta) = \left[ 1 + \left( \frac{r}{\alpha} \right)^2 \right]^{-\beta}, \quad (4.42)$$

where  $\alpha$  represents the size of the PSF, and  $\beta$  denotes atmospheric dispersion. Note that in the limit of  $\beta \rightarrow \infty$ , a Moffat profile becomes a Gaussian<sup>4</sup>. A Moffat profile with  $\beta = 4$  can describe the Kolmogorov PSF better than a Gaussian. The sum of two Moffat functions, one with  $\beta = 7$  and the other with  $\beta = 2$ , can describe the wing of the PSF much better[81]. However, a single Moffat profile is most commonly used. Instead of a Moffat profile, we use the PSF model consisting of two Gaussians for the realistic PSF model;

$$I(r; \alpha) = G(r; \alpha) + f_I G(r; f_\alpha \alpha), \quad (4.43)$$

with values of  $f_I = 0.1$  and  $f_\alpha = 2^5$ . Hereafter we often define the size of the double Gaussian by FWHM of the first component,  $\text{FWHM}_1$ . In this case the flux of the 2nd component, which describes a PSF wing, amounts to 40% of that of 1st component. The double Gaussian with these parameters has been used as one of the PSF models in the pipeline of the SDSS. The three profiles are shown in Fig. 4.4. One can see a Gaussian profile does not have a wing, and a Moffat profile and a double Gaussian is close.

We simulate an image of the PSF as follows. We use the analytical PSF model above, and include ellipticity via the elliptical coordinate transformations:

$$x'_i = [\mathbf{E}^{-1}(\mathbf{e})]_{ij} x_j, \quad (4.44)$$

where  $\mathbf{x}' \equiv (x', y')$ ,  $\mathbf{x} \equiv (x, y)$  and

$$\mathbf{E}^{-1}(\mathbf{e}) \equiv \frac{1}{\sqrt{1-e^2}} \begin{pmatrix} 1-e_1 & -e_2 \\ -e_2 & 1+e_1 \end{pmatrix}. \quad (4.45)$$

Here  $(e_1, e_2)$  is the assumed ellipticity,  $(x, y)$  are the pixel coordinates and  $(x', y')$  are the coordinates in the sheared coordinate system in which the PSF looks circularly symmetric. That is, the circular isophote in the coordinates  $(x', y')$  is mapped to the elliptical isophote in the coordinates  $(x, y)$ , where the PSF value in each pixel is obtained by substituting the radius ( $r' = \sqrt{x'^2 + y'^2}$ ) into the analytical PSF model.

<sup>4</sup>If  $\alpha$  is fixed to  $\sqrt{2\beta}\sigma$  and then the limit of  $\beta \rightarrow \infty$  is taken, Eq. (4.42) becomes  $\exp(-r^2/2\sigma^2)$ .

<sup>5</sup>Representative values suggested by R. Lupton, priv. comm.

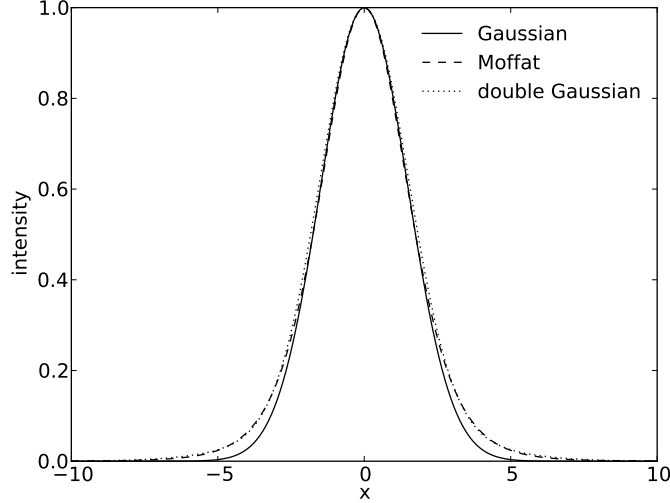


Figure 4.4: PSF profiles. FWHM is fixed to 3.5 pixels over all profiles. For a Moffat profile,  $\alpha$  is calculated from the FWHM and  $\beta = 4.0$ . For a double Gaussian,  $\text{FWHM}_1 = 3.5$  pixels,  $f_I = 0.1$ , and  $f_\alpha = 2.0$ . A Gaussian and a double Gaussian are used for this simulation.

### Simulation of Galaxy Image

For galaxy model, we employ exponential profile. We employ the following formalism;

$$I(r; r_e) = \exp\left(-1.6721 \left(\frac{r}{r_e}\right)\right). \quad (4.46)$$

Here  $r_e$  is the half light radius which is defined as distance from center satisfying

$$\frac{\int_0^{r_e} 2\pi r dr I(r)}{\int_0^\infty 2\pi r dr I(r)} = \frac{1}{2}. \quad (4.47)$$

Note that in Gaussian case,  $r_e$  is equal to a half of the FWHM.

We account for the intrinsic ellipticity and weak lensing shear as follows. In the weak lensing lensing limit, the shearing effect on a galaxy image is equivalent to an elliptical coordinate transformation. Therefore we can simulate a galaxy image including these two effects by mapping the analytic model via the elliptical coordinate transformation;

$$x'_i = [\mathbf{E}^{-1}(\mathbf{e})]_{ij} [\mathbf{E}^{-1}(\boldsymbol{\gamma})]_{jk} x_k, \quad (4.48)$$

in a similar manner as in Eq. (4.44), where  $\gamma$  is the ellipticity vector corresponding weak lensing shear.

Next, we include the PSF convolution by numerically convolving the galaxy image with the PSF in Fourier space. In this step, it is necessary to divide a pixel into finer pixels to carry out precise convolution. We generate a galaxy image and PSF image in the 25 times finer pixels than the target CCD pixel scale, and then convolve the galaxy image with the PSF image. The values at each CCD pixel center from the convolved galaxy image in the finer pixel coordinate are regarded as the hypothetically observed galaxy image. Here we assume that the PSF models already have pixelization, so that further calculation in finer pixel coordinates is not needed.

### Adding Noise

When including the pixel noise, we add random (uncorrelated) noise to each pixel assuming a Gaussian distribution in the sky noise limit. We also include the noise contribution from the object flux, i.e, the object plus sky photon counts, through the noise due to the object flux is only important for the high S/N objects. We will quantify the performance of our shape measurement method as a function of the S/N of a given PSF or galaxy image. We employ the total S/N for a given object defined in the same manner as in GREAT08[16]:

$$S/N = \frac{F}{\sigma_F} = \frac{\left[ \sum_i^{\text{pixels}} I(\mathbf{x}_i)^2 \right]^{1/2}}{\sigma_{\text{sky}}}, \quad (4.49)$$

where  $I(\mathbf{x}_i)$  is the object at the  $i$ -th pixel, and  $\sigma_{\text{sky}}$  is the rms of Gaussian sky noise assumed to be constant over all pixels representing a single star or galaxy. Once the S/N and sky noise level is specified for a given image, the normalization of the image flux can then be determined from Eq. (4.49). Examples of the generated image is shown in Fig. 4.5.

### 4.3.3 Results

#### Dependence on $N_{\text{gal}}$

**Test 1: Gaussian PSF** We begin with the simplest case, i.e., Gaussian PSF which is the lower order of the GL functions. We set the PSF FWHM to 3.5 pixel which corresponds to  $0.7''$  for the Suprime-Cam, the typical size of PSF. For galaxy profile, we use exponential profile with three cases of different size; the half light radius is half, equal, and one and half of that of PSF (0.875 pixel, 1.75 pixel, and 2.625 pixel, respectively). Also we prepared three cases of ellipticities, i.e., 0, 0.2,

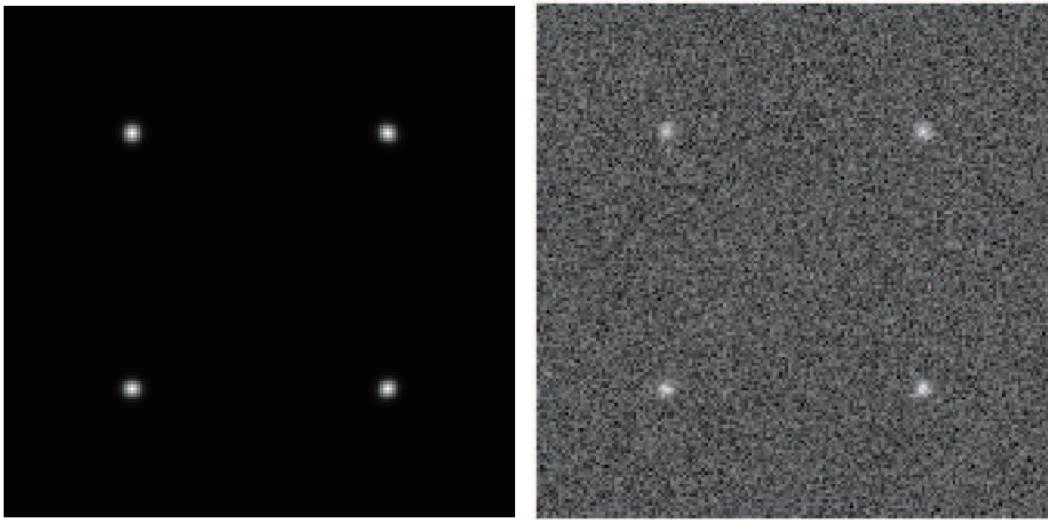


Figure 4.5: Exmaples of generated images for ring test. Exponential galaxies whose  $r_e = 0.875$  pixel and  $e = 0.1$  convolved with circular double Gaussian PSF whose  $\text{FHWM}_1=3.5$  pixel are shown. Left panel is images without noise, while right panel is images with noise ( $S/N = 20$ ). For each panel, a galaxy whose position angle is 0 deg, 45 deg, 90 deg, and 135 deg is shown in lower left, lower right, upper left, and upper right, respectively.

and 0.4. For each type of galaxies, we prepared four images whose position angle is 0 degrees, 45 degrees, 90 degrees, and 135 degrees to carry out the ring test. For all the rotated galaxies, we applied constant shear  $\mathbf{g} = (0.02, 0)$ . We did not add any noise on the images.

We applied the EGL method with  $N_{\text{PSF}} = 12$ ,  $N_{\text{in}} = 20$ , and  $f_p = 1.2$ , varying  $N_{\text{gal}}$ . Shear is estimated by using responsivity shown in Eq. (4.12). The result is shown in Fig. 4.6. The estimated first component of the shear whose input value is 0.02 is plotted as a function of  $N_{\text{gal}}$ . In general, as  $N_{\text{gal}}$  becomes higher, the shear estimate comes close to the right answer. This is because galaxy profile is more completely represented by the GL functions. It is difficult to obtain right answer when galaxies are small, especially when the galaxy size is smaller than that of PSF. This implies galaxy shape information is destructed by PSF. We can expect  $\sim 1\%$  shear recovery accuracy with  $N_{\text{gal}} = 8$  except for the larger ellipticity case ( $e=0.4$ ). With  $N_{\text{gal}} = 2$ ,  $\sim 8\%$  accuracy is expected.

**Test 2: Double Gaussian PSF and Effect of  $f_p$**  As a realistic PSF case, we test the EGL method with a double Gaussian profile whose  $\text{FWHM}_1 = 3.5$  pixel. Other setups are same as test 1. The results are shown in Fig. 4.7. For larger galaxies and smaller ellipticities, the EGL method still works well; it yields a few percent bias when  $N_{\text{gal}} = 8$ . However, for galaxies having smaller size and larger ellipticity, it is difficult to obtain the right answer with  $N_{\text{gal}} = 8$ . So we increased  $f_p$  to 3.0, whose result is shown in Fig. 4.8. For  $N_{\text{gal}} = 8$ , the EGL fit achieved a few percent accuracy. This is probably because we forced the model to fit the outer part of the galaxy that has rich information about the galaxy shape.

**Test 3: PSF Anisotropy** In reality, the PSF has anisotropy due to optical aberration. To test this, we added ellipticity (0.01, 0) to double Gaussian profile, which is half of the input shear. We tried  $f_p = 1.2$  and  $f_p = 3.0$ . Other settings for the EGL method are same as test 1. Figure 4.9 and Fig. 4.10 show the results for  $f_p = 1.2$  and  $f_p = 3.0$ , respectively. The difference from circular double Gaussian case is within a few percent.

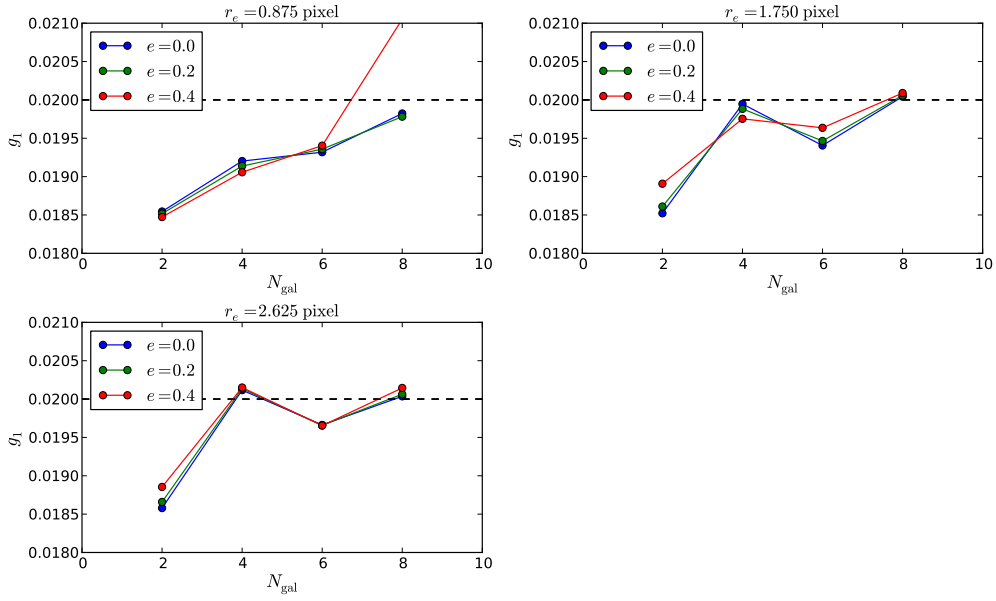


Figure 4.6: Shear recovery accuracy when PSF is Gaussian with FWHM=3.5 pixel as a function of  $N_{\text{gal}}$ , the order of GL function used for galaxy fitting. Other parameters of the EGL fit are fixed to  $N_{\text{PSF}} = 12$ ,  $N_{\text{in}} = 20$ , and  $f_p = 1.2$ . For galaxy model, exponential profile having various ellipticity and size is used. The half light radius of galaxy is set to half, equal, and one and half of that of PSF (0.875 pixel, 1.750 pixel, and 2.625 pixel, respectively). Input shear to the simulation image is (0.02, 0) as shown in dotted line.

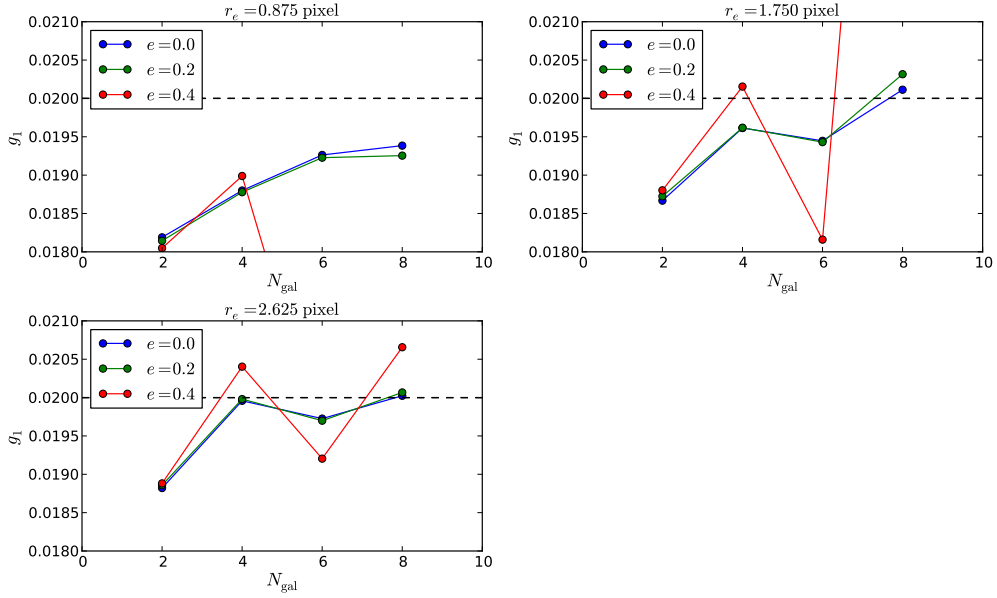


Figure 4.7: Same plot as Fig. 4.6, but PSF is double Gaussian profile whose FWHM of the first component is 3.5 pixel.

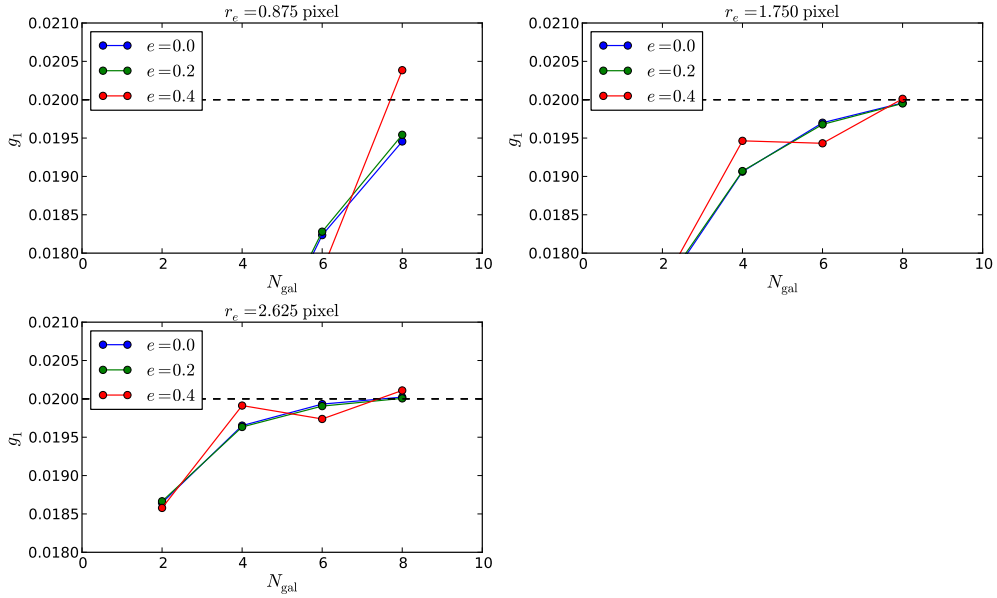


Figure 4.8: Same plot as Fig. 4.7, but  $f_p$  is increased to 3.0.

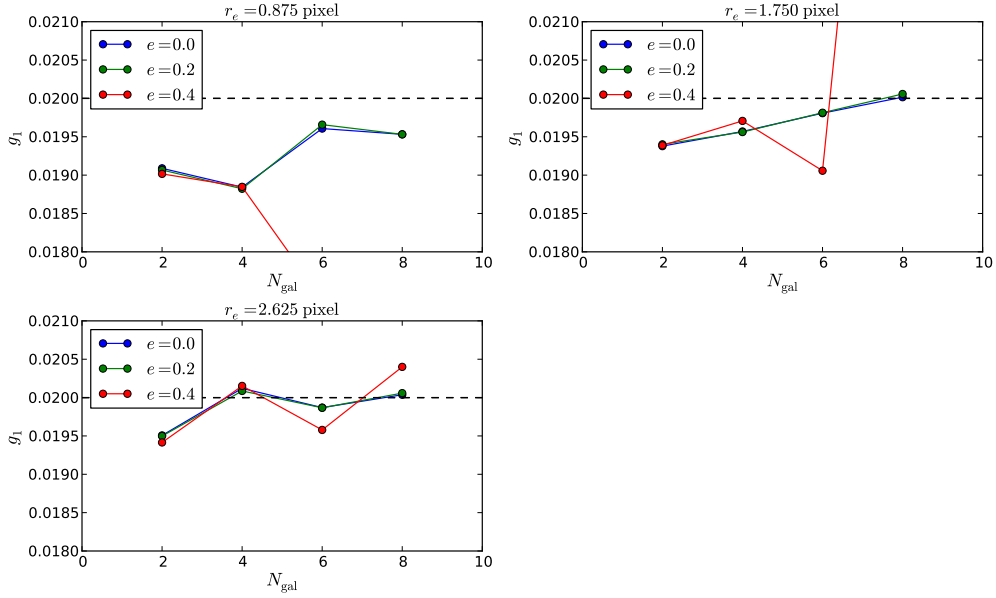


Figure 4.9: Same plot as Fig. 4.7, but PSF has anisotropy,  $e^* = (0.01, 0)$ . Note that the anisotropy is half of the input shear.

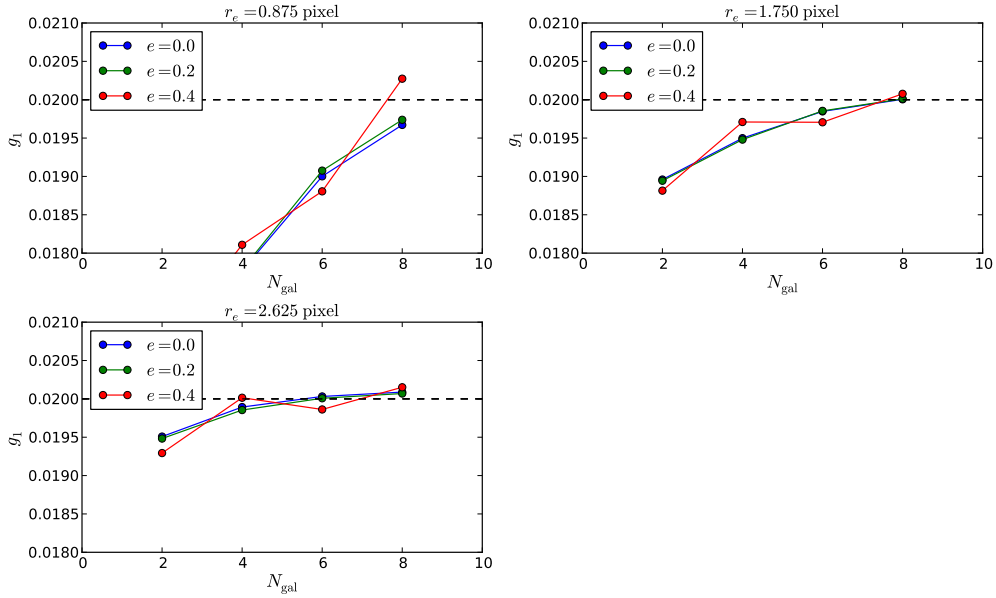


Figure 4.10: Same plot as Fig. 4.9, but  $f_p$  is increased to 3.0.

## How Well the GLs Can Describe PSF?

In this section we present how well the linear combination of the GLs can describe a realistic PSF, namely, a double Gaussian PSF with typical parameters  $(f_I, f_\sigma) = (0.1, 2)$  and  $\text{FWHM}_1 = 3.5$  pixels. The black-bold line in the upper panel of Fig. 4.11 is the double Gaussian used for our simulation, which is normalized by the peak of the profile. Although we used 2 dimensional profile for this study, of course, this figure shows a slice on  $y = 0$  plane for the illustrative purpose. The intensity falls down to  $10^{-3}$  times of the peak around 9 pixels from the center so that effect to the shear should become less outside of this region.

We then carried out fitting to the double Gaussian profile, using GLs in the same manner as described in Section 4.2.2. Note that this double Gaussian profile does not have noise for simplicity. Calculating linear combinations of the GL basis functions using the GL coefficients obtained by the fitting allows for reconstructing the modeled PSF profile. The residuals, the modeled PSF minus the double Gaussian PSF, are shown in upper panel of Fig. 4.11. We plot the several cases of  $N_{\text{PSF}} = 2, 4, 6, 8$ . We show even number of orders since radial basis functions, which will be used for representing the wing, are included only in them. There are “flips” when  $N_{\text{PSF}}$  is incremented, with getting close to the double Gaussian profile. This means the PSF model is gradually tuned to the real PSF. In addition,  $N_{\text{PSF}}$  goes higher the number of zero crossing points increases, since the number of zero crossing nodes of the radial basis functions also increases.

The lower panel of Fig. 4.11 shows the integrated value of the double Gaussian and each model as a function of radius from center.

$$F(r) = \int_0^r I(r') 2\pi r' dr' / F(r \rightarrow \infty), \quad (4.50)$$

where  $F(r \rightarrow \infty)$  is an integral of the double Gaussian / GL model itself over real space. From this figure, the GL model truncated at lower  $N_{\text{PSF}}$  estimates PSF smaller as shown in the region around  $r = 3 \sim 5$  pixels, which may cause underestimation of shear. From this figure, we decided the reliable  $N_{\text{PSF}}$  is 8 for double Gaussian PSF.

## With Noise

We tested the accuracy of the EGL method in presence of pixel noise. First we generated galaxy images in the same manner as the test 2 when we investigated dependence on  $N_{\text{gal}}$ , and added photon noise to each pixel of an image following Section 4.3.2. We tested three cases of  $S/N$ : 100, 50, 20, each of which has 80000 galaxies to reduce statistical error due to the pixel noise. For the parameters of the EGL method, we tried two extreme cases:  $(N_{\text{gal}}, N_{\text{PSF}}, N_{\text{in}}, f_p) = (2, 8, 12, 1.2), (8,$

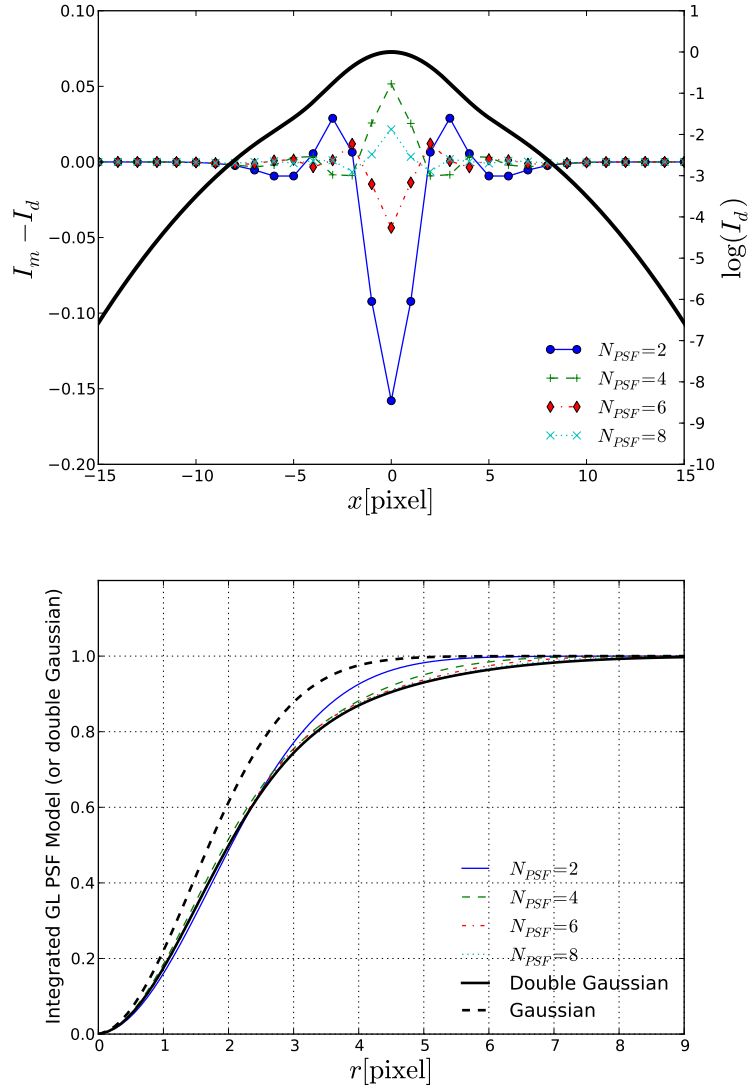


Figure 4.11: *upper panel*: A double Gaussian PSF profile (black-bold line) and the residual between PSF modeled by the GLs and the double Gaussian (other thin lines). The former is plotted in log scale as shown in the right vertical axis, while the latter is in linear scale. The double Gaussian profile is normalized by the peak of the profile, and configured with  $r_I = 0.1$ ,  $r_\sigma = 2$ , and  $\text{FWHM}_1 = 3.5$  pixels. Blue-solid, green-dashed, red-dashed-dotted, cyan-dotted lines show the case of  $N_{PSF}$  is 2, 4, 6, 8, respectively. *lower panel*: A double Gaussian profile and GL PSF model integrated from the center to radius  $r$ . Notations for lines are same as the upper panel.

12, 20, 3.0). Results for each case are shown in Fig. 4.12 and 4.13 as a function of  $S/N$ . Error bars come from photon noise. Together with the three  $S/N$  cases, the results when  $S/N$  of a galaxy image is infinity (or non-noise) are shown at  $S/N=150$ , which is same as the results shown in test 2 when we investigated dependence on  $N_{\text{gal}}$ .

When  $N_{\text{gal}} = 2$ , the bias on shear estimate is within  $\sim 10\%$  except for  $(r_e, S/N) = (0.875, 20)$ . They indeed fluctuate, but there are no drastic differences from galaxies without noise. The EGL method with  $N_{\text{gal}} = 8$  is extremely biased when  $S/N$  is small. For example, shear measurement on galaxies whose size is 0.875 pixel yields more than 10% bias except for a galaxy with  $(e, S/N) = (0, 100)$ . However, When galaxies have large size and small ellipticity, the results are less biased. For example when  $r_e = 0.265$  and  $S/N \geq 50$ , shear measurement on galaxies whose ellipticity is 0 or 0.2 still yield only a few % bias.

We guess the reason of the large bias in the case of  $N_{\text{gal}} = 8$  as follows. Higher order of the GLs extends towards outskirts than lower order, so they need shape information at outer radii of the galaxy. The fit with  $N_{\text{gal}} = 8$  works well when there is no noise, since the outer radii of a galaxy have shape information, although the amplitude is very small. However, when a galaxy image is noisy, the information at outer radii is hidden by the pixel noise, and makes it difficult for the fitter to converge correctly.

Another possible reason is so-called “noise rectification bias”, which is described by Hirata et al. [32]. The probability distribution function of the pixel noise is symmetric around zero, since this is Poisson noise of photons. However, the process to translate the pixel value into ellipticity is non-linear. Thus the probability distribution function of the ellipticity is no longer symmetric, and regarding the mean value as the representative value of the estimated ellipticity will cause bias.

Practically, for large and high signal-to-noise ratio galaxies, we are able to use the EGL method with  $N_{\text{gal}} = 8$ . However, the dominant source of shape measurement is statistical error due to shape noise as described in Section 4.1.2, which scales with  $1/\sqrt{N}$ , where  $N$  is the number of galaxies. In many cases we may want to use more galaxies to suppress the shape noise. Thus rather than using only large and high signal-to-noise ratio galaxies, we might want to use smaller and low signal-to-noise ratio galaxies. For these galaxies, we should use the EGL method with  $N_{\text{gal}} = 2$ . Although there is  $\sim 10\%$  bias, it can suffice when shape noise is still large like cluster-galaxy lensing analysis.

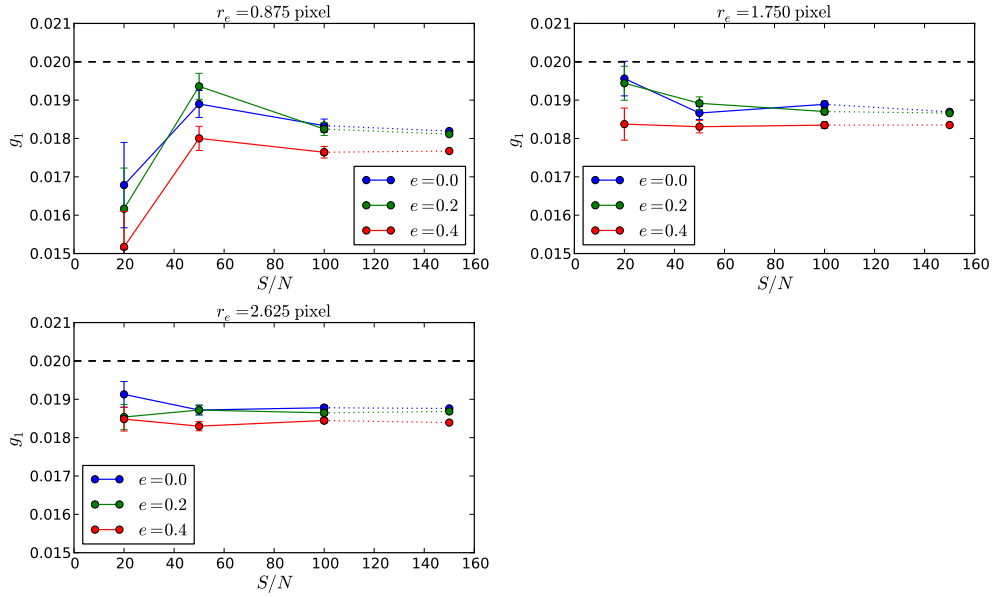


Figure 4.12: Configuration of the galaxy image is same as Fig. 4.7 except that noise is added as described in Section 4.3.2. Parameters of the EGL method are  $(N_{\text{gal}}, N_{\text{PSF}}, N_{\text{in}}, f_p) = (2, 8, 12, 1.2)$ . The dots at  $S/N = 150$  is not the value obtained by fitting a image with  $S/N = 150$ , but that without noise.

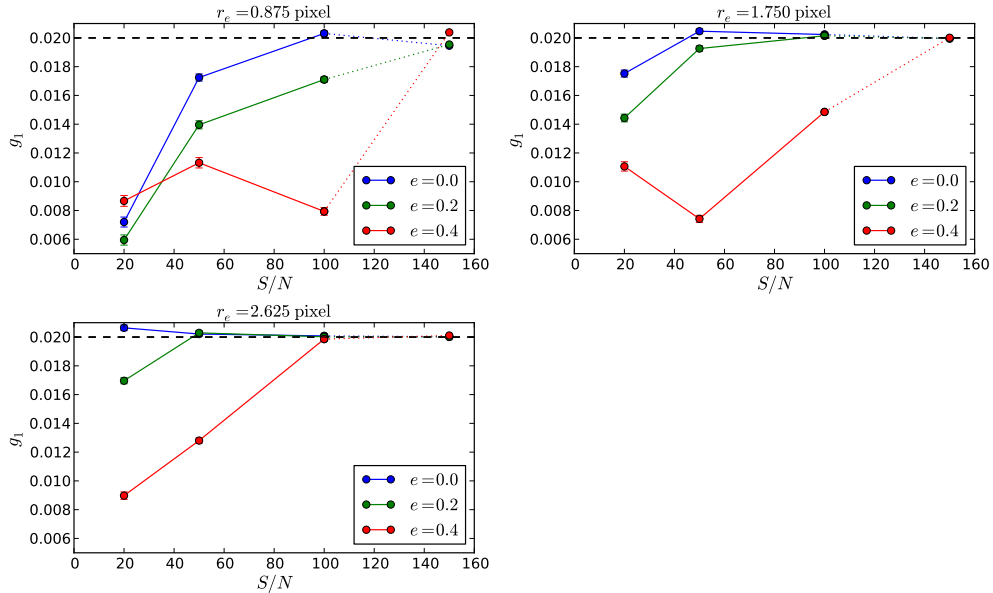


Figure 4.13: Same plot as Fig. 4.12, but parameters of the EGL method is  $(N_{\text{gal}}, N_{\text{PSF}}, N_{\text{in}}, f_p) = (8, 12, 20, 3.0)$ .

# Chapter 5

## Mass measurement of the High-redshift Massive Galaxy Cluster ACT-CL J0022-0036

### 5.1 Data

Our observations of ACTJ0022 were carried out at the Suprime-Cam[60] of the Subaru Telescope[35], which is a wide-field camera whose field of view is  $34' \times 27'$ . Images were taken on December 4, 2010. We took  $Br'i'z'Y$ -band, and  $i'$ -band is used for WL analysis, and all the band are used for photometric redshift (photo- $z$ ). The bands for photo- $z$  is determined by simulations based on Nishizawa et al. [70]. In these simulations the mock catalog is made by imposing the conditions that the catalog satisfy the redshift-magnitude relation in COSMOS photo- $z$  catalog [34]. Note that the COSMOS photo- $z$  catalog provides reliable redshift estimates since 30 bands data and spectroscopic subsample were used. The exposure time and number of exposures of each band is summarized in Table 5.1. We chose the number of exposures in order to to minimize the number of saturated stars. The nighttime condition was clear enough for WL measurement.

filter	exposure time [s]	number of exposures	total exposure time [s]
$B$	200	3	600
$r'$	200	3	600
$i'$	240	10	2400
$z'$	270	12	3240
$Y$	270	12	3240

Table 5.1: Summary of exposure time of each band.

## 5.2 Analysis Overview

Figure 5.1 shows an overview of the data analysis. In this analysis, a HSC pipeline, the software suite being developed for HSC data analysis, was used. The HSC employs 112 science CCDs, which produces  $\sim 10000$ -chip data whose size is  $\sim 200$ GB per a night. Thus it is difficult to check if all the chips are successfully reduced at each stage. This pipeline attempts to reduce chips in an automated way from raw data to catalog. In addition, to make the reduction faster, this pipeline passes the intermediate products via memory rather than using the hard drive. The core part of the pipeline is written in C++, which is wrapped by Python. This feature enables developers and users to combine pipeline modules in script language. The HSC pipeline is used for chip-based data reduction, image stacking, and PSF matching. Our WL measurement software described in Section 4 is also integrated into the pipeline.

The flow-chart of our analysis is as follows. First, raw data of each chip enters the chip-based data reduction stage as shown in Fig.5.1. Instrumental signature removal (ISR) includes overscan correction, flat fielding, sky subtraction, and so on, which will be mentioned later. Then PSF is determined by using Principal Component Analysis (PCA) [39]. Next, the chip images are stacked to boost signal-to-noise ratio (S/N) of each object. At this stage, mosaicing of chips is solved, and world coordinate system (WCS) for each chip is produced. Following the WCS, chips are stacked. Details of these two processes will be described in Section 5.3. For obtaining good photometry, PSF is matched between different band images. Object detection is then done on the stacked image. We use the stacked image in order to detect fainter objects. Photometry is carried out based on the object catalog. Details of these processes will be described in Section 5.4.1.

At this point, we are prepared to measure quantities needed for cluster mass estimate, redshifts and shapes. Using the photometry catalog, photo- $z$  is carried out to obtain redshift catalog. Details of photo- $z$  will be described in Section 5.4.2.

Shape measurement is carried out using multiple exposures rather than a stacked image. Traditionally shape is measured using a stacked image. However, there are some issues on the stacked image analysis.

- Stacking needs image warping. This requires pixel resampling.
- PSF of each exposure is mixed.

The first point means that original information of each pixel is destructed. At this manipulation, pixel interpolation is carried out to resample pixel values. For example, bilinear interpolation<sup>1</sup> is often used, but this interpolation causes correlated noise, which should be originally zero unless cross-talk exists. Lanczos interpolation

---

<sup>1</sup>Bilinear interpolation interpolates given pixel values to an arbitrary target position with weight

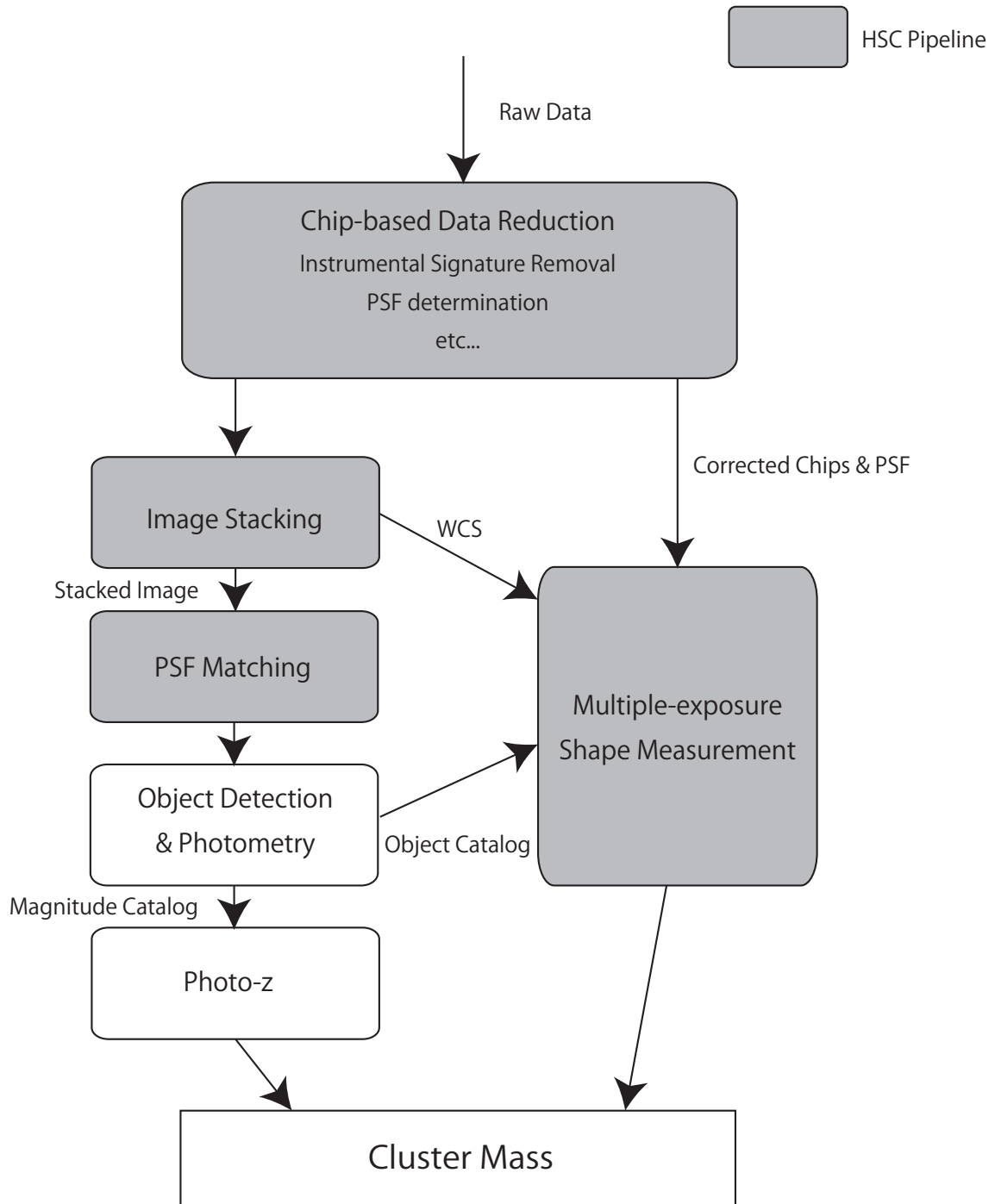


Figure 5.1: Analysis Overview.

might be a better solution for interpolation, which attempts not to introduce any artificial information. This is because in Fourier space the Lanczos filter has zero value at wavelengths shorter than twice of pixel scale<sup>2</sup>. Although it is worth testing whether Lanczos filter provides accuracy enough for shape measurement, we do not pursue this in this thesis. There are other reasons enough to use multiple exposures, as described below.

The second point is that stacking process mixes PSF although it originates from different physical situation. For instance, PSF pattern changes due to optics misalignment which depends telescope elevation and other factors of telescope mechanics, and atmospheric aberration which depends on temperature, humidity, and wind speed/direction. By mixing these effect, PSF on stacked image becomes complicated, and therefore it may become difficult to be modelled. Since accurate correction of PSF is important for shape measurement, this may cause systematic bias.

To make use of information of PSF from each chip, we adopt multiple-exposure shape measurement. For this, we use corrected chip images and PSF information from the chip-based data reduction stage, WCS from the image stacking stage, and object catalog from the object detection & photometry stage. WCS is used to transform the position of object from pixel coordinates on the stacked image to that on each chip. Details of formulation for multiple-exposure analysis will be given in Section 5.5.1

Another advantage of multiple-exposure shape measurement is that it is able to

---

based on the distance between the target position and surrounding pixels. Interpolation is first carried out along one direction, and then that for other direction is made.

<sup>2</sup>Suppose an interpolation for discrete data is written as convolution

$$I(x) = (W * I)(x) = \sum_{y=-\infty}^{\infty} W(x-y)I(y)dy, \quad (5.1)$$

where  $W(x)$  is convolution kernel, or filter. In Fourier space, the ideal interpolation is written as

$$\tilde{W}(f) = \begin{cases} 1 & \text{for } -\pi f_n < f < \pi f_n \\ 0 & \text{otherwise,} \end{cases} \quad (5.2)$$

where  $f_n$  is Nyquist frequency. This filter cuts off all signal components greater than  $f_n$ , which is beyond information provided by the discrete data, while keeping lower-frequency components unchanged. This becomes a sinc function  $\sin(\pi x)/\pi x$  in real space. However, in practice it is extremely difficult to use sinc function since it has wide wing. Lanczos filter add weight and truncates the sinc function as

$$W(x) = \begin{cases} \text{sinc}(x)\text{sinc}(x/a) & \text{for } -a < x < a \\ 0 & \text{otherwise,} \end{cases} \quad (5.3)$$

where  $a$  is typically set to 2 or 3. This filter still cuts off all Fourier components greater than Nyquist frequency.

test the quality of each exposure. This allows us to check if each exposure is adequate for shape measurement by looking at shape-related quantity directly. Details of this test will be described in Section 5.5.4.

Then photo- $z$  catalog and shear catalog will be used for cluster mass estimate, which will be described in Section 5.6, together with lensing and photo- $z$  systematic effects on the mass.

## 5.3 Data Reduction

### 5.3.1 Data Format of HSC Pipeline

The HSC pipeline produces three planes for a single chip. The first is an image plane, which contains image data itself. The second is a variance plane, which stores variance of each pixel. They are calculated from the raw image assuming Poisson noise of photons coming into a pixel which is propagated at each stage of the reduction. The third is a mask plane, which has the 16-bit integer on each pixel. Different bits are used for different masks such as saturated, bad, and so on. Thus if one encounters a pixel having nuisance masks, this pixel can be removed from the analysis.

### 5.3.2 Chip-based Data Reduction

In the chip-based data reduction, instrumental signature, such as vignetting and sky background, is removed to make an image prepared for measurements. Then the reduction moves to calibration stage where PSF and WCS determination are carried out. This WCS is used as an initial guess for mosaicing in image stacking. Final stage of the reduction is photometry stage where flux and moment measurements are performed. The measured flux is also used by image stacking to determine scale between different chips.

#### Instrumental Signature Removal Stage

First, pixels having a value greater than a saturation threshold are masked as SAT. Different saturation thresholds are set to different CCDs.

A raw chip image consists of image data regions and overscan regions. CCD has 4 outputs (or amps), each of which reads out  $4177 \text{ pixels} \times 512 \text{ pixels}$ . Thus raw data has 4 stripes of image data. Between the stripes there are the overscan regions, the part that is not exposed to light. The overscan regions record bias voltage that is intentionally added by electronics during readout process for keeping CCD signals inside of a dynamic range of the electronics. Using median of the overscan regions,

the bias is subtracted. Then the overscan regions are trimmed and 4 image data regions are assembled.

Now that we have signals only from photons, a variance plane, which was described in Section 5.3.1, is created. Assuming Poisson statistics, the variance at pixel  $(x, y)$  is calculated as  $\text{Var}(x, y) = I(x, y)/g$ , where  $I(x, y)$  is pixel count and  $g$  is gain, or conversion factor, of CCD defined as how many electrons are converted to a single count of a pixel.

Next, flat fielding is carried out, which corrects ununiformity over the field of view. The ununiformity is caused by vignetting towards the edge of the field, ununiform transmittance of a filter, QE variation of pixels, and so on. By illuminating all pixels with same brightness, we can obtain reference images called flat. In this thesis, we use dome flat, which is created by using uniform light source inside of the dome. The dome flat was taken on the same day as our observations. Dividing image data by the flat, we obtain a flat-fielded image.

Interference of photons coming into CCD might cause fringe pattern, which appears especially in longer wavelength. Fringe subtraction on  $Y$ -band is carried out by using a fringe frame, which is created from sky frames. Scaling of the fringe frame is calculated iteratively, and then subtract the scaled fringe frame from the chip image.

Next, known CCD defects are masked as **BAD**, and saturation mask (**SAT**) is grown by 2 pixels to mask out pixels having photons leaking out from saturated pixels. If there are pixels having NaN, they are masked as **UNMASKEDNaN**.

As a final step of ISR, sky subtraction is performed. First, the chip image is divided into  $1024 \text{ pixel} \times 1024 \text{ pixel}$  patches and background in each patch is calculated as  $3\text{-}\sigma$  clipped mean. Then the background is interpolated by spline interpolation, which is subtracted from the chip image.

## Calibration Stage

First, PSF is determined. To prepare for PSF determination, defects are fixed by interpolating pixels values surrounding the defects. The interpolated pixels are masked as **INTRP**. As an initial guess for PSF, a Gaussian with FWHM=1.0 arcsec is used. A set of pixels sharper than the PSF is regarded as a cosmic ray, and masked as **CR**.

In order to find stars to be used for PSF determination, detection of bright objects are carried out with the initial PSF. The chip image is convolved with the PSF. Then on the convolved image, a set of connected pixels above  $n\sigma$ , where  $\sigma$  is background noise and  $n$  is a (relative) detection threshold, are found and assembled into a footprint. These pixels are masked as **DETECTED**. A single footprint is regarded as an object. In this process the PSF plays a role of a matched filter, which is the optimal filter for finding objects having same profile as the filter given that noise

consists of only white noise. At this point, a lot of faint objects are included. In order to select bright objects, footprints having a peak that is greater than  $n_{\text{extra}}n\sigma$  are selected as bright objects, where  $n_{\text{extra}}$  is called an extra threshold. Then sky subtraction is performed again with the detected objects masked. We used finer mesh ( $128 \times 128$ ) to remove small variation of sky. To mask outskirts of bright objects, we set the detection threshold to 2. When the threshold is greater than this value, sky is over-subtracted since the outskirts of the bright objects are regarded as sky background. The extra threshold is set to 5. Then measurements of the bright objects are carried out. Although various quantities based on different measurement algorithms are measured, we explain three quantities that are related to our analysis. The first is aperture flux, which sums up pixel value inside of  $3.6''$  aperture. Second is PSF flux which is measured by minimizing  $\chi^2$  based on PSF model. This flux is optimal in terms of signal-to-noise ratio. The last is adaptive second order moments. Since data has noise in general, it is necessary to set weight function to calculate second order moments:

$$I_{xx} = \int W(\mathbf{x})I(\mathbf{x})x^2d\mathbf{x}, \quad (5.4)$$

$$I_{xy} = \int W(\mathbf{x})I(\mathbf{x})xyd\mathbf{x}, \quad (5.5)$$

$$I_{yy} = \int W(\mathbf{x})I(\mathbf{x})y^2d\mathbf{x}. \quad (5.6)$$

Although a Gaussian is commonly used for the weight function, adaptive moments employ an elliptical Gaussian weight whose shape is matched to the object, which gives more optimal estimates.

Based on these measurements, star-galaxy separation is carried out. As a first step, objects whose PSF flux is lower than the parameter `fluxLim` is removed to get rid of faint galaxies. Next, stars are selected by using the adoptive second order moments by looking at two dimensional histogram of  $I_{xx}$  and  $I_{yy}$ . Since stars have similar moments, objects around the peak of the histogram are likely stars. Thus objects within  $2\sigma$  from the peak are selected, and flagged as **STAR**<sup>3</sup>.

Finally, using these stars, PSF is determined as follows.

- Principal components, which is described below, of PSF are constructed from star images.

---

<sup>3</sup>If this selection is only within  $1\sigma$ , it tends to reject stars around edge of a chip whose ellipticity is not small due to optical distortion and aberration. However, when the selection becomes more tolerant, the possibility to pick up galaxies increases. This is because ellipticity of small galaxies around the center of exposure may be comparable with that of stars around the edge. This contamination might be reduced by using the second order moments measured on the coordinates where optics distortion is corrected.

- Interpolate the principal components to model its spatial variation.

The PSF determination in the HSC pipeline employs PCA. PCA is a mathematical procedure which converts a set of data of possibly correlated variables into a set of values of uncorrelated variables called principal components by using orthogonal transformation<sup>4</sup>. The number of principal components is less than or equal to the number of original variables. The transformation is defined in a way that the first order principal component has as high a variance as possible, which means that it accounts for as much of the variability in the data as possible. Each succeeding component has the highest variance under the condition that it is orthogonal to the preceding components. Using linear combination of the principal components, we can reconstruct the data.

The number of principal components, which is specified by the parameter `nEigenComponents` in the HSC pipeline, is arbitrary<sup>5</sup>. If `nEigenComponents` is same as the number of the original variables, the data will be fully reconstructed by the linear combination. However, it will contain a feature we do not want such as noise. Thus `nEigenComponents` should not be so large, but should not be so small; this will not capture the variations of PSF. PCA itself does not tell how many principal components we should use, so that we have to choose `nEigenComponents` empirically.

The HSC pipeline constructs the principal components as two dimensional image postage, as shown in Fig. 5.2. Next, PSF including spatial variation is modelled as

$$P(u, v; x, y) = K_0(u, v) + \sum_{i=1}^{n-1} a_i F_i(x, y) K_i(u, v), \quad (5.7)$$

where  $(u, v)$  is the coordinates inside of the two dimensional image postage representing a principal component,  $(x, y)$  is the coordinates across the chip which corresponds to the center of PSF,  $F_i(x, y)$  is a spatial model of PSF, and  $K_i$  is *normalized* principal components which are introduced to conserve the amplitude of PSF. They are defined as

$$K_0 \equiv k_0(u, v) / \sum_{u, v} k_0(u, v), \quad (5.8)$$

$$K_i \equiv k_i(u, v) / \sum_{u, v} k_i(u, v) - K_0, \quad (5.9)$$

where  $k_i$  is  $i$ -th the principal components. Thus sum of PSF over  $(u, v)$  is always unity. This normalization technique comes from Alard and Lupton [5]. The HSC

---

<sup>4</sup>Depending on the field of application, PCA is also named the Karhunen-Loeve (KL) expansion and principal components are named KL components.

<sup>5</sup>Although it is not common to count average of data as the number of principal components, we include it in this thesis as 0th order component.

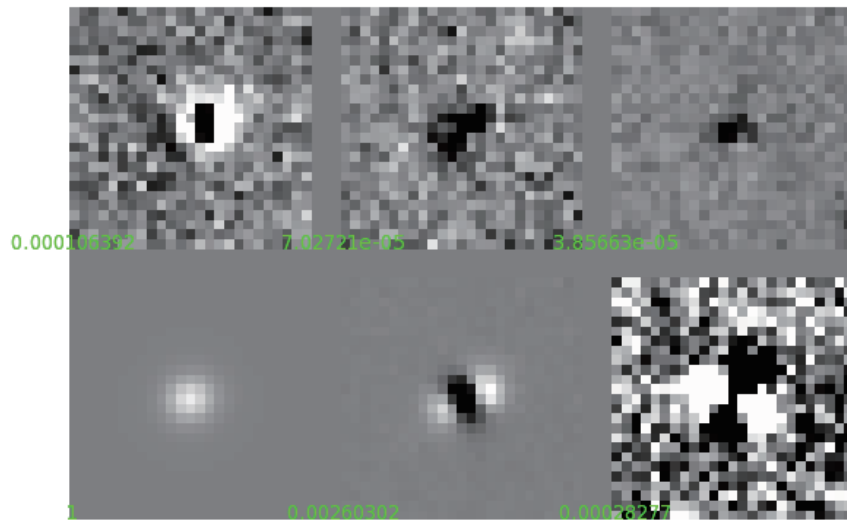


Figure 5.2: Example of principal component analysis of PSF. The lower left image is 0th order of principal components which corresponds to mean of data. The order of principal component increases, as an image goes from the lower center to lower right and then from the upper left to upper right.

pipeline adopts Chebyshev polynomials defined as

$$T_0(x) = 1, \tag{5.10}$$

$$T_1(x) = x, \tag{5.11}$$

$$T_{n+1}(x) = 2xT_n(x) - T_{n-1}(x) \tag{5.12}$$

in one dimension, where  $x$  is restricted to  $-1 < x < 1$ . In fact, since the coordinates of chip is two-dimensional,

$$T_{pq}^{(2)}(x, y) = T_p(x)T_q(y) \tag{5.13}$$

is employed, and coordinates  $x, y$  is scaled as it takes -1 and/or 1 at edges of chip. Chebyshev polynomial is chosen to prevent polynomials from diverging around the edge of chip; while simple polynomials diverges at the edge, Chebyshev polynomials converges to -1 or 1. The coefficients in Eq. (5.7) is obtained by fitting stellar images. The process to determine the principal components and the spatial variation is iterated for three times. At each iteration, the star candidates having larger  $\chi^2$  value are rejected. Objects used for PSF at the final iteration are flagged as **PSFSTAR**. The PSF determination strongly depends on order of polynomials for spatial fit, the parameter `spatialOrder`, as well as the number of principal components `nEigenComponents` and the flux limit for bright source selection `fluxLim`. We will describe how we determine the parameters in Section 5.5.2. Using the PSF, all measurements such as flux and moments described above are carried out again on the bright objects.

Next, astrometry is performed to determine the position of objects in the sky, which will be used for the initial guess of mosaicing in the image stacking process. First, the bright stars are matched to a reference catalog created from SDSS DR8[4], by using `astrometry.net`<sup>6</sup>, the *astrometry engine* to create astrometric meta data for a given image. Then based on the match list, WCS is determined in TAN-SIP convention where the coordinate transformation from pixel coordinates to celestial coordinates is represented by simple polynomials with `order= 2`.

Comparing the measured aperture flux with magnitude in the reference catalog, magnitude zero point is determined. As a default setting, a reference catalog based on SDSS DR8[4] is prepared. However, we have to determine magnitude zero point of Y-band which does not exist in SDSS filter system. To solve this issue, the new reference catalog, so-called native band catalog, is created. First, objects around the field of ACTJ0022 were retrieved from the SDSS reference catalog. Then, using a stellar atmosphere model provided by Castelli and Kurucz [22], the SDSS magnitudes are extrapolated to Y-band as follows. Castelli and Kurucz Atlas provides 3808 stellar spectra with various parameters of metallicities, effective temperatures

---

<sup>6</sup><http://astrometry.net/>

and gravities. For each stellar object in the retrieved catalog, fitting to all the stellar spectra is performed and the stellar model which gives the smallest  $\chi^2$  value is selected. Then convolving  $Y$ -band filter response to the spectra,  $Y$ -band magnitudes for each stellar objects are obtained. Note that for the filter response, mirror reflectivity, atmospheric extinction, and camera transmittance are included. Also magnitudes for  $Br'i'z'$  are provided as well. We use these native band reference magnitudes in this thesis. Since the reference construction begins from SDSS magnitudes that are already calibrated to atmospheric extinction at a reference airmass of 1.3, we do not have to correct for the airmass. On the other hand, since the SDSS magnitudes are not corrected for Galactic extinction, we have to correct for it, which is described in Section 5.4.1.

Figure 5.3 shows an example of output image from calibration stage. Green bleeding masks show SAT and INTRP, blue masks show DETECTED, and magenta masks show CR. Yellow circles with yellow texts show stars that are used for PSF determination, and yellow circles with red texts show an object which is selected as star candidate by star/galaxy separation but later rejected in the process of PSF determination due to large  $\chi^2$  value. Texts under the circles show object ID and the  $\chi^2$  value.

## Photometry Stage

Finally, the pipeline measures various quantities of faint objects, which is called photometry stage. First, faint object detection is performed with the extra threshold used in the bright object detection turned off. For the detected faint objects, same measurements described in the previous section, such as fluxes and moments, are carried out. The results of this measurements are used in the next image stacking.

### 5.3.3 Image Stacking

Image stacking is carried out as follows. First, it collects the reduced chip images, catalogs, and match list of objects on our images and reference catalog. To make mosaic, the image stacking algorithm uses not only position of stars in the reference catalog, but also that of slightly fainter objects lying on different exposures. Using the latter information, precision of the mosaic is improved by a factor of 2. This mosaicing is recorded as TAN-SIP WCS whose order = 10, which will be used by multiple-exposure shape measurement. In addition, using photometry catalog of each chip, scaling between different chips are determined. Typically the scaling is within  $\pm 2\%$ . After the mosaicing and scaling are determined, each chip image is warped and rescaled. Warping requires resampling of pixels values. Among several resampling algorithm available in the pipeline, we chose Lanczos3 algorithm, the Lanczos filter truncated at  $a = 3$  in Eq. (5.3). Thanks to the high precision mo-

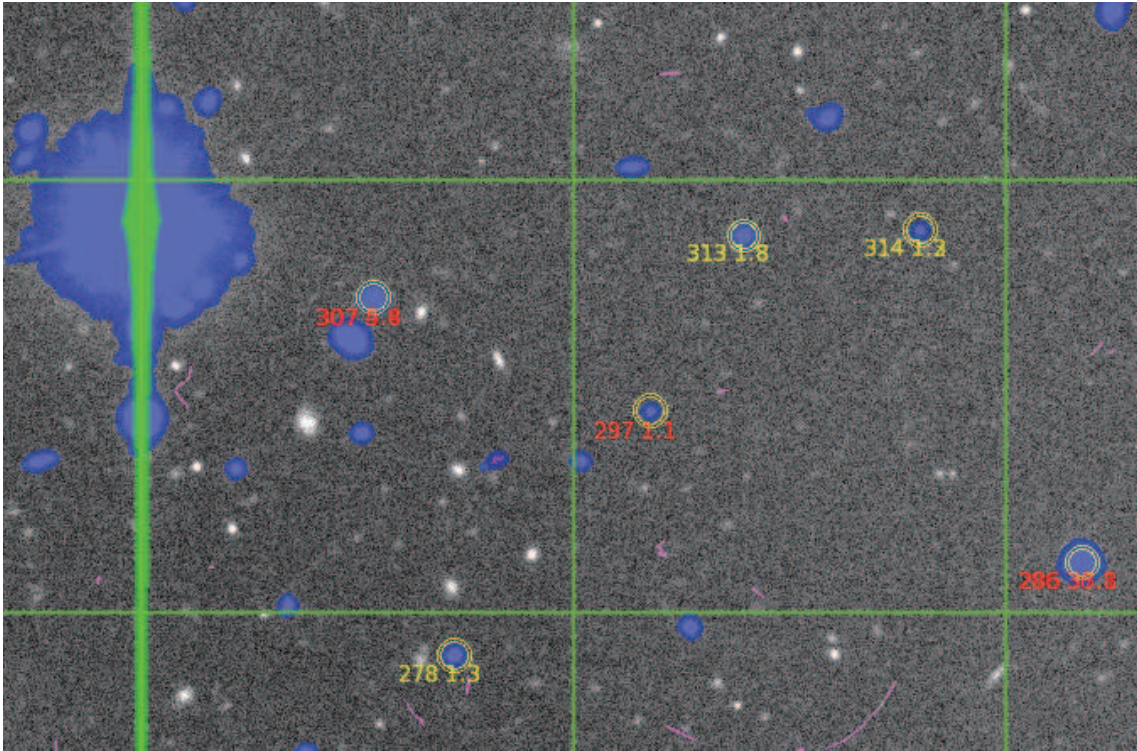


Figure 5.3: One example of reduced image. This image is  $\sim 700$  pixel  $\times$   $\sim 450$  pixel of the center part of chip ID = 126932. For details about colors and numbers, see text.

saicing, astrometry accuracy of stacked image achieved  $\sim 0.03''$ . The RGB images consisting of  $r'i'z'$  stacked images are shown in Fig. 5.4.  $\sim 8 \times \sim 8$  arcmin<sup>2</sup> region around the center is trimmed.

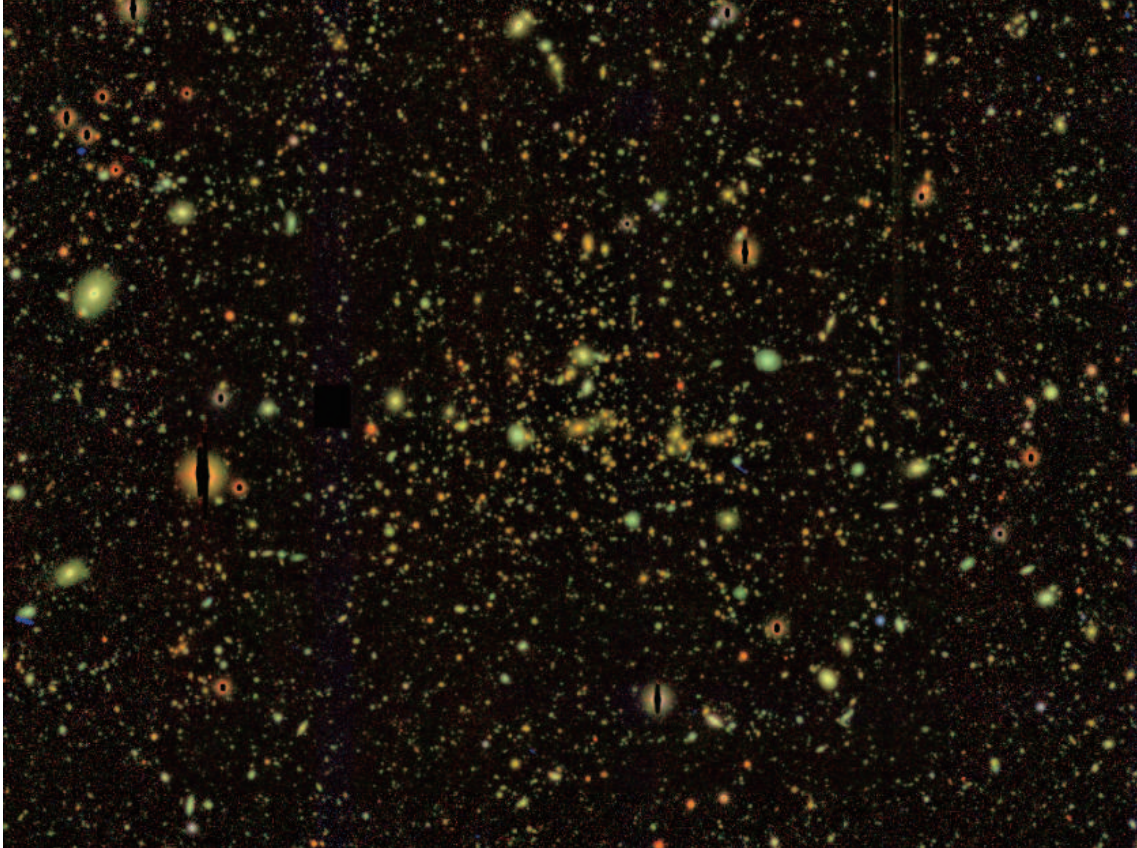


Figure 5.4: RGB image of ACTJ0022 which consists of  $r'i'z'$  stacked images processed by the HSC pipeline.  $\sim 8 \times \sim 8$  arcmin<sup>2</sup> region around the center is trimmed.

## 5.4 Photometry and Redshift Estimation

In this section, we describe how to estimate redshift of each galaxy by using photo- $z$ . To obtain photo- $z$  we need to measure colors, the difference of magnitudes between two bands. We first explain how to measure accurate colors, and then move to photo- $z$  estimation.

## 5.4.1 Photometry

### PSF Matching

Photo- $z$  requires *good* color estimates. Colors should be derived from fluxes within identical physical aperture on an object in different bands. Since PSF changes apparent size of objects, we should match PSF of different bands to the largest PSF.

First, to find the largest PSF, we measured PSF of each stacked image using PSF determination algorithm of the HSC pipeline. Then we measured size of PSF model reconstructed at several positions of stacked images by using adaptive moments

$$\sigma = (I_{xx}I_{yy} - I_{xy}^2)^{1/4}. \quad (5.14)$$

We found the size of largest PSF is  $\sim 2.6$  pixel, which is around the edge of  $r'$ -band stacked image. This large PSF originates from one of the three  $r'$  exposures.

Next, to match the PSF, we used a method developed by Alard and Lupton [5] which is already implemented in the HSC pipeline. This method enables to match the PSF to an arbitrary, analytical target PSF. We set the target PSF to Gaussian with  $\sigma = 2.6$  pixel. The method uses Gaussian-based orthogonal functions to construct matching kernel. The orthogonal function is similar to GL functions used in the EGL method; Alard and Lupton [5] adopted products of Gaussian and polynomials for higher order. Also the kernel varies with spatial position, which allows for a uniform target PSF across the field.

Table 5.2 shows size and ellipticity before and after PSF is matched, where the ellipticity is calculated again by using adoptive moments of stars;

$$e_1 = \frac{I_{xx} - I_{yy}}{I_{xx} + I_{yy}}, \quad (5.15)$$

$$e_2 = \frac{2I_{xy}}{I_{xx} + I_{yy}}. \quad (5.16)$$

The PSF size of different bands is matched to 2.6 pixel within  $\sim 1\%$ . Similarly ellipticity and its standard deviation is much reduced.

### Object Detection and Photometry

Object detection and photometry are performed by using dual mode of SExtractor[11], which uses a reference image for object detection and measures photometry on another image. We carried out five measurements. For all the measurements, non-PSF-matched  $i'$ -band image is used as a reference image to detect objects and define which pixel belongs to an object (so-called segmentation). For photometry, we use PSF-matched  $Br'i'z'Y$ -band images. We used `MAG_ISO` for photometry to be used

	filter	$\sigma$ [pixel]	$e_1$	$e_2$
$B$	original	$1.394 \pm 0.04$	$0.055 \pm 0.023$	$-0.002 \pm 0.013$
	PSF match	$2.609 \pm 0.02$	$-0.003 \pm 0.005$	$-0.001 \pm 0.004$
$r'$	original	$2.279 \pm 0.11$	$-0.032 \pm 0.018$	$-0.009 \pm 0.019$
	PSF match	$2.572 \pm 0.06$	$-0.001 \pm 0.011$	$-0.002 \pm 0.012$
$i'$	original	$1.553 \pm 0.05$	$-0.019 \pm 0.025$	$-0.006 \pm 0.035$
	PSF match	$2.609 \pm 0.03$	$0.001 \pm 0.008$	$-0.002 \pm 0.012$
$z'$	original	$1.914 \pm 0.06$	$-0.015 \pm 0.020$	$-0.022 \pm 0.026$
	PSF match	$2.603 \pm 0.04$	$0.001 \pm 0.009$	$-0.003 \pm 0.013$
$Y$	original	$1.645 \pm 0.08$	$0.000 \pm 0.025$	$-0.023 \pm 0.035$
	PSF match	$2.604 \pm 0.04$	$0.001 \pm 0.008$	$-0.002 \pm 0.012$

Table 5.2: Size and ellipticity before and after PSF is matched.

for color, which measures the flux within the segmentation defined on the reference image. Defining the segmentation on the non-PSF-matched image is the best solution, since if we define it on a PSF-matched image it will pick up pixels at outskirts of objects and resultant photometry becomes noisy. In addition, the segmentation defined on a PSF-matched image may pick up pixels in blended parts of neighboring objects.

Magnitude zero point is determined by using the HSC pipeline. It measures stellar flux in  $4.8''$  aperture on the PSF-matched images. We used such a large aperture in order to cover all the flux from stars smeared by PSF matching. Then the flux is compared to the native catalog described in Section 5.3.2 to determine the magnitude zero point. The errors of the zero point are  $B$ : 0.048,  $r'$ : 0.090,  $i'$ : 0.043,  $z'$ : 0.080, and  $Y$ : 0.086.

## Dust Extinction

We estimated dust extinction, following the approach shown in Schlegel et al. [87]. Dust extinction affects observed magnitude of a pass band  $b$  as

$$m_{\text{obs}} = m_{\text{true}} + \Delta m_b, \quad (5.17)$$

where  $m_{\text{obs}}$  is observed magnitude of an object,  $m_{\text{true}}$  is true magnitude where dust extinction is corrected, and  $\Delta m_b$  is dust extinction of a pass band  $b$ .  $\Delta m_b$  is calculated as

$$\Delta m_b = -2.5 \log_{10} \left( \frac{\int d\lambda W_b(\lambda) S(\lambda) 10^{-A(\lambda)/2.5}}{\int d\lambda W_b(\lambda) S(\lambda)} \right), \quad (5.18)$$

where  $W_b(\lambda)$  is a weight originating from telescopes and instruments at a range of pass band  $b$ ,  $S(\lambda)$  is the photon luminosity of the object, and  $A(\lambda)$  is the dust

extinction at wavelength  $\lambda$ . We calculated  $W_b(\lambda)$  as

$$W_b(\lambda) = B(\lambda)R(\lambda)P(\lambda)F_b(\lambda)Q(\lambda), \quad (5.19)$$

where  $B(\lambda)$  is the atmospheric transmittance at the summit of Mauna Kea given by Fig. 3.6,  $R(\lambda)$  is the reflectivity of primary mirror of the Subaru Telescope given by Fig. 3.2,  $P(\lambda)$  is the transmittance of prime focus unit of the Suprime-Cam given by Fig. 3.9,  $F_b(\lambda)$  is the transmittance of a filter  $b$  given by Fig. 3.10, and  $Q(\lambda)$  is the QE of the CCD given by Fig. 3.12.  $S(\lambda)$  is obtained by averaging the normal elliptical galaxy spectral energy distributions (SEDs) from Kennicutt [43]. We extrapolated the averaged SED as  $S(\lambda) \propto \lambda$  outside the range of the spectral coverage.  $A(\lambda)$  are calculated from functional forms which give the ratio between extinction at a certain wavelength  $\lambda$  and extinction of  $V$ -band as a function of wave number  $x$  which corresponds to the inverse of wavelength  $\lambda$ , which is expressed as

$$\frac{A(\lambda)}{A(V)} = a(x) + \frac{b(x)}{R_V}. \quad (5.20)$$

For  $a(x)$  and  $b(x)$ , we employed O'Donnell [72] in the optical wavelength and Cardelli et al. [19] in the ultraviolet and infrared wavelength.  $R_V$  is defined as the  $V$ -band extinction  $A(V)$  and the relative extinction between  $B$ - and  $V$ - band called reddening:

$$R_V = \frac{A(V)}{A(V) - A(B)} \equiv \frac{A(V)}{E(B - V)}. \quad (5.21)$$

Although the value of  $R_V$  varies, the observational evidence favors  $R_V \sim 3.1$  which we actually used for the estimation of dust extinction. According to the dust extinction map provided by NASA/IPAC Infrared Science Archive<sup>7</sup> which derived reddening by using the data Schlegel et al. [87] pioneered combining the strengths of IRAS and COBE/DIRBE, the reddening around the field of ACTJ0022 ranges from 0.0242 mag to 0.0260 mag with mean value of 0.0250 mag. Since the variation is subtle, we adopt  $E(B - V) = 0.0250$  mag which yields  $A(V) = 0.0074$  mag with the assumption of  $R_V \sim 3.1$ . The calculations mentioned above give the dust extinction of each band as shown in Table 5.3.

## 5.4.2 Photometric Redshift

Although spectroscopy gives a good redshift estimate, it is not practically feasible to obtain spectroscopic redshift (spec- $z$ ) of all the galaxies appear on our image. It requires a several ten minutes for measuring spectrum of one object, and it is not easy to perform robust spectroscopy of faint galaxies which we actually want to use for shear estimate.

<sup>7</sup><http://irsa.ipac.caltech.edu/applications/DUST/>

filter	$\Delta m_b$ (mag)
<i>B</i>	0.098
<i>r'</i>	0.066
<i>i'</i>	0.050
<i>z'</i>	0.036
<i>Y</i>	0.031

Table 5.3: Estimated dust extinction around the field of ACTJ0022-0036.

Instead, we use a technique to estimate redshifts by combining multi-passband magnitudes of a given galaxy image, which is so-called photo- $z$ . The photo- $z$  has better cost efficiency than spectroscopy since, in our case, it gives redshift estimates of several ten thousand galaxies by using only five passband images.

In this thesis, we use the public available code, *La Phare*<sup>8</sup> [8][34], which uses template SED. The photo- $z$  of a galaxy is estimated by minimizing  $\chi^2$ ;

$$\chi^2(\alpha, T, z, E) = \sum_i^{N_f} \frac{[f_i^{\text{obs}} - \alpha f(T, z, E)]^2}{\sigma_i^2}, \quad (5.22)$$

where  $f_i^{\text{obs}}$  is observed flux of  $i$ -th filter,  $f(T, z, E)$  is the model flux which is a function of SED type  $T$ , redshift  $z$ , and the amount of extinction by the galaxy itself  $E$ . The summation runs over the number of filters we use. The factor parameter  $\alpha$ , which is the same in all the bands, is introduced because the photo- $z$  is estimated only from colors.

The primary feature of galaxy spectra is 4000Å break, the strong absorption at wavelength bluer than 4000Å in rest frame which originates from stellar spectra having an accumulation of absorption lines of mainly ionized metals. If 4000Å break is captured by given passbands used for photo- $z$ , the redshift is estimated well. On the other hand, if the spectral feature is misidentified, the redshift is drastically misestimated, which is called catastrophic error. If redshifts are estimated higher than true redshift, they may contaminate background galaxies used for shear estimate, which will dilute shear estimate.

The template sets of SED we use are same as what is called CWW in Ilbert et al. [33]. This is based on observed spectra by Coleman et al. [24], which is further optimized by Ilbert et al. [33].

*La Phare* has a functionality to re-calibrate magnitude zero points. There exists uncertainty on magnitude zeropoint determined by photometry. Also the template SEDs we use do not perfectly represent spectrum of galaxies. To reduce these

<sup>8</sup><http://www.cfht.hawaii.edu/~arnouts/LEPHARE/lephare.html>

uncertainties, objects whose spec- $z$  is already known are used, and the magnitude zero points are shifted to minimize the difference between photo- $z$  and spec- $z$ . Note that it is not calibration of photometry, but optimization for photo- $z$ . We used SDSS DR8[4] and BOSS[27] spectra for spec- $z$ . The number of matched objects, including stars and QSOs, to our catalog is 225. However, some of them saturate since our images are deeper, so that finally we used 205 objects for the re-calibration. The obtained shifts of magnitude zeropoints are  $B$ :0.072,  $r'$ :-0.057,  $i'$ :-0.023,  $z'$ : -0.053, and  $Y$ :0.016.

The scatter plot between photo- $z$  and spec- $z$  is shown in Fig. 5.5. Blue and green dots denote the scatter before and after magnitude zeropoint re-calibration, respectively. The solid line denotes the case that photo- $z$  and spec- $z$  are perfectly consistent, i.e.,  $z_p = z_s$ . When photo- $z$  is out of dashed lines,  $z_p > 1.05z_s + 0.2$  or  $z_p < 0.95z_s - 0.2$ , we regard the estimates are outlier. Outlier fraction, mean bias, and scatter before and after the re-calibration are summarized in Table 5.4. The latter two quantities are calculated after the outliers are removed. Although outlier fraction is not improved very well, meas bias and scatter become a half of the original magnitude zero points. This implies that the re-calibration does not help to reduce catastrophic error, but once we are able to find a proper SED, it yields better photo- $z$  estimate. The outlier fraction is large, but this is probably due to lack of bluer bands. Actually, our bluest band,  $B$ , overlaps 4000Å break if a galaxy is at redshift of  $z \sim 0$ , which does not give enough information to estimate photo- $z$ . If calibration samples with higher  $z_s$  were available, the outlier fraction would be smaller and give more robust re-calibration.

	original	calibrated
outlier fraction	0.722	0.654
mean bias*	-0.066	-0.032
scatter*	0.740	0.366

\* These quantities calculated after outliers are rejected.

Table 5.4: Photo- $z$  statistics before and after re-calibration of magnitude zeropoint.

Figure 5.6 shows the result of photo- $z$  estimated for objects whose flux in  $3''$  aperture is 5 times larger than its error are selected. A peak at  $z_p = 1.65$  is suppressed when we apply a selection for shape measurements which is mentioned in Section 5.6.2. Since we can use galaxies with higher signal-to-noise ratio for shape measurements, the peak is due to galaxies with lower signal-to-noise ratio. To check the result of photo- $z$ , we look at  $z_p$  of the cluster. First, we select galaxies around 2000 pixel  $\times$  2000 pixel at the center of image, since typical cluster size,  $\sim 2$  Mpc, at  $z \sim 0.8$  corresponds to  $\sim 1300$  pixel of our image. Then we make color-magnitude diagram, using  $r' - z'$  and  $z'$ , to select the cluster from a sequence member galaxies

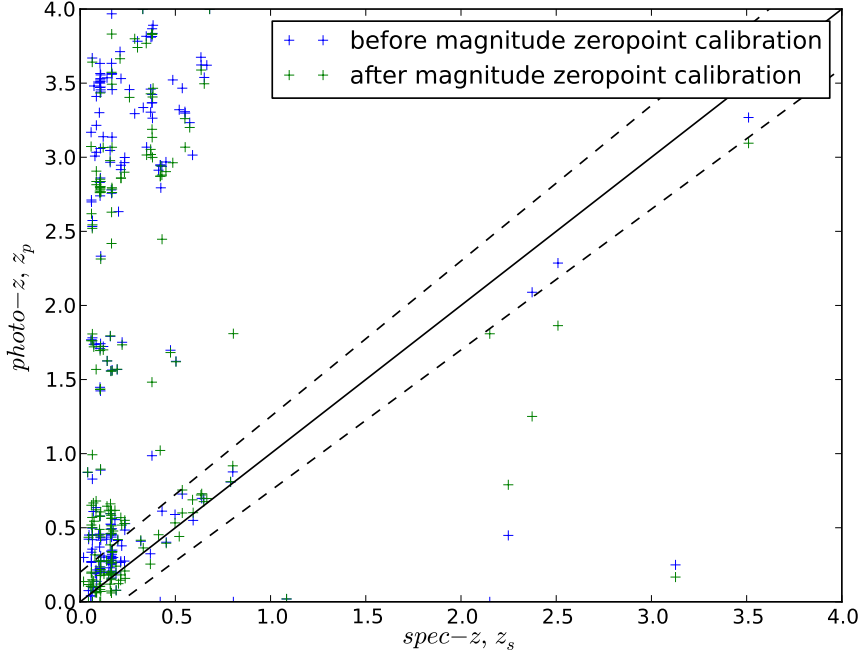


Figure 5.5: The scatter plot between photometric and true redshift. Blue and green dots denote the scatter before and after magnitude zero-point calibration, respectively.

of a cluster makes, so-called red sequence. This sequence is caused by the fact that member galaxies of a cluster were born in same era, so that a cluster mostly consists of early-type galaxies (elliptical and S0 galaxies) whose color is red. The member galaxies of a cluster at redshift of  $z \sim 0.8$  are expected to have a sequence around  $r' - z' \sim 2$ . We regarded the region enclosed in red lines in Fig. 5.7,  $19 < z' < 23$ ,  $r' - z' > -0.12z' + 4.25$ , and  $r' - z' < -0.12z' + 4.75$ , as the red sequence of ACTJ0022, and selected the sample as a part of the cluster. Figure 5.8 shows the histogram of  $z_p$  of the sample. The peak is at a bin of  $z_p = 0.775 \pm 0.025$ , which is shifted to lower redshift by  $z_p \sim 0.03$  compared to known redshift of the BCG of ACTJ0022. There are some drastical misestimations above  $z_p \gtrsim 2$ , which will contaminate background galaxies as described before. Thus they should be removed when we estimate shear signals. The outlier fraction is reduced to 0.256, which implies that photo- $z$  is determined better than lower redshift because we have enough bandpasses covering range of SED to tell 4000Å break in this redshift range. From this histogram, we decided background galaxy selection as  $0.95 < z_p < 2.0$ . Note that

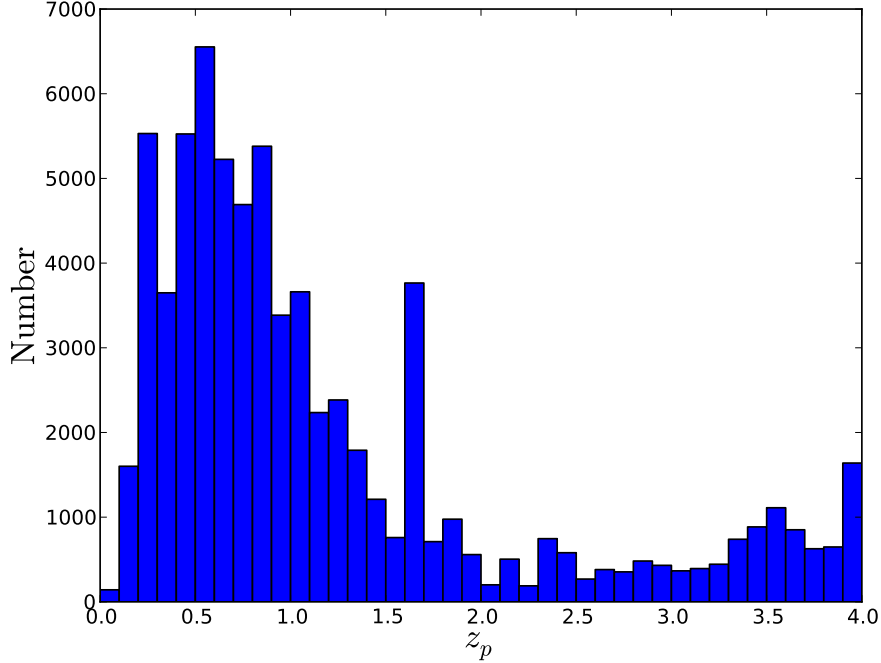


Figure 5.6: Redshift distribution of our field after objects whose flux in  $3''$  aperture is 5 times larger than its error are selected.

outlier fraction is also small in Fig. 5.5 at this redshift range. Further discussions on systematic uncertainties will be made in Section 5.6.4.

## 5.5 Weak Lensing Analysis

### 5.5.1 Simultaneous Multiple-exposure Analysis

In our multiple-exposure shape measurement scheme,  $\chi^2$  in the case of single exposure analysis written as Eq. (4.31) is expanded as

$$\chi^2 = \sum_{\eta=1}^{N_{\text{exp}}} \sum_{\alpha=1}^{N_{\text{pix}}^{(\eta)}} \frac{\left[ f_s^{(\eta)} I^{\text{obs}(\eta)}(\mathbf{x}_\alpha^{(\eta)}) - \sum_i b_i \Phi_i^{\sigma_o E}(\mathbf{b}^{*(\eta)}; \mathcal{W}^{(\eta)}(\mathbf{x}_\alpha^{(\eta)})) \right]^2}{\left( f_s^{(\eta)} \sigma_\alpha^{(\eta)} \right)^2}. \quad (5.23)$$

Here  $\mathbf{b}^{*(\eta)}$  is Gauss-Laguerre coefficients of PSF of exposure  $\eta$ . This quantity is determined based on PSF of each chip provided by the chip-based data reduction

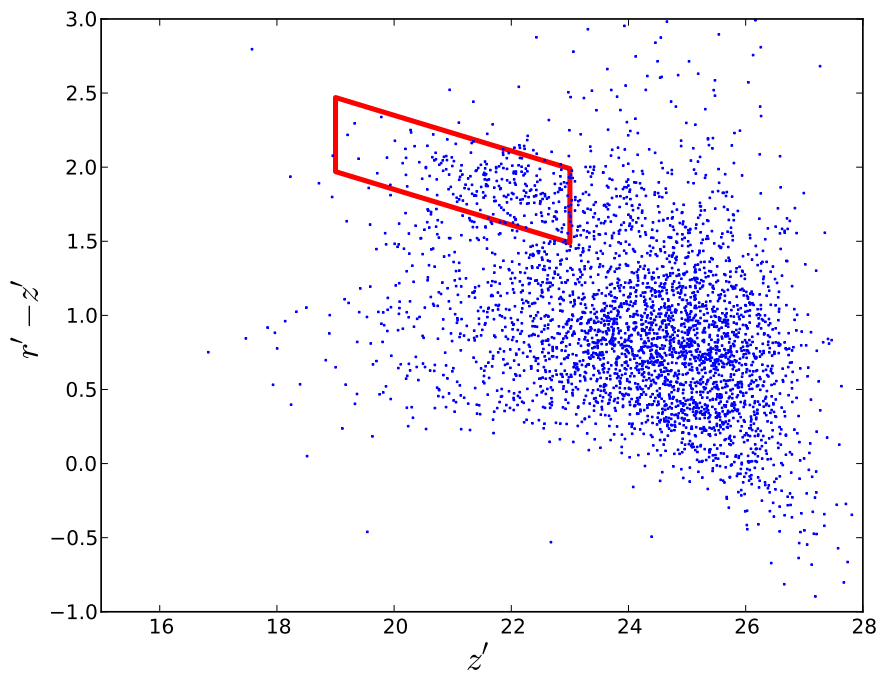


Figure 5.7: Color-magnitude diagram of the center part of our image. The region enclosed by red lines denote bright end of red sequence of ACTJ0022.

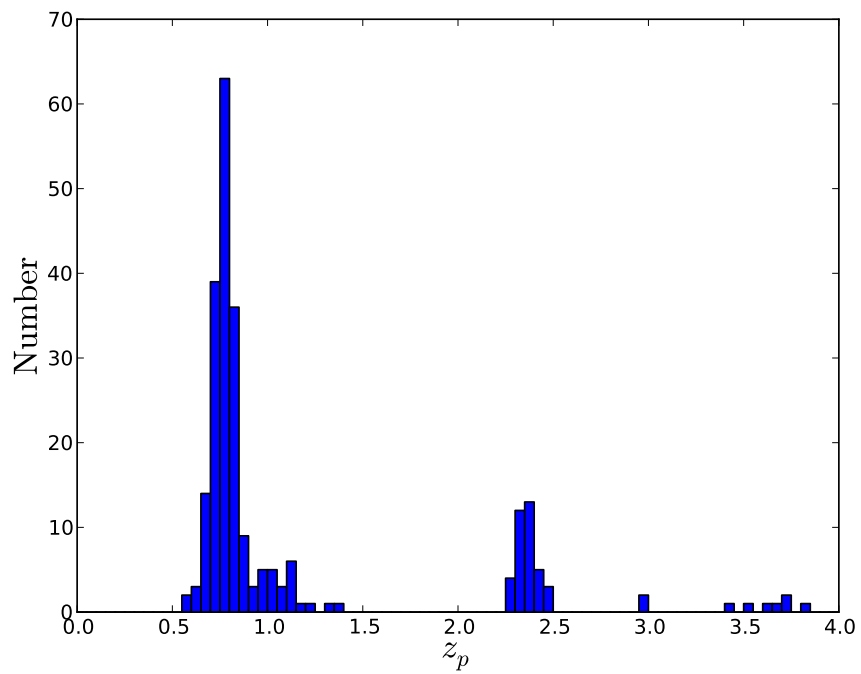


Figure 5.8: Redshift distribution of the red sequence selected in Fig. 5.7.

process, whose details are described later. Picking up pixel values belonging to an objects from each exposure is a little bit tricky. A set of pixels attributed to an object, segmentation, on the stacked image is provided by object detection of SExtractor, as described in Section 5.4.1. The segmentation on the stacked image is first transformed to the celestial coordinates and then transformed to the pixel coordinates of each exposure  $\eta$ , both of which are done by using WCS provided by the stacking process. The transformed segmentation provides a set of pixel indexes on an exposure,  $\mathbf{x}_\alpha^{(\eta)}$ . Then we pick up pixel values in each exposure, which is represented as  $I^{\text{obs}(\eta)}(\mathbf{x}_\alpha^{(\eta)})$  in Eq. (5.23).  $\mathcal{W}^{(\eta)}$  is WCS for the transformation from pixel coordinates on exposure  $\eta$  to celestial coordinates, which is inverse of the one used for transforming the segmentation from celestial coordinates to pixel coordinates of exposure  $\eta$ . Therefore the fitting function  $\Phi^{\sigma_o E}$  is generated on celestial coordinates. Since there is no preference on pixel coordinates of each exposure, it is reasonable to use the celestial coordinates. In addition, in the celestial coordinates, optical distortion, or more precisely coordinate transformation due to optics, is already solved. The optical distortion is not a convolution effect in objects and should not be treated as a part of PSF. Thus fitting an object by the model generated on the celestial coordinates is proper treatment of PSF.  $f_s^{(\eta)}$  is a scale parameter of a chip in exposure  $\eta$ , which is determined by comparing photometry between chips. This quantity is also provided by the image stacking process.

To determine  $\mathbf{b}^{*(\eta)}$ , we first reconstruct a PSF image at the position of galaxy, using principle components of PSF provided by the HSC pipeline. Then the PSF image is fitted by the GLs in the same manner as Section 4.2.2. However, instead of Eq. (4.24) we use

$$I^{*(\eta)}(\boldsymbol{\theta}) = \sum_i b_i^{*(\eta)} \psi_i^{\sigma_*}(\mathcal{W}^{(\eta)}(\mathbf{x}^{(\eta)} - \mathbf{x}_0^{(\eta)})), \quad (5.24)$$

This model function is again generated on celestial coordinates to keep consistency with the galaxy fitting in Eq. (5.23) and obtain purely convolution effect of PSF. Note that the PSF image is normalized to keep the amplitude of the PSF-convolved galaxy fitting models between different exposures unchanged.

Based on the test with simulations in Section 4.3.3, we choose  $(N_{\text{gal}}, N_{\text{PSF}}, N, f_p) = (2, 8, 12, 1.2)$ . Since we want to use galaxies as many as possible to reduce shape noise, we decided to use this configuration even though there will be systematic errors of 5-10%, which will be evaluated later.

## 5.5.2 PSF Determination

To evaluate PSF determination by the HSC pipeline, we checked if PSF size and ellipticity can recover original stellar size and ellipticity. First, to measure these stellar properties, we modelled stellar images, which is flagged as PSFSTAR by the

HSC pipeline, by GLs as described in Section 5.5.1. Using  $\mathbf{b}$  and  $\sigma$  of the GL model, the stellar size and ellipticity are estimated as

$$s = \sigma \exp\left(\frac{b_{11}}{b_{00} - b_{22}}\right), \quad (5.25)$$

$$\eta = \frac{2\sqrt{2}b_{02}}{b_{00} - b_{22}}, \quad (5.26)$$

where the ellipticity is defined as  $\eta = \eta_1 + i\eta_2$  (for details, see Bernstein and Jarvis [10]). Note that  $\eta$  is not same as the definition of reduced shear. We converted  $\eta$  to the quantity equivalent to reduced shear as

$$|e| = \tanh\left(\frac{|\eta|}{2}\right). \quad (5.27)$$

Similarly, PSF size and ellipticity are obtained by fitting PSF image reconstructed at the position of the star.

Looking at the residual of ellipticity and size between stars and PSF, we determined PSF determination parameters described in Section 5.3.2. First, at the star/galaxy separation we set `fluxLim` to higher value (60000) to remove small galaxies. Since these small galaxies have ellipticity, it will contaminate PSF determination. Second, we set `nEigenComponents` and `spatialOrder` to 6 and 4, respectively. If the number of eigen components is small, we do not have eigen images enough to represent variations of PSF. Higher spatial order is needed to represent PSF pattern across the field well. Since typical number of stars used for PSF determination is  $\sim 40$ , a very high spatial order will cause overfitting.

For illustrative purposes, the measured stellar ellipticity and PSF ellipticity on chips of exposure ID=126932 is shown in Fig.5.9 and 5.10, respectively. Also their size is shown as color gradation in these figures. Each panel is tiled in the same alignment as CCD chips on the focal plane. Note that these quantities are measured in celestial coordinates, which means we see pure effect from optics aberration. Even after optical distortion is removed, large ellipticity  $e \sim 0.05$  remains at the edge of field of view.

The residual ellipticity and size of the exposure is shown in Fig. 5.11. Here we define the residual as the quantities of PSF subtracted from that of a star. The residual ellipticity is much smaller than original stellar ellipticity, and the pattern looks random. Also the residual size distributes around  $\sim 0$ . Scatter plot of the stellar ellipticity and residual ellipticity of the exposure is shown in Fig. 5.12. Error bars in this figure is calculated by propagating covariance of  $\mathbf{b}$  shown in Eq. (4.35) to Eq. (5.26) and Eq. (5.27). Note that the error of only stellar ellipticity is used for residual ellipticity. We ignored the error of PSF ellipticity, since the PSF image is much less noisier than stellar image. The average of residual ellipticity and its

error is shown at the bottom part of each panel. Note that all the average are less than  $\sim 10^{-4}$ , which is much smaller than shear signal at outskirts of a cluster ( $g_+ \sim 10^{-2}$ ).

Figure 5.13 shows the correlation between residual ellipticity and stellar ellipticity. If the stellar ellipticity is fully traced by PSF model, there is no correlation. However, there is clear correlation in center chips such as chip ID = 1260325 and 1269324, which is a source of systematic error. The residual ellipticity distributes symmetrically around its average  $\sim 10^{-4}$  with the standard deviation  $\sim 10^{-3}$ . So if we have a number of stars in the area where reduced shear is estimated, the systematic error will be averaged out. We will discuss this effect on our shear estimate in Section 5.5.2.

Finally, we show statistics of all the one hundred chips used for our WL analysis. Each point of Figure 5.14 denotes ellipticity averaged over a single chip. Blue dots denote averaged star ellipticity, and green dots denote averaged residual ellipticity. Typical residual ellipticity of a single chip is  $e_1^{\text{res}} = (1.4 \pm 6.5) \times 10^{-4}$  and  $e_2^{\text{res}} = (0.6 \pm 6.4) \times 10^{-4}$ .

star: 126932

66

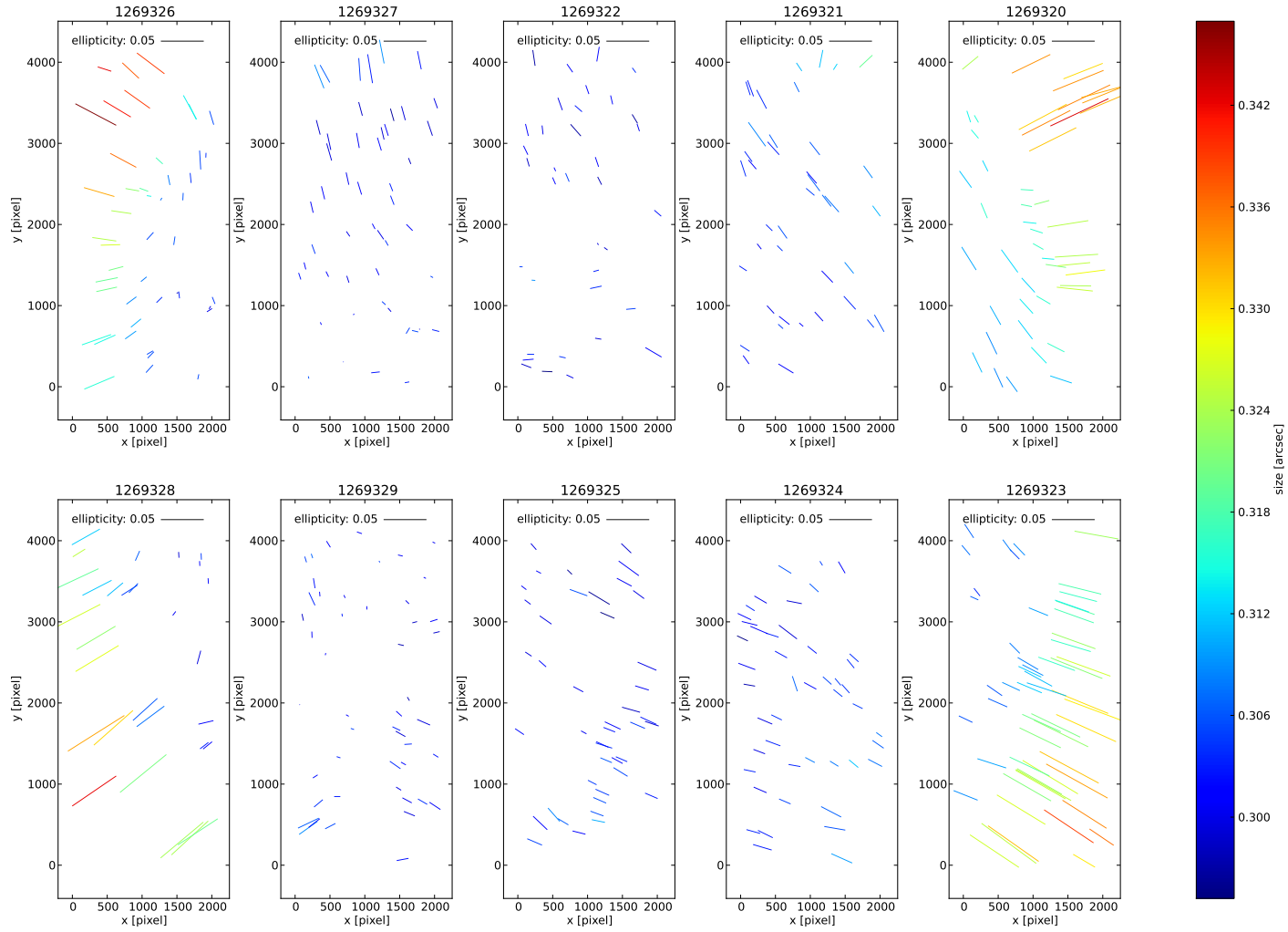


Figure 5.9: Stellar ellipticity and size across chips of exposure ID = 126932.

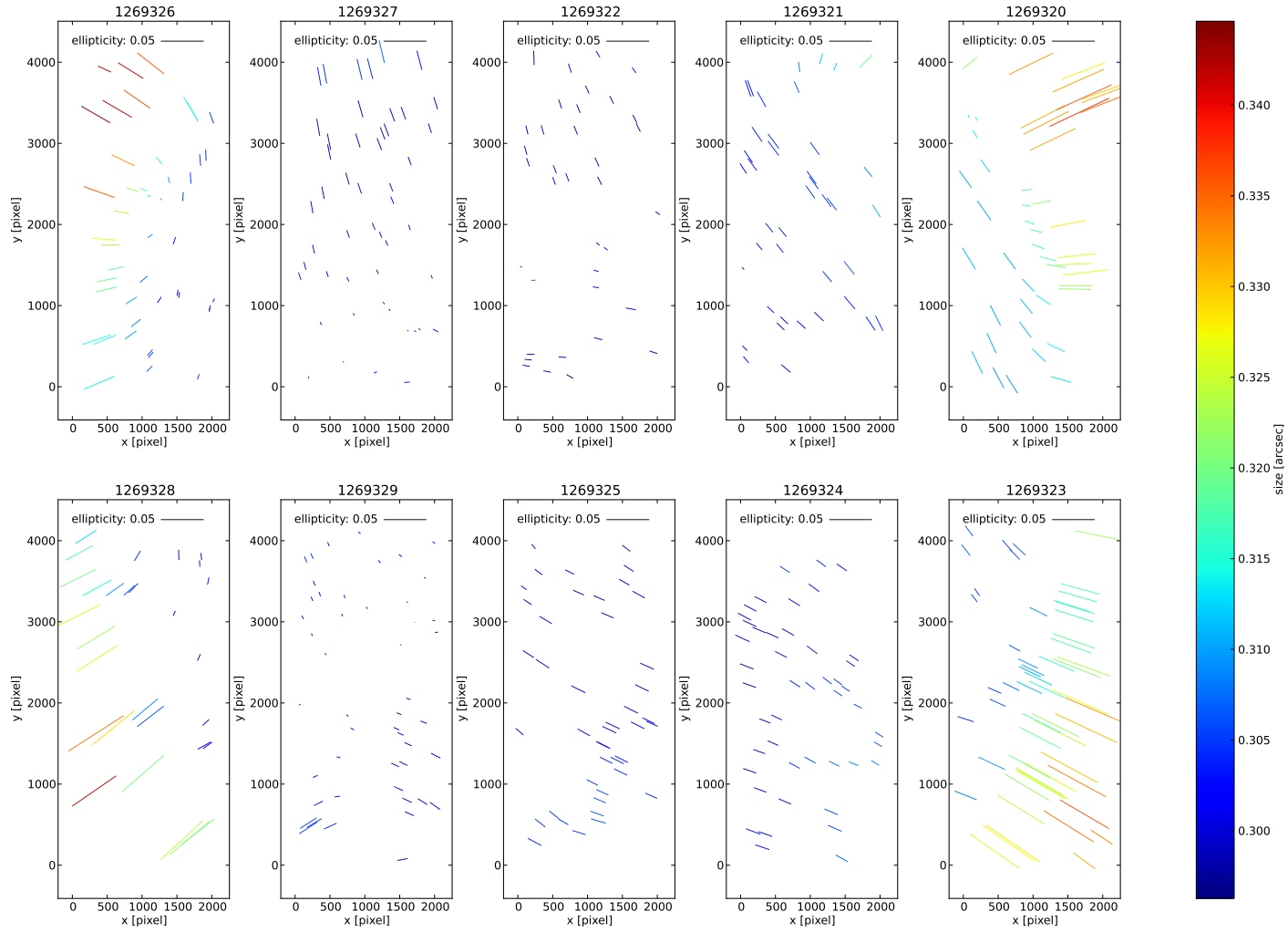


Figure 5.10: PSF ellipticity and size across chips of exposure ID = 126932.

residual (star-PSF): 126932

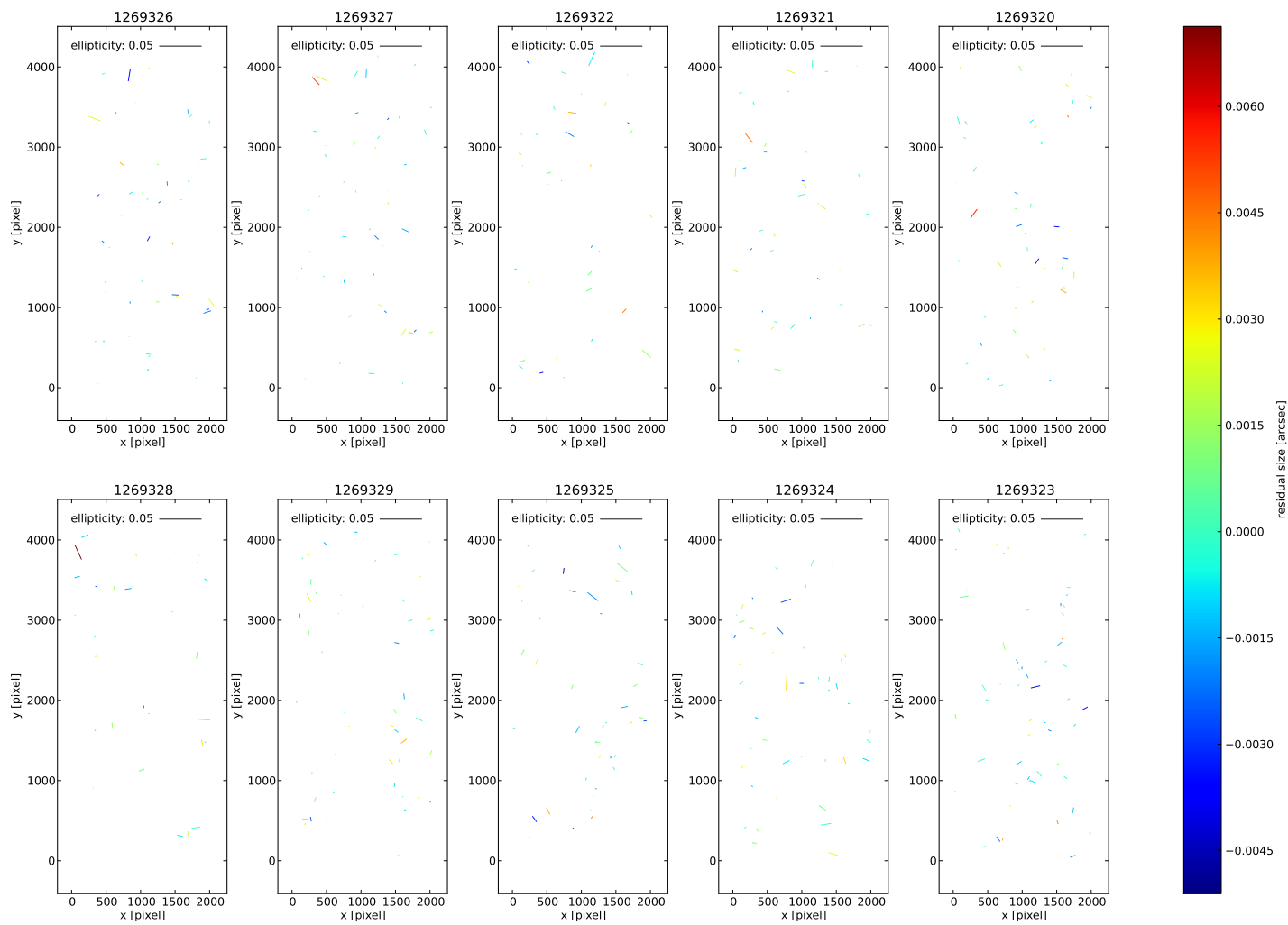


Figure 5.11: Residual ellipticity and size between stars and PSF across chips of exposure ID = 126932.

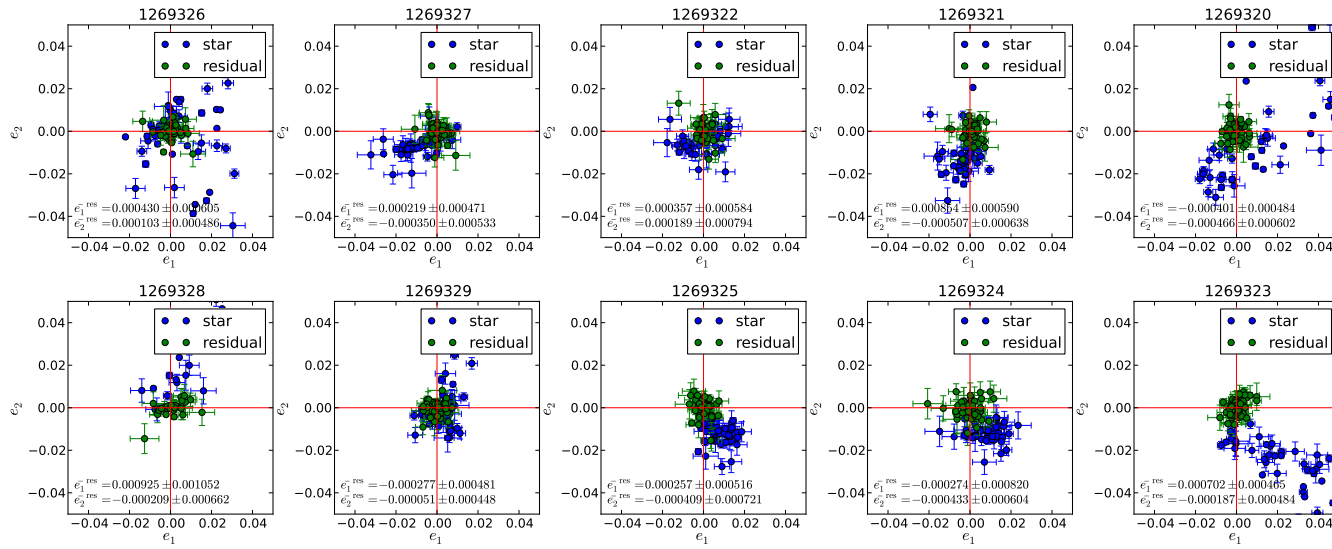


Figure 5.12: Ellipticity distribution on chips of exposure ID = 126932. Blue dots denote stellar ellipticity and green dots denote residual ellipticity between stars and PSF.

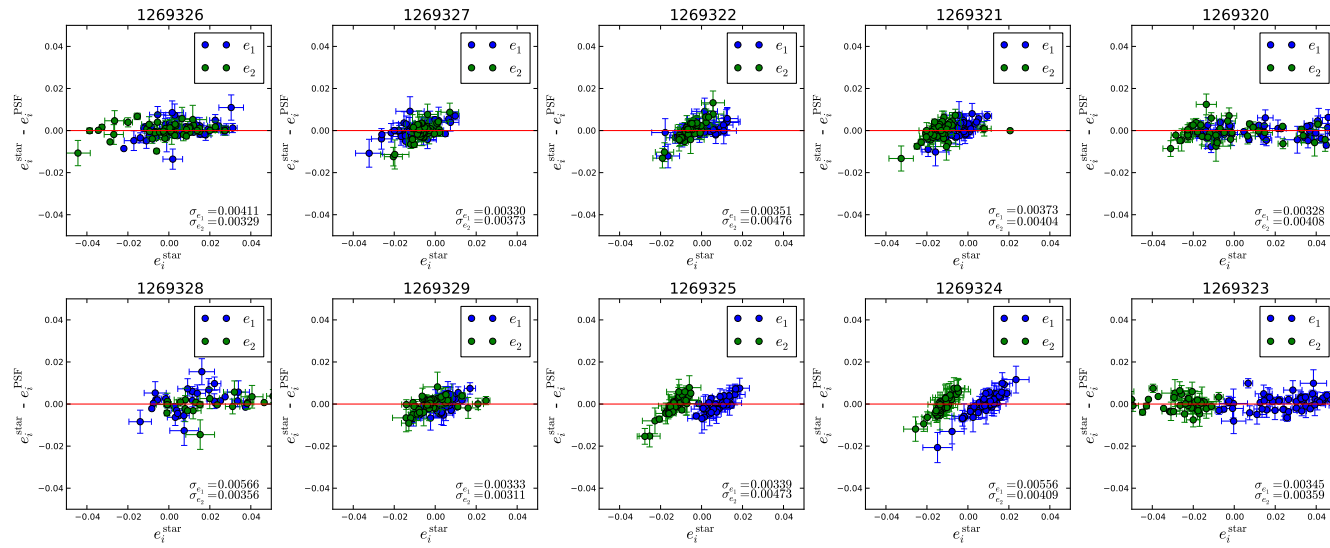


Figure 5.13: Correlation between residual ellipticity and stellar ellipticity on chips of exposure ID = 126932.

### 5.5.3 Star/galaxy Separation

Figure 5.15 shows object size versus magnitude of the  $i'$ -band stacked image, which is taken from `FWHM_IMAGE` and `MAG_AUTO` from catalog generated in Section 5.4.1 by SExtractor, respectively. The sequence having constant FWHM is regarded as stars. We select objects with  $3.0 \text{ pixel} < \text{FWHM} < 4.0 \text{ pixel}$  and  $19.5 < i' < 21.5$  as the stars. The FWHM of the selected samples is  $3.45 \pm 0.17 \text{ pixel}$ . We select objects above  $2\text{-}\sigma$  as galaxies, i.e.,  $\text{FWHM} > 3.8 \text{ pixel}$ . FWHM goes up at the bright end, which means stars are saturated and saturation bleeds enlarge the apparent size. To avoid this contamination, objects with  $i' > 19$  are selected as galaxies.

### 5.5.4 Residual Correlation

In this section, we demonstrate an advantage of the multiple-exposure shape measurement. It is able to test which exposure does not have enough quality in terms of shape measurement. Here we consider the following quantity;

$$R_{ij}^{(\eta)}(\Delta\boldsymbol{\theta}) \equiv \left\langle e_i^{\text{star},(\eta)}(\boldsymbol{\theta}) \left( e_j^{\text{gal},(\text{all})}(\boldsymbol{\theta} + \Delta\boldsymbol{\theta}) - e_j^{\text{gal},(\text{all}-\eta)}(\boldsymbol{\theta} + \Delta\boldsymbol{\theta}) \right) \right\rangle, \quad (5.28)$$

which is hereafter called *residual correlation*. This quantity is correlation between stellar ellipticity at the position  $\boldsymbol{\theta}$  of an exposure  $\eta$  and galaxy residual ellipticity at the position  $\boldsymbol{\theta} + \Delta\boldsymbol{\theta}$ , the difference between galaxy ellipticity determined by multiple-exposure shape measurement using all exposures and galaxy ellipticity determined by the shape measurement using all exposures but the exposure  $\eta$ . If PSF of a particular exposure  $\eta$  is not fully corrected, this effect affects the former galaxy ellipticity, and does not the latter galaxy ellipticity. If the correlation is significantly inconsistent with zero, the exposure  $\eta$  does something bad on the shear estimate, which indicates that the exposure should be removed from the multiple-exposure shape measurement.

We considered ellipticity component  $e_+$  and  $e_\times$ , which means the component along or perpendicular to  $\boldsymbol{\theta}$  and the component at 45 degrees. Figure 5.16 shows four combinations of residual correlation as a function of separation  $|\Delta\boldsymbol{\theta}|$ . Each panel has all ten cases of removed exposure. ID of the exposure removed from multiple-exposure shape measurement is shown in upper right of correlation. Clearly exposure ID = 126934 has significant correlation. PSF of the exposure has coherent large ellipticity ( $\sim 0.04$ ) which might make precise shape measurement difficult. We hereafter remove this exposure from our analysis.

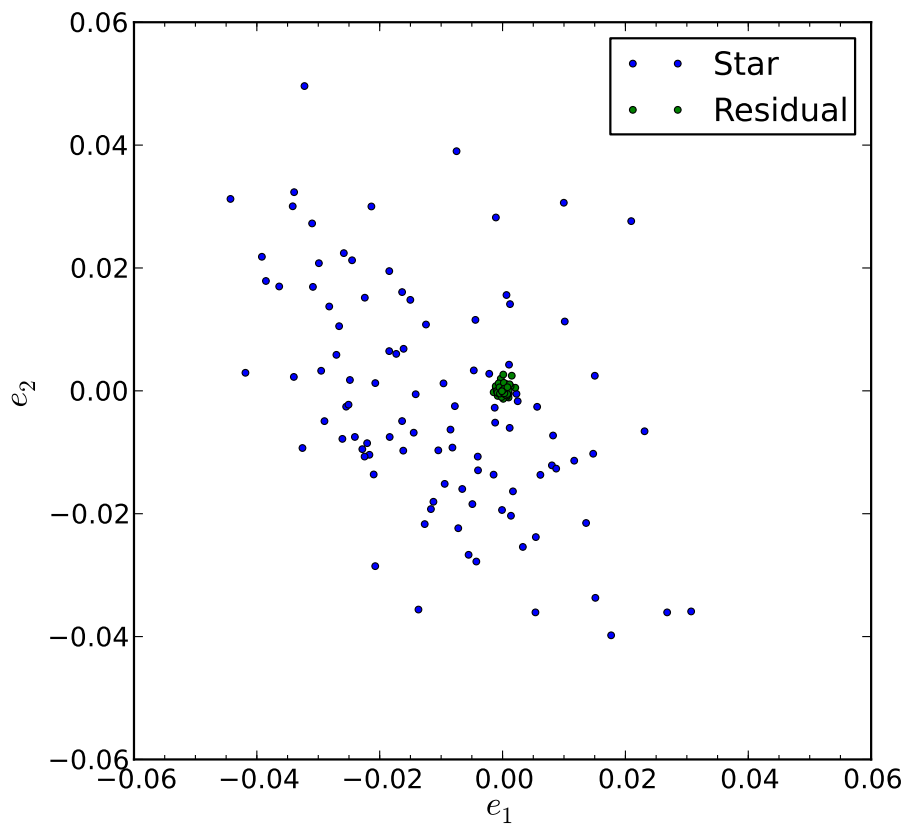


Figure 5.14: Mean ellipticity distribution of all chips used for WL analysis.

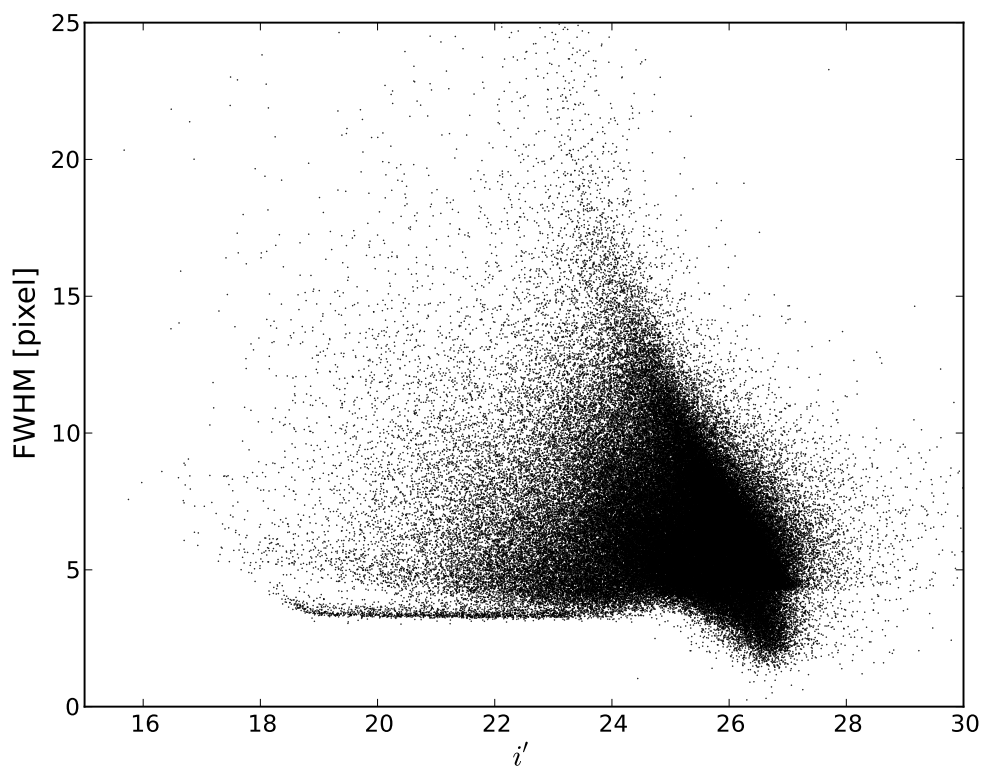


Figure 5.15: Size-magnitude diagram for star/galaxy separation.

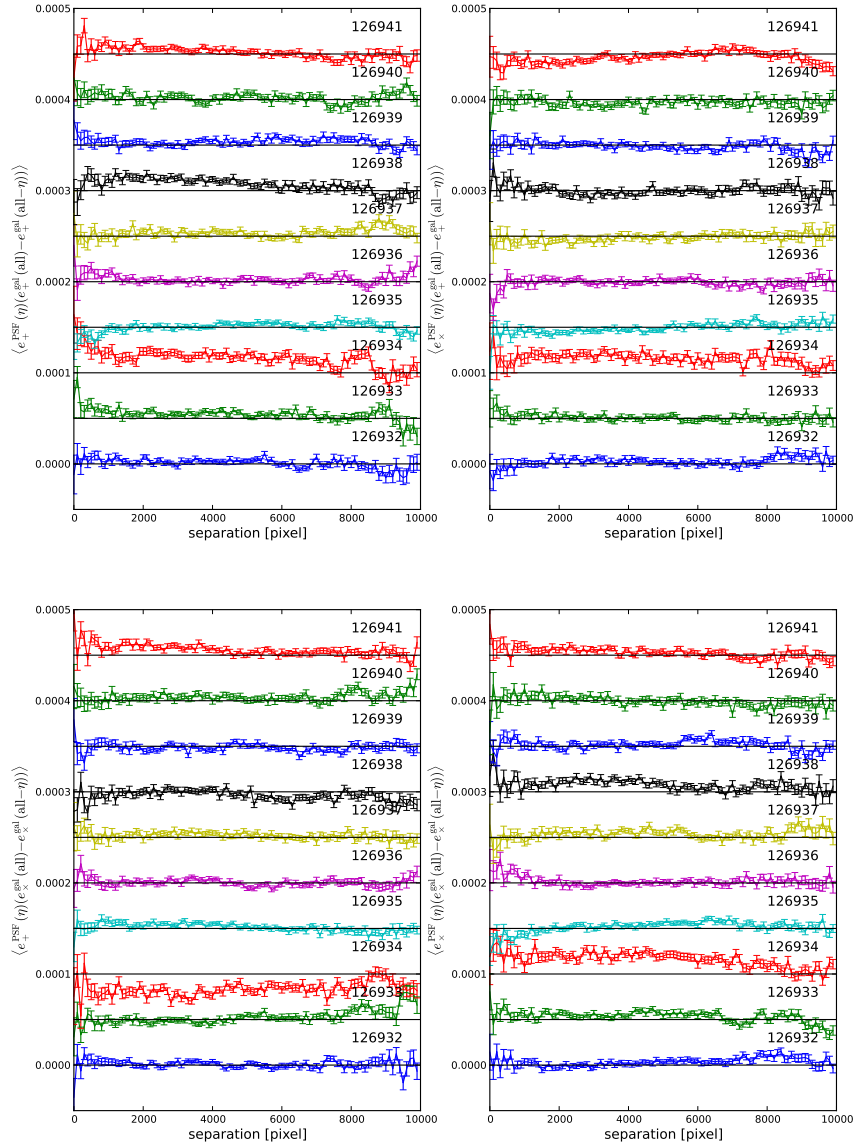


Figure 5.16: Residual correlation to test quality of exposure. Since we use ten exposures in total, there are ten cases of residual correlation. Black horizontal line of each correlation shows zero correlation. ID of the removed exposure is shown at the upper right of each correlation.

## 5.6 Mass Reconstruction

### 5.6.1 Model-dependent Estimate of Cluster Mass

Cluster mass can be defined as follows. First, we find a radius  $r_\Delta$  such that the mean mass density enclosed in sphere whose radius is  $r_\Delta$  is  $\Delta$  times the mean mass density at redshift  $z$ ,  $\rho_m(z) = \rho_m(1+z)^3$ . Then the cluster mass  $M_\Delta$  is defined as

$$M_\Delta = \frac{4\pi}{3} r_\Delta^3 \rho_m(z) \Delta. \quad (5.29)$$

Alternatively, cluster mass can be defined by using critical mass density  $\rho_c(z)$  instead of mean density. We denote the mass defined in this manner as  $M_{\Delta\rho_c}$ . As Mortonson et al. [62] calculated  $M$ - $z$  exclusion curve as described in Section 2.2 using  $M_{200}$ , we use this definition throughout this section.  $M_{\Delta\rho_c}$  will be used in Chapter 6 to compare our result with previous works.

This spherical over-density mass is quite useful from a theoretical view, since dark matter halo mass function derived from numerical simulations is well fitted by analytical formula like Press-Schechter formalism [80], if halo masses are defined by applying top-hat spherical function to simulations.

In order to estimate cluster mass, we employ the dark halo profile proposed by Navarro Frenk & White (NFW) profile [68];

$$\rho_{\text{NFW}}(r) = \frac{\rho_s}{(r/r_s)(1+r/r_s)^2}, \quad (5.30)$$

where  $\rho_s$  is central density parameter and  $r_s$  is the scale radius which divides the profile into two regimes of  $\rho \propto r^{-1}$  and  $\rho \propto r^{-3}$ . This profile fits N-body simulations well over a wide range of halo masses.

Using the dimensionless radius,  $x = D_l\theta/r_s$ , the NFW profile gives the following convergence and shear [71];

$$\kappa_{\text{NFW}} = \begin{cases} \frac{2r_s\rho_s}{\Sigma_{\text{cr}}(x^2-1)} \left[ 1 - \frac{2}{\sqrt{1-x^2}} \operatorname{arctanh} \sqrt{\frac{1-x}{1+x}} \right] & x < 1 \\ \frac{2r_s\rho_s}{3\Sigma_{\text{cr}}} & x = 1, \\ \frac{2r_s\rho_s}{\Sigma_{\text{cr}}(x^2-1)} \left[ 1 - \frac{2}{\sqrt{x^2-1}} \operatorname{arctan} \sqrt{\frac{x-1}{1+x}} \right] & x > 1 \end{cases} \quad (5.31)$$

$$\gamma_{\text{NFW}} = \begin{cases} \frac{r_s\rho_s}{\Sigma_{\text{cr}}} g_{<}(x) & x < 1 \\ \frac{r_s\rho_s}{\Sigma_{\text{cr}}} \left[ \frac{10}{3} + 4 \ln \frac{1}{2} \right] & x = 1 \\ \frac{r_s\rho_s}{\Sigma_{\text{cr}}} g_{>}(x) & x > 1 \end{cases}, \quad (5.32)$$

where

$$g_{<}(x) = \frac{8\text{arctanh}\sqrt{(1-x)/(1+x)}}{x^2\sqrt{1-x^2}} + \frac{4}{x^2}\ln\frac{x}{2} - \frac{2}{x^2-1} + \frac{4\text{arctanh}\sqrt{(1-x)/(1+x)}}{(x^2-1)\sqrt{1-x^2}}, \quad (5.33)$$

$$g_{>}(x) = \frac{8\text{arctan}\sqrt{(x-1)/(1+x)}}{x^2\sqrt{x^2-1}} + \frac{4}{x^2}\ln\frac{x}{2} - \frac{2}{x^2-1} + \frac{4\text{arctan}\sqrt{(x-1)/(1+x)}}{(x^2-1)^{3/2}}. \quad (5.34)$$

The enclosed mass within a sphere of radius  $r_\Delta$  can be obtained by integrating the NFW profile up to  $r_\Delta$

$$M_{\Delta,\text{NFW}} = \frac{4\pi\rho_s r_\Delta^3}{c_\Delta^3} \left[ \ln(1+c_\Delta) - \frac{c_\Delta}{1+c_\Delta} \right], \quad (5.35)$$

where  $c_\Delta \equiv r_\Delta/r_s$ . By equating Eq.(5.29) and (5.35),  $\rho_s$  and  $r_s$  can be written by  $M_\Delta$  and  $c_\Delta$ . Thus the best fit  $M_\Delta$  and  $c_\Delta$  can be obtained by minimizing

$$\chi^2(M_\Delta, c_\Delta) = \sum_i^{N_{\text{bin}}} \frac{[g_{\text{NFW},r_i} - g_{+, \text{data}, r_i}]^2}{\sigma_{+, \text{data}, r_i}^2}, \quad (5.36)$$

where  $i$  runs over the bin number up to  $N_{\text{bin}}$ .  $g_{\text{NFW}}(r_i)$  is obtained as follows. Mathematically,  $g_{\text{NFW},r_i}$  is calculated by

$$g_{\text{NFW},r_i} = \int_{r_{i,\text{in}}}^{r_{i,\text{out}}} 2\pi r dr \frac{\kappa_{\text{NFW}}(r)}{1-\gamma_{\text{NFW}}(r)} \bigg/ \int_{r_{i,\text{in}}}^{r_{i,\text{out}}} 2\pi r dr, \quad (5.37)$$

where  $r_{i,\text{in}}$  and  $r_{i,\text{out}}$  is inner radius and outer radius of the bin, respectively. However, we confirmed the following is a good approximation

$$g_{\text{NFW},r_i} \sim g_{\text{NFW}}(r_i) \equiv \frac{\kappa_{\text{NFW}}(r_i)}{1-\gamma_{\text{NFW}}(r_i)}, \quad (5.38)$$

where  $r_i$  is area mean of bin radius:

$$r_i = \int_{r_{i,\text{in}}}^{r_{i,\text{out}}} 2\pi r^2 dr \bigg/ \int_{r_{i,\text{in}}}^{r_{i,\text{out}}} 2\pi r dr = \frac{2(r_{i,\text{out}}^3 - r_{i,\text{in}}^3)}{3(r_{i,\text{out}}^2 - r_{i,\text{in}}^2)}. \quad (5.39)$$

We estimate critical surface mass density  $\Sigma_{\text{cr}}$  in Eq. (5.31) and (5.32) as

$$\Sigma_{\text{cr}} = \frac{c^2}{4\pi G} D_l^{-1} \left\langle \frac{D_{ls}}{D_s} \right\rangle^{-1}, \quad (5.40)$$

where the mean distance ratio is calculated using photo- $z$

$$R \equiv \left\langle \frac{D_{ls}}{D_s} \right\rangle = \left[ \int_{z_{\text{lens}}}^{\infty} dz_p \frac{dN_{\text{sel},z_p}}{dz_p} \right]^{-1} \int_{z_{\text{lens}}}^{\infty} dz_p \frac{D_{ls}(z_p)}{D_s(z_p)} \frac{dN_{\text{sel},z_p}}{dz_p}, \quad (5.41)$$

where  $dN_{\text{sel},z_p}/dz_p$  is the redshift distribution of background galaxies based on photo- $z$  estimate. This quantity may become source of systematic uncertainty because of inaccuracy of photo- $z$ , which will be discussed in Section 5.6.4.

$g_{+, \text{data}}(r_i)$  is  $i$ -th bin of the tangential shear calculated from data. We first convert  $g_1^{(j)}$  and  $g_2^{(j)}$ , where  $j$  is object ID, in our sample to E-mode and B-mode;

$$g_+^{(j)} = -(g_1^{(j)} \cos 2\phi^{(j)} + g_2^{(j)} \sin 2\phi^{(j)}), \quad (5.42)$$

$$g_{\times}^{(j)} = g_1^{(j)} \sin 2\phi^{(j)} - g_2^{(j)} \cos 2\phi^{(j)}, \quad (5.43)$$

where  $\phi^{(j)}$  is the position angle between the first coordinate axis on the sky and the vector connecting the cluster center and the galaxy position. Then the samples are divided into bins and  $g_{+, \text{data}, r_i}$  is calculated in each bin as follows. First, the observed ellipticity,  $g_+^{(j)}$  and  $g_{\times}^{(j)}$  which are in *shear* definition, is converted to *distortion* definition,  $g_+^{d(j)}$  and  $g_{\times}^{d(j)}$ . Then, using responsivity  $\mathcal{R}$  (Eq. (4.14)) and weighting function  $w$  (Eq. (4.18)), shear and its error in *distortion* definition is calculated as

$$g_{+, \text{data}, r_i}^d = \frac{\sum_j w_j g_+^{d(j)}}{\mathcal{R} \sum_j w_j}, \quad (5.44)$$

$$\sigma_{+, \text{data}, r_i}^d = \frac{\sqrt{\sum_j w_j^2 g_+^{d(j)2}}}{\mathcal{R} \sum_j w_j}. \quad (5.45)$$

Then they are converted to *shear* definition to obtain  $g_{+, \text{data}, r_i}$  and  $\sigma_{+, \text{data}, r_i}$ . Similarly, those quantities for  $\times$  component can be calculated.

## 5.6.2 Results

We again summarize the selections we applied.

- star/galaxy separation FWHM  $> 3.8$  pixel,  $i' > 19$ ,
- background galaxy selection  $0.95 < z_p < 2.0$ .

After these selections, number density of galaxy in the field is  $18.5 \text{ arcmin}^{-2}$ . We further select objects where our shape measurement is reliable. From the test with simulations carried out in Section 4.3.3, we applied the selection  $S/N > 30$  and  $r_e > 0.875$  pixel, where  $S/N$  and  $r_e$  is the definition of signal-to-noise ratio and half light radius of a galaxy defined in Section 4.3. From these simulations, We found that these values correspond to those defined in Section 4.2 as

	setup	$M_{200} [\times 10^{15} M_{\odot}/h]$	$c_{200}$	$\chi^2/\text{d.o.f.}$
case 1	$c_{200}$ : free	$0.72^{+0.33}_{-0.27}$	$> 9.2$	0.83
case 2	$c_{200} = 4.03$	$0.84^{+0.55}_{-0.44}$	N/A	1.12

Table 5.5: Results of NFW profile fitting.

- reliable shape measurement  $\nu > 20$  and  $\sigma_g > 1.2$ .

After applying these selections, number density of the galaxy is reduced to  $3.18 \text{ arcmin}^{-2}$ . We divided the objects lying at  $1.0' < \theta < 10.0'$  into 7 bins, and calculate E-mode and B-mode. The result is shown in Fig. 5.17. The upper panel shows tangential shear and the lower panel shows B-mode. For making it easy to check if the B-mode is consistent with zero, we plotted  $g_{\times}\theta$ , as the error is approximately proportional to inverse of radius. The signal-to-noise ratio of the tangential shear, which is defined as

$$S/N = \sum_{i \in \text{bin}} \left[ \frac{g_{+, \text{data}}(r_i)}{\sigma_{+, \text{data}}(r_i)} \right]^2. \quad (5.46)$$

is 3.61.

Then we performed a fit to obtain cluster mass with  $\Delta = 200$ . We carried out two cases.

- case 1 Fit without fixing concentration parameter  $c_{200}$ . We set a constraint to  $c_{200}$  as it should be lower than 30.
- case 2 Fit with fixing  $c_{200} = 4.03$ , following the prediction by Duffy et al. [26] where they derived power law to represent concentration parameter as a function of cluster mass and redshift by using N-body simulations.

The results of both cases are summarized in Table 5.5, and fitted profiles are shown in Fig. 5.17. For the case 1, we could not obtain  $c_{200}$ , and only lower limit is constrained. Contour map of  $\chi^2$  of the case 1 is shown in Fig. 5.18. This shows  $M_{200}$  and  $c_{200}$  does not degenerate. Although  $c_{200}$  is not determined very well, this does not affect  $M_{200}$  determination so much. Case 2 yields a larger mass estimate error than case 1, although the number of fitting parameters is smaller. This is implied by the fact that the  $\chi^2$  contour at  $c_{200} = 4.03$  is broader than that at  $c_{200} \gtrsim 10$ .

### 5.6.3 Validity Check for Error Bars

To derive the errors of the mass and concentration parameter, we assumed  $\chi^2$ -distribution of Eq. (5.36). It is essential to check whether the tangential shear

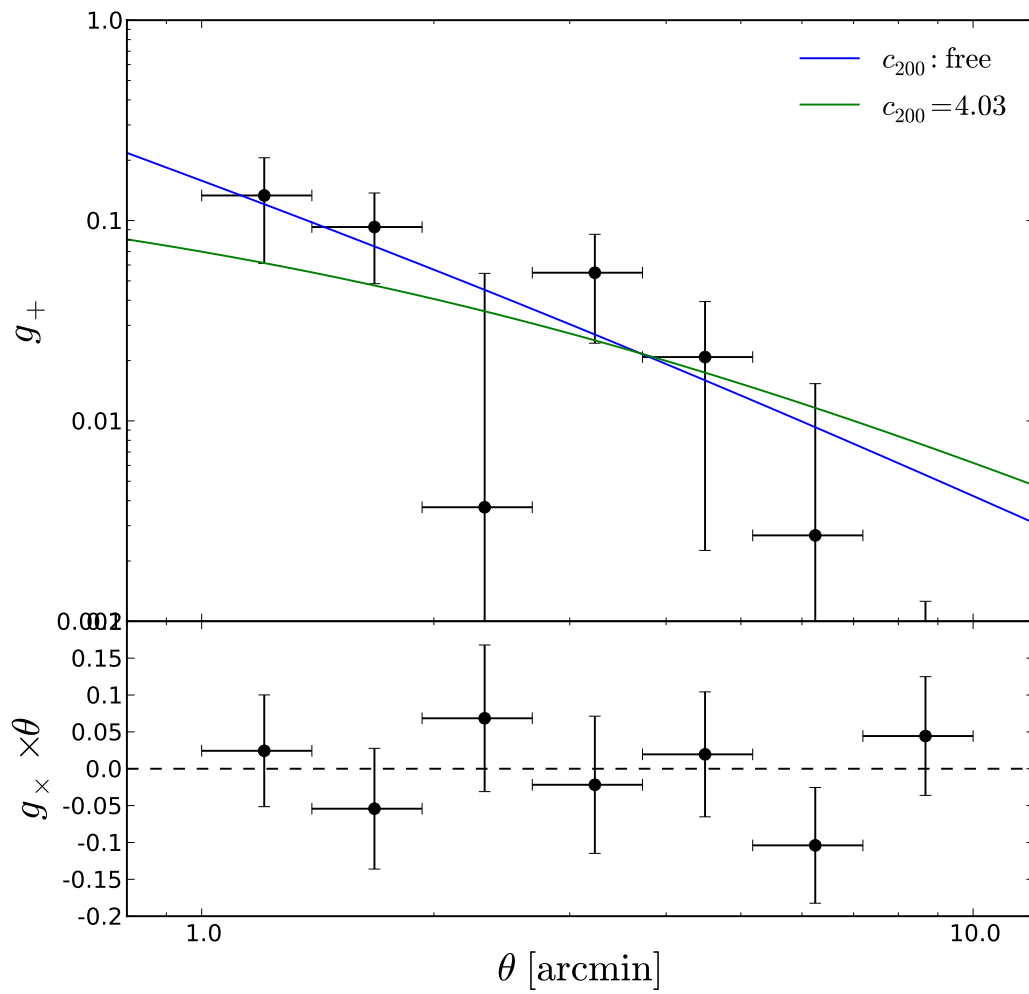


Figure 5.17: Tangential shear of ACTJ0022.

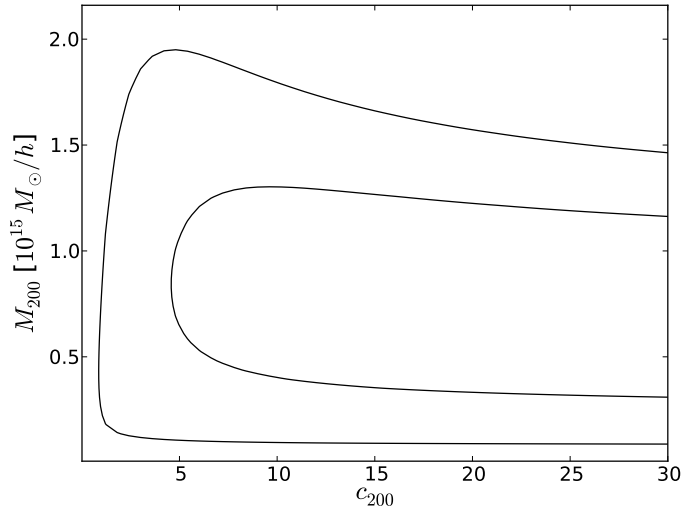


Figure 5.18: Contour map of  $\chi^2$ . The contours show 68% and 95% confidence limits (corresponding to  $\Delta\chi^2 = 2.3, 6.17$ , respectively).

signal at each bin has a Gaussian distribution or not. In addition it is necessary to check whether the error of the tangential shear we used for Eq. (5.36) is close to  $1\text{-}\sigma$  of the Gaussian.

In order to obtain the distribution of the tangential shear signal at a certain bin, we need lots of realizations of measured galaxy ellipticities in the bin, since the signal is obtained by averaging tangential components of galaxies and thus we have only one realization from the data we have. For making realizations, we randomly rotated the orientation of each galaxy ellipticity in the bin, i.e., randomly changing position angle of each galaxy, following the assumption that orientation of galaxies in the sky is random. This means that we intentionally broke the alignment of measured ellipticities induced by cluster WL, and regarded the ellipticities of the rotated galaxies as a realization of intrinsic galaxy ellipticity distribution in each bin. Although the distribution is expected to be slightly wider than that of the real intrinsic ellipticity due to the contribution from WL signals, it does not essentially affect the width we want to look at since WL signals are typically ten times smaller than intrinsic ellipticities of galaxies. Note that the mean of the distribution is no longer equal to the tangential shear signal we obtained, but zero. Nevertheless, this simulation is sufficient to look at the behavior of the error of tangential shear signals. Using the randomly-rotated ellipticities, we calculated the tangential shear by Eq. (5.44) for each realization. Note that in fact this is not a simple average. i.e., it uses responsivity and weight. For each galaxy, we used the same responsivity and

weight as the ones before the rotation, since they are unchanged under the rotation.

Since the tangential shear signal is obtained by averaging tangential components of each galaxy, it is expected that its distribution is close to a Gaussian due to the central limit theorem. However, when the number of galaxies used for calculating the average is small, the distribution is not necessarily close to a Gaussian. For illustrative purposes, we selected a certain number of galaxies  $n_{\text{gal}}$  from the inner most bin of our data, rotated them randomly to make realizations, and made the tangential shear distribution, as shown in Fig. 5.19. We calculated the tangential shear distribution for  $n_{\text{gal}} = 1, 3, 5$  and 10, using  $10^5$  realizations. Note that the weight is taken into account when making the histogram. As  $n_{\text{gal}}$  becomes larger, the distribution becomes close to a Gaussian. Moreover, in the case of  $n_{\text{gal}} = 5$  and 10, the distribution is likely a Gaussian. Since the smallest number of galaxies in the bins used for estimating mass in Section 5.6.2 is 10, all the tangential shear signals in these bins are expected to be close to a Gaussian.

We also investigated how these distributions are close to a Gaussian more quantitatively. Histograms of the tangential shear signal at each bin created by using  $10^5$  realizations are shown in Fig. 5.20. Each Gaussian is fitted by minimizing

$$\chi^2(A, a, \sigma) = \sum_i^{\text{bins}} \left[ \frac{N_i - A \exp\left(-\frac{(g_{+,i}-a)^2}{2\sigma^2}\right)}{\sqrt{N_i}} \right]^2, \quad (5.47)$$

where  $N_i$  is the number of data in  $i$ -th bin of a histogram. The reduced  $\chi^2$  is close to unity, which suggests that the distribution of the tangential shear signal is close to a Gaussian. Table 5.6 shows several estimates of error of the tangential shear signals. The standard deviation calculated from the tangential shear distribution shown in Fig. 5.20 agrees well with  $\sigma$  of Gaussian fitted to the tangential shear distribution shown in Fig. 5.20, which also suggests that the tangential shear distributions are close to a Gaussian. Errors calculated from data by using Eq. (5.45) are also close to these estimates from simulations. The difference is around 5%.

Next, we propagated the tangential shear distributions obtained from the simulations to  $M_{200}$  with  $c_{200}$  fixed to 4.03. This time we used  $2 \times 10^6$  realizations to obtain a smooth distribution. For each realization, we shifted the central value of the tangential shear signal shown in Fig. 5.17 by a tangential shear signal obtained from one realization, and find the minimum of  $\chi^2$  (Eq. (5.36)) by changing  $M_{200}$ .  $M_{200}$  giving the minimum  $\chi^2$  is the best fit  $M_{200}$  for each realization. The obtained distribution is shown in Fig 5.21. We found 68% percentile of the distribution to obtain error. Assuming the central value of mass estimate is same as that obtained in Section 5.6.2, we obtained the mass estimate from the distribution as  $M_{200} = 0.84_{-0.39}^{+0.53} \times 10^{15} M_{\odot}/h$ . This error agrees with that obtained in Section 5.6.2 in  $\sim 10\%$  level. Thus we concluded that calculating the error of tangential shear

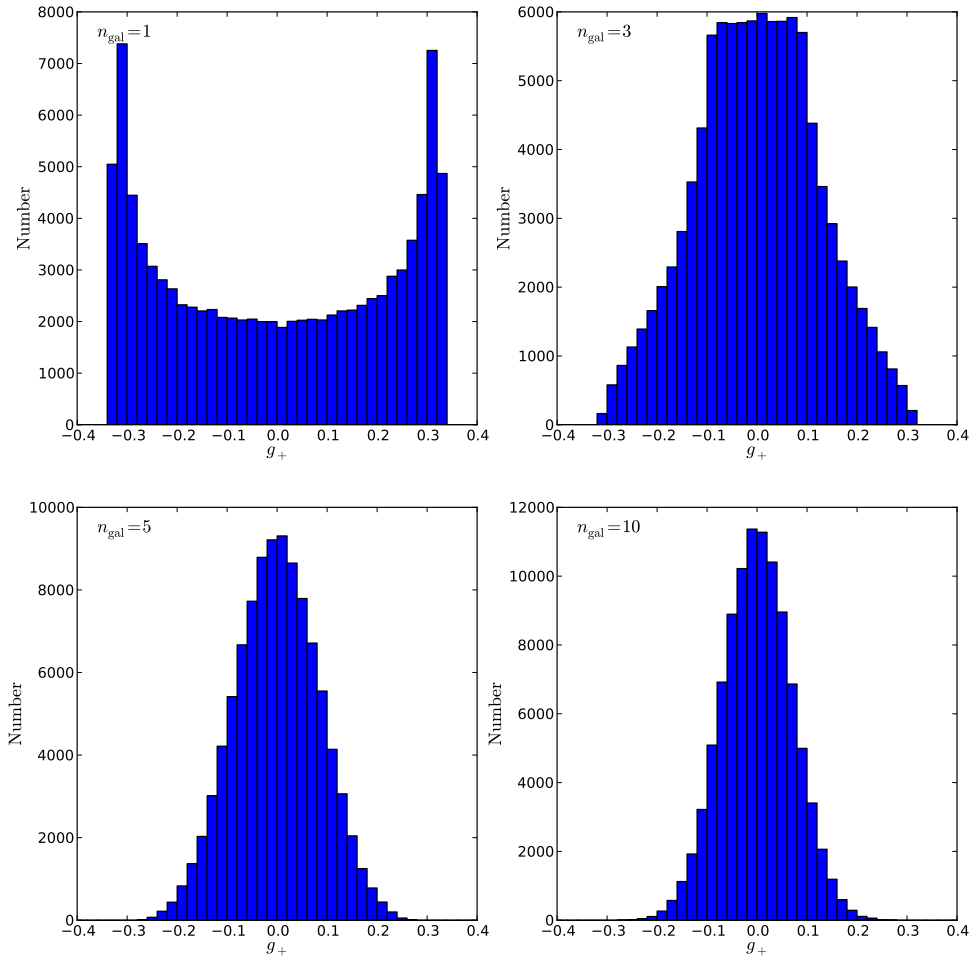


Figure 5.19: Dependency of tangential shear distribution on the number of galaxies used for calculating the tangential shear. We used  $10^5$  realizations to calculate the distribution of each case.

bin	error from data <sup>a</sup>	hist. standard deviation <sup>b</sup>	hist. $\sigma$ <sup>c</sup>
1	0.073	0.0695	$0.0696 \pm 0.0002$
2	0.045	0.0470	$0.0471 \pm 0.0001$
3	0.051	0.0476	$0.0476 \pm 0.0001$
4	0.031	0.02981	$0.02983 \pm 0.00007$
5	0.019	0.01881	$0.01881 \pm 0.00004$
6	0.013	0.01270	$0.01271 \pm 0.00003$
7	0.0091	0.00918	$0.00919 \pm 0.00002$

<sup>a</sup> errors calculated from data by using Eq. (5.45)

<sup>b</sup> standard deviation calculated from tangential shear distribution shown in Fig. 5.20

<sup>c</sup>  $\sigma$  of Gaussian fitted to tangential shear distribution shown in Fig. 5.20

Table 5.6: Estimates of error of tangential shear signals.

signals by Eq. (5.45) and then minimizing  $\chi^2$  (Eq. (5.36)) reasonably gives a good estimate for the error of cluster mass.

### 5.6.4 Systematic Uncertainties

In this section we investigate systematic uncertainties on the cluster mass estimate.

#### Photometric Redshift

We consider two systematic effects caused by inaccuracy of estimating redshifts of galaxies. The first is dilution effect, which is caused by the uncertainty of determining redshift of each galaxy. If the background sample we selected in Section 5.4.2 have foreground galaxies, they dilute tangential shear signal. Using the spec- $z$  and photo- $z$ , this contamination rate is calculated as

$$f_c \equiv \frac{N_{\text{sel},z_p}(z_s < 0.8)}{N_{\text{sel},z_p}}, \quad (5.48)$$

where  $N_{\text{sel},z_p}$  is the number of galaxies after a selection based on photo- $z$  is applied.

The second is the uncertainty of the mean distance ratio in Eq. (5.41). If we know the true redshift distribution of the objects selected by photo- $z$ ,  $\frac{dN_{\text{sel},z_p}^{\text{true}}}{dz_s}$ , the true distance ratio is written as

$$R_{\text{sel},z_p}^{\text{true}} \equiv \left\langle \frac{D_{ls}}{D_s} \right\rangle^{\text{true}} = \left[ \int_{z_{\text{lens}}}^{\infty} dz_s \frac{dN_{\text{sel},z_p}^{\text{true}}}{dz_s} \right]^{-1} \int_{z_{\text{lens}}}^{\infty} dz_s \frac{D_{ls}(z_s)}{D_s(z_s)} \frac{dN_{\text{sel},z_p}^{\text{true}}}{dz_s}. \quad (5.49)$$

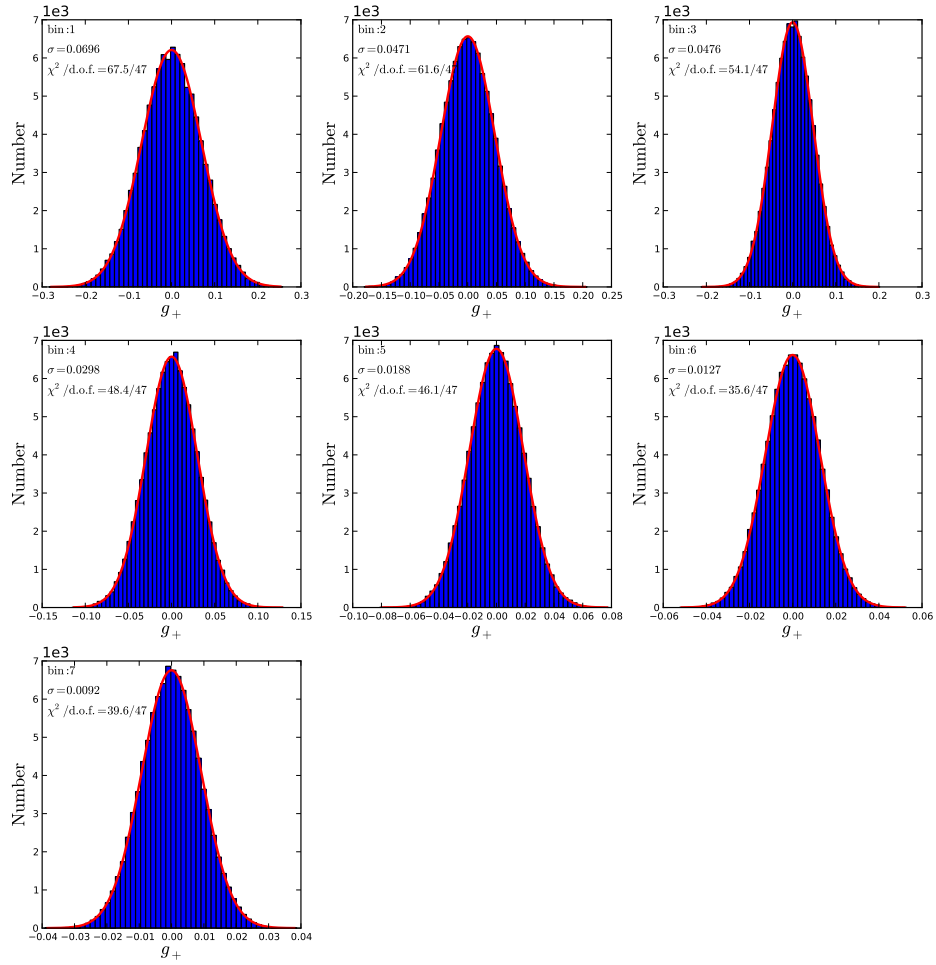


Figure 5.20: Tangential shear distribution of each bin obtained from  $10^5$  realization. Bin ID shown at upper left of each panel increases from the inner bin to outer bin in Fig. 5.17.

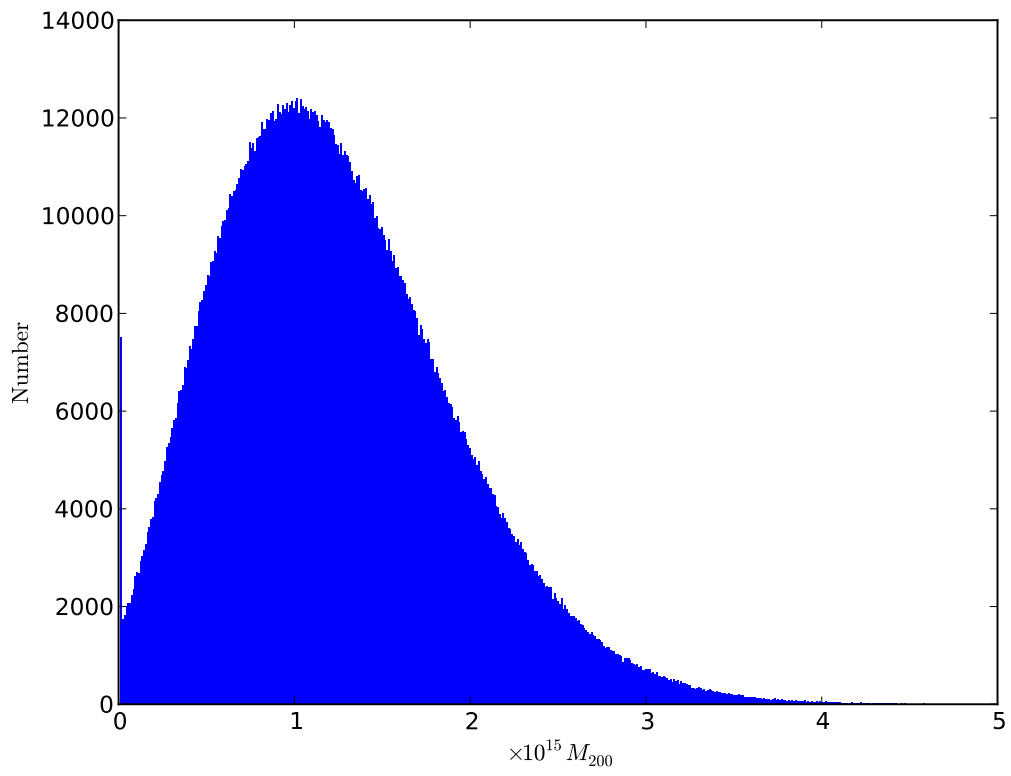


Figure 5.21: Distribution of cluster mass obtained by propagating the distribution of tangential shear obtained by simulations.

Note that the integral begins from  $z_{\text{lens}}$  on  $z_s$  plane, since objects actually in front of the lens is not lensed. Comparing the mean distance ratio derived from photo- $z$  written in Eq. (5.41) with  $R_{\text{sel},z_p}^{\text{true}}$ , we are able to estimate the systematics.

To estimate these systematic errors, we have to know both of spec- $z$  and photo- $z$ . Since we have only a few spec- $z$  for objects in our field, as used in magnitude zero point re-calibration in Section 5.4.2, we made two other catalogs having spec- $z$  and photo- $z$  for all the objects. In the process of making the catalog, we regarded photo- $z$  derived from COSMOS 30-band photometric catalog as spec- $z$ , as well as described in Section 5.1

The one is the mock simulation catalog, which is generated based on Nishizawa et al. [70]. This catalog has the magnitude of each band obtained by convolving the filter response to a given SED. The catalog is slightly different from the observation; the limiting magnitude and photometric band selection are  $i' = 26.2$  and  $Bi'z'Y$ , and galaxy types are randomly distributed over the redshift. The  $i'$ -band magnitude and spec- $z$  distribution is realistic, since they are matched to the COSMOS photometric catalog. We run the photo- $z$  code for this catalog to obtain photo- $z$ .

The other is toy-spectroscopic redshift catalog (hereafter toy-spec $z$ ), which is generated based on the COSMOS 30-band photo- $z$  catalog. We run photo- $z$  code to obtain photo- $z$  using  $Br'i'z'$  magnitudes of the COSMOS catalog. Note that we are not able to use  $Y$ -band, since the COSMOS catalog does not have it. Since the limiting magnitude of our sample (25.6 th) is different from that of COSMOS (26.0 th), we have to modify redshift distribution of the COSMOS catalog to use them in Eq. (5.49):

$$\left. \frac{dN_{\text{sel},z_p}^{\text{true}}}{dz_s} \right|_{\text{ACTJ}} = \left. \frac{dN_{\text{sel},z_p}^{\text{true}}}{dz_s} \right|_{\text{COSMOS}} \times \frac{dN/dz|_{\text{theory}}(i' < 25.6)}{dN/dz|_{\text{theory}}(i' < 26.0)}, \quad (5.50)$$

where  $dN/dz|_{\text{theory}}$  is obtained from fitting formula for 30-band photo- $z$  sample provided by Ilbert et al. [34].

Table 5.7 and 5.8 show the results. In addition to the selection we actually made,  $0.95 < z_p < 2.0$ , the result for selection  $0.95 < z_p$  is shown in the tables. After cutting out  $z_p$  above 2.0, the contamination rates are reduced by 10% or less. This fact means that the selection we decided in Section 5.4.2 also works for the simulations to remove outliers. Although the contamination rates are slightly different between the two simulations, we estimate the systematics as  $f_c = 0.10$ . The systematics are propagated to the mass estimate as follows. First, due to the contamination, the dilution of true shear is estimated as

$$\langle \gamma \rangle_{\text{meas}} = (1 - f_c) \langle \gamma \rangle_{\text{true}}. \quad (5.51)$$

Thus we estimate the systematic uncertainty due to dilution effect to be +10% of the tangential shear signal. Shifting the center value of tangential shear signal of

each bin by +10% and fitting the tangential shear signals again, we found that of mass estimate is shifted by +12%.

From Table 5.8, we adopt  $\pm 7\%$  systematics for the measured mean distance ratio,  $R^{\text{meas}}$ . The systematic uncertainty  $\delta R^{\text{meas}}$  is propagated to the reduced shear of NFW profile as

$$g_{NFW}(r_i) \rightarrow g_{NFW}(r_i) \left( 1 + \frac{\delta R^{\text{meas}}}{R^{\text{meas}}} \right), \quad (5.52)$$

which results in the shift of the center value of the cluster mass by  $\pm 8\%$ .

setup	$0.95 < z_p < 2.0$	$0.95 < z_p$
mack simulation	0.10	0.25
toy-specz	0.07	0.18

Table 5.7: Contamination rates.

setup	$0.95 < z_p < 2.0$	$0.95 < z_p$
mack simulation	0.29(0.30)	0.26(0.38)
toy-specz	0.30(0.28)	0.27(0.31)

Table 5.8: Estimated true mean distance ratio. Values in the parenthesis are the distance ratio calculated by using photo- $z$

## PSF Determination

As described in Section 5.5.2, there are correlations between residual ellipticity and stellar ellipticity. However, they symmetrically distribute around its average ( $\sim 10^{-4}$ ), so that they will be reduced to  $\sim 10^{-4}$  level if a lot of stars are used for determining PSF. We calculated the tangential component of residual ellipticity to directly investigate its effect on tangential shear. Its standard deviation all over the exposures,  $\sigma_{SN}^*$ , is 0.0042.

We estimate this effect for each bin of tangential shear as follows. First, the shape noise of each galaxy is naively written as

$$\sigma_+ = \frac{\sigma_{SN}}{\sqrt{n_{\text{gal}}A}}, \quad (5.53)$$

where  $\sigma_{SN}$  is the standard deviation of galaxy ellipticity,  $n_{\text{gal}}$  is the number density of galaxies, and  $A$  is an area of the bin. On the other hand, the scatter originating from residual ellipticity can be written as

$$\sigma_+^* = \frac{\sigma_{SN}^*}{\sqrt{n_* n_{\text{exp}} A}}, \quad (5.54)$$

where  $n_*$  is the stellar number density and  $n_{\text{exp}}$  is the number of exposures. Here we assumed residual ellipticities in different exposures do not correlate with each other. By equating Eq. (5.53) and (5.54), we obtain

$$\sigma_+^* = \sqrt{\frac{n_{\text{gal}}}{n_* n_{\text{exp}}} \frac{\sigma_{SN}^*}{\sigma_{SN}}} \sigma_+. \quad (5.55)$$

We used 9 exposures for the multiple exposure fitting. From Section 5.6.2,  $n^* \sim 3.18$ , and we found  $n^* \sim 0.45 \text{ arcmin}^{-2}$  and  $\sigma_{SN} \sim 0.18$ . Therefore  $\sigma_+^* \sim 0.02\sigma_+$ . This means that residual ellipticity increases the shape noise by only  $7 \times 10^{-3}\%$ . Thus we neglect these systematics.

### Shape Measurement

We carried out similar simulations of the EGL method described in Section 4.3, in order to quantify the systematic uncertainties from shape measurement precisely. We divided  $S/N$ - $r_e$  plane, where  $S/N$  and  $r_e$  is signal-to-noise ratio and half light radius of a galaxy as defined in Section 4.3.2, into meshes whose central values are  $S/N = (20, 30, 40, 80, 150)$  and  $r_e = (0.8, 0.875, 1.0, 1.2, 1.8, 2.5, 3.3)$ . The border of each mesh is the middle of the centers of neighboring meshes. Figure 5.22 is the bias map on the  $S/N$ - $r_e$  plane which shows multiplicative bias in terms of  $b = 100(g_{\text{meas}} - g_{\text{true}})/g_{\text{true}}$ , where  $g_{\text{meas}}$  is measured shear and  $g_{\text{true}}$  is true shear. We calculated total bias by averaging these biases with weighting the number of galaxy in each mesh. The value of borders are converted to the parameters of the EGL method,  $\nu$  and  $\sigma_g$ , as described in Section 5.6.2. Note that although in  $S/N < 30$  there is large bias on small galaxies, our selection is  $S/N > 30$ , as described in Section 5.6.2. The total bias is  $-6\%$  compared to true value of shear, which corresponds to the systematic uncertainty increasing the mass estimate by  $+7\%$ .

### Combine Systematic Uncertainties

The systematic uncertainties with respect to the center value of mass estimate are summarized in Table 5.9.

For fitting of case 1 in Section 5.6.2, after combining the systematic uncertainties, mass estimate becomes

$$M_{200} = (0.72_{-0.27}^{+0.33}(\text{stat.})_{-0.06}^{+0.12}(\text{syst.})) \times 10^{15} M_{\odot}/h. \quad (5.56)$$

Therefore statistical error is dominant in the cluster mass estimate.

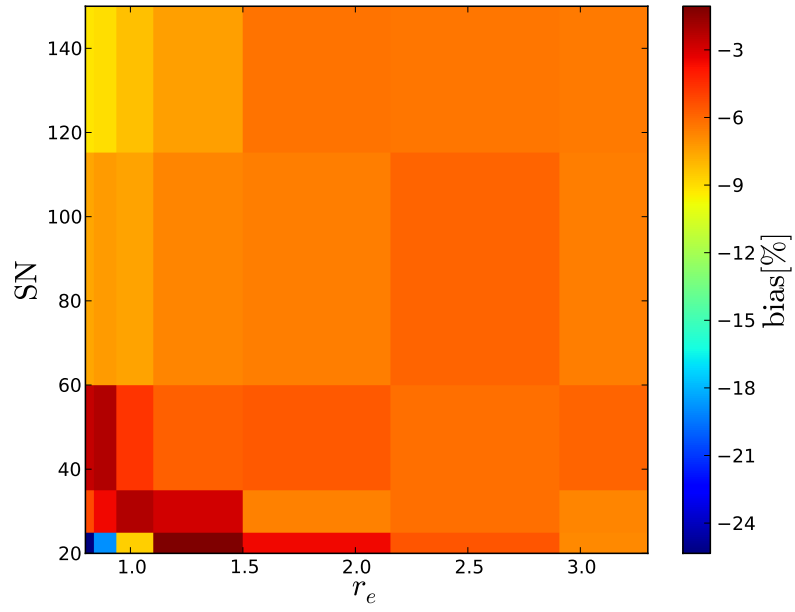


Figure 5.22: Bias map of shape measurement.

source	systematics [%]
dilution	+12
mean distance ratio	$\pm 8$
shape measurement	+7
total <sup>a</sup>	+16 -8

<sup>a</sup> added in quadrature

Table 5.9: Systematic bias.

# Chapter 6

## Discussion

### 6.1 Comparison with Previous High-redshift Cluster Lensing Measurement

Although there are several precedents that carried out WL measurements of high-redshift galaxy clusters, most of them were done by using the Hubble Space Telescope (HST). Since the HST is in space, the PSF is much smaller than that of ground-based telescopes. Shapes of distant, small galaxies can be extracted efficiently once one has deep images. For example, Umetsu and Futamase [96] detected dark matter concentrations in the field of Cl 1604+4304 ( $z = 0.897$ ) through WL measurements on images taken by the Wide-Field Planetary Camera 2 (WFPC2), and Jee et al. [36] performed systematic studies of 22 high-redshift clusters ( $z \gtrsim 1$ ) taken by the Advanced Camera for Surveys (ACS) by estimating mass through weak lensing measurements. Note that the field of view of these instruments (WFPC2:  $2.5' \times 2.5'$  and ACS:  $3' \times 3'$ ) is much smaller than that of the Suprime-Cam ( $34' \times 27'$ ), and it is difficult to observe an entire cluster by a single field of view.

As a pioneering work done by using a ground-based telescope, Luppino and Kaiser [50] carried out WL measurements on MS 1054-03 ( $z = 0.83$ ) through the UH 2.2m telescope. They detected tangential shear signals at the 5-10% level, and demonstrated the signals change depending on object selection by  $I$ -band magnitude and  $R-I$ . A few other works also measured high-redshift cluster lensing and showed tangential shear signals. For example, Clowe et al. [23] observed cluster of galaxies whose redshift of 0.807 (CL J1122.9-1136) and 0.960 (CL J1103.7-1245), using ESO Distant Cluster Survey (EDisCS) images taken by Focal Reducer and low dispersion Spectrograph (FORs2) of the Very Large Telescope (VLT). The images consist of  $IVB$  bands, and they used color cuts to select background galaxies. It seems that the tangential shear signal of CL J1122.9-1136 is significant, while that of CL J1103.7-1245 is not.

Our work is one of the few cases in which tangential shear is significantly detected. The unique point of our work is that we used photometric redshift to select background galaxies. For low redshift clusters ( $z \lesssim 0.3$ ), when we carry out Subaru/Surpime-Cam-like deep observations, most of observed galaxies are in the background. Thus color cuts work efficiently and robustly (for example, see Okabe et al. [76]). However, for our high-redshift cluster, as seen in Fig. 5.6, more than half of the observed galaxies lie in the foreground. Thus photometric redshift gives a more robust background galaxy selection than the color cuts.

## 6.2 Concentration Parameter

Our NFW fit implies a very high concentration parameter compared to the theoretical prediction,  $c_{200} = 4.03$ . The observed tangential shear signals at outer radii become suddenly small ( $g_+ \ll 0.01$ ), and the fit does not converge.  $c_{200}$  is bounded to the upper limit of the fit, 30, with a lower bound is 9.2. This is partly because the tangential shear signals are noisy. The error of the signals depends on the number density of the background galaxy  $N$ , since the error is dominated by shape noise which scales with  $N^{-1/2}$ . Deeper images may help to suppress the shape noise. However, as we will discuss in Section 6.4 it is difficult to suppress the shape noise effectively.

Another possible reason is that we might be looking at only the outer region of the cluster. Since  $r_{200}=1.8$  Mpc ( $3.9'$ ), the characteristic scale of the NFW profile is  $r_s \sim 0.4$  Mpc which corresponds to  $\sim 1'$ , if we assume a concentration parameter  $c_{200} \sim 4$ . As shown in Fig. 5.17, we do not use tangential shear information at radii smaller than  $\sim 1'$ . Thus we might only be looking at a steep part of the NFW profile proportional to  $r^{-3}$ . It is impossible to obtain significant tangential shear signals at such small radii, since the number of the galaxy that can be used for deriving the tangential shear is so small that signal-to-noise ratio in a bin is smaller than 1. Strong lensing may help to provide information in such small radii, but we do not find any apparent signal in our image. Observations by space telescopes such as the HST might find strong lensing through its high resolution images.

Broadhurst et al. [17] reported high concentration,  $c_{\text{vir}} \sim 14$ , of A1689 ( $z = 0.183$ ), compared to the expected value ( $c_{\text{vir}} \sim 4$ ), so clusters with such high concentration values exist. The large concentration parameter might be due to selection bias of the SZ effect. If the hot gas in a cluster is highly concentrated, the SZ signal becomes stronger. In order to address this issue, more systematic studies of WL mass of SZ-selected clusters should be done. As future wide-field weak lensing surveys, such as the HSC and DES, are carried out such statistics should be available.

## 6.3 Systematic Uncertainties from Physics

### 6.3.1 Halo Triaxiality

In Section 5.6, we constrained the cluster mass by deprojecting two-dimensional lensing information under the assumption that mass distribution is spherically symmetric. However, the  $\Lambda$ CDM predicts that dark halos are in general triaxial, which can be naturally expected because of the filamentary nature of structure formation [37]. Thus the result assuming spherical symmetry can be biased.

Oguri et al. [74] estimated the halo triaxiality effect in lensing measurements. They considered a triaxial halo with the virial mass  $M_{\text{vir}} = 10^{15} h^{-1} M_{\odot}$  at  $z = 0.3$ , and a three-dimensional NFW-like profile with typical triaxiality, following the model mass profile given in Jing and Suto [37]. The three-dimensional profile is then projected onto two-dimensional profiles. Note that the two-dimensional profiles are different, depending on the direction of projection. They created a convergence map for each two-dimensional profile, and saw how the estimate of the cluster mass and concentration parameter is changed by fitting the convergence map derived from the spherical NFW profile. They found that the convergence map projected along the major (minor) axis yields an overestimation (underestimation) by 20-30% in both the mass and concentration parameter.

Similarly, our mass estimation can be biased by  $\pm 20\text{-}30\%$  due to triaxiality, which corresponds to  $\pm 50\text{-}70\%$  ( $\pm 30\text{-}50\%$ ) of the statistical error when concentration parameter is free (fixed).

### 6.3.2 Off-Centering Effect

When fitting the NFW profile to the tangential shear profile, we assumed that the BCG position (R.A.=00:22:13.01, Dec.=−00:36:33.51 (J2000) according to our astrometry) is the center of the cluster. The cluster center, or potential minimum, can be determined by using variety of methods such as X-ray, SZ, and satellite velocities, which means that the BCG is not necessarily the same as the potential minimum. If the BCG has offset from the potential minimum and the tangential shear profile is calculated assuming the BCG is the center, the mass estimate is reduced.

According to studies that compared the BCG position with the cluster center defined by X-ray intensity or average satellite velocity, typical displacement is about 2-3% of the virial radius [97][46][13]. We looked at how much our mass estimate is changed when the cluster center has such an offset. First, in order to obtain virial radius, we re-performed NFW fitting by replacing Eq. (5.29) with

$$M_{\text{vir}} = \frac{4\pi}{3} r_{\text{vir}}^3 \rho_c(z) \Delta_{\text{vir}}, \quad (6.1)$$

where

$$\Delta_{\text{vir}} = 18\pi^2(1 + 0.4093w^{2.71572})\Omega_{m,0}(1 + z)^3 E(z)^{-2}, \quad (6.2)$$

$$w = \frac{(\Omega_{m,0}^{-1} - 1)^{1/3}}{1 + z}, \quad (6.3)$$

where we use Nakamura and Suto [65],  $E(z)$  is defined in Eq. (2.18), and  $z$  is the redshift of a cluster. Note that in the case of ACTJ0022,  $\Delta_{\text{vir}} \sim 147$ . After the fit, we obtain  $r_{\text{vir}} = 1.7$  Mpc ( $r_{\text{vir}} = 1.8$  Mpc) when the concentration parameter is free (fixed). We then set offsets to  $(\Delta x, \Delta y) = 0.03r_{\text{vir}}(\cos \theta, \sin \theta)$  from the position of BCG, where  $\theta$  is the position angle with respect to the direction of R.A. We consider 8 offsets with  $\theta = 0, 45, 90, 135, 180, 215, 270, 315$  in degrees, and how the mass estimate is changed. We find that systematically the mass estimate with each offset is reduced. When the concentration parameter is free (fixed), 7 (6) out of 8 offsets yield lower mass estimates and the mass estimate averaged over 8 offset cases is reduced by  $\sim -10\%$  ( $\sim -7\%$ ) compared to mass estimate when we regard the BCG position as the center. This result implies that the BCG position is close to the true center of the cluster.

The center of ACTJ0022 was also investigated by other works. Reese et al. [82] carried out follow-up observations of ACTJ0022 with Sunyaev-Zel'dovich Array (SZA)<sup>1</sup>. Their deep, targeted observations provided higher signal-to-noise ratio SZE signals. The center of ACTJ0022 based on the SZ profile is R.A.=00:22:13.00, Dec.=−00:36:33.35 (J2000), which is fairly consistent with the position of the BCG. On the other hand, the ACT team reported the center of the ACTJ0022 is R.A.=00:22:13.44, Dec.=−00:36:25.20 (J2000)<sup>2</sup>. There is a discrepancy between our BCG position and the center of the SZ map reported by Reese et al. [82] as large as 0.45'. The positional uncertainty of the center provided by the ACT team is  $\sim 0.25'$ . This discrepancy should be investigated in the future. If the position provided by the ACT team is correct, ACTJ0022 is a disturbed cluster.

### 6.3.3 Projection Effect

The mass we estimated through WL does not consist of the mass of a cluster only. As we observe three-dimensional mass projected onto the lens plane, large scale structure is also included into our estimate, which contaminates the cluster mass.

We can include this effect by generalizing the  $\chi^2$  used for mass estimate (Eq. (5.36)) to use a covariance consisting of the variance of lensing shear and the covariance

<sup>1</sup><http://astro.uchicago.edu/sza/>

<sup>2</sup>Priv. comm. with Matthew Hilton.

due to the large scale structure which is equivalent to cosmic shear;

$$\chi^2(M_\Delta, c_\Delta) = \sum_{ij}^{N_{\text{bin}}} \frac{[g_{\text{NFW}, r_i} - g_{+, \text{data}, r_i}] [g_{\text{NFW}, r_j} - g_{+, \text{data}, r_j}]}{C_{ij}}, \quad (6.4)$$

$$C_{ij} = \sigma_{+, \text{data}, r_i}^2 \delta_{ij} + C_{ij}^{\text{lss}}, \quad (6.5)$$

where  $\delta_{ij}$  is Kronecker delta. By using Eq. (47) in Oguri and Takada [73], the covariance due to the large scale structure is written as

$$C_{ij}^{\text{lss}} = \int \frac{ldl}{2\pi} J_2(l\theta_i) J_2(l\theta_j) C^{\kappa\kappa}(l), \quad (6.6)$$

where  $J_2(l\theta_i)$  is the Bessel function, and  $C^{\kappa\kappa}(l)$  is the lensing shear power spectrum;

$$C^{\kappa\kappa}(l) = \int dw \left[ \frac{\bar{\rho}_m(z)}{(1+z)\Sigma_{cr}(z)} \right]^2 w^{-2} P_m^{\text{NL}} \left( k = \frac{l}{w}; z \right), \quad (6.7)$$

where  $w$  is the comoving distance and  $P_m^{\text{NL}}$  is the nonlinear matter spectrum. We use the fitting formula in [89] for computing  $P_m^{\text{NL}}$  as well as Oguri and Takada [73].

Minimizing the new  $\chi^2$ , we find that the projection effect changes the central value of mass by  $\sim +4\%$ , and increases the statistical error by  $\sim 3 - 4\%$ . As the statistical error due to shape noise is large, the influence induced by the projection effect is relatively small.

## 6.4 Comparison with Observation by Sunyaev-Zel'dovich Array

Reese et al. [82] who carried out deep observations of ACTJ0022 as described in Section 6.3.2 gave two kinds of mass estimate. The first one was a SZ-derived mass estimated as follows. They converted the observed SZ signals into spherically integrated Compton- $y$  parameter<sup>3</sup>, based on the universal pressure profile derived from 33 local ( $z < 0.2$ ) cluster X-ray observations provided by Arnaud et al. [7]. Using the virial theorem with surface pressure correction, they related the integrated Compton- $y$  parameter with mass (for details, see Mroczkowski [63]). They reported  $M_{500\rho_c}^{\text{SZ}} = 0.58 \pm 0.04 \times 10^{15} M_\odot$  and spherically integrated Compton- $y$  parameter within  $r_{500\rho_c}$ ,  $Y_{500\rho_c} = 0.80 \pm 0.11 \times 10^{-4} \text{ Mpc}^2$ .

The other estimate was an optically informed mass based on SDSS Stripe 82 data [2]. They first computed cluster richness  $N_{200}$  and the number of red sequence

<sup>3</sup>For the definition of Compton- $y$  parameter, see Appendix C.

<sup>4</sup> $M_{500\rho_c}^{\text{SZ}}$  and  $Y_{500\rho_c}$  presented here are different from what one may find at arXiv as of Dec. 20, 2012. E. Reese provided us these values in private communication.

galaxies in a cluster measured within  $r_{200}$ , following a prescription provided by Menanteau et al. [57]. The cluster richness was then translated into mass estimate  $M_{500\rho_c}^{N-M_{WL}}$  by using a scaling relation between the cluster richness and weak lensing mass that was provided by Rozo et al. [86]. The reported mass was  $M_{500\rho_c}^{N-M_{WL}} = 0.777 \pm 0.112 \times 10^{15} M_{\odot}$ .

To compare their result, we again performed a fit on the tangential shear signals to derive  $M_{500\rho_c}$  while leaving  $c_{500\rho_c}$  free. The result is  $M_{500\rho_c} = 0.78_{-0.29}^{+0.31} \times 10^{15} M_{\odot}$ . Although our WL mass agrees with  $M_{500\rho_c}^{SZ}$  within error bar, there is small discrepancy. On the other hand, our result agrees well with  $M_{500\rho_c}^{N-M_{WL}}$ , which is derived from scaling relation between cluster richness and WL mass.

The error of our mass estimate is much larger than that derived from SZ signals and optical information presented by Reese et al. [82]. This is due to the small number density of background galaxies used for deriving the WL signals,  $3.18 \text{ arcmin}^{-2}$ . To reduce the error, it is necessary to increase the number density  $N$ , since the error is dominated by shape noise which scales with  $N^{-1/2}$ . As discussed in Section 4.3.3, the shape measurement algorithm we used for this work, the EGL method, will bias shear estimate for galaxies with low signal-to-noise ratio. Thus we set the strict selection of the background galaxies,  $\nu > 20$ , where  $\nu$  is the signal-to-noise ratio defined by fitting results of the EGL method (Section 5.6.2). When we set a lower selection limit,  $\nu > 10$ , the number density is increased to  $4.99 \text{ arcmin}^{-2}$ . Thus even if we carry out a 4 times longer observation of our data or find a better shape measurement algorithm which can be applicable to galaxies whose  $\nu > 10$ , the error of mass estimate will be reduced by only factor of  $\sim 1.3$ . In this sense, the WL measurement of ACTJ0022 is statistically limited.

Systematic uncertainties from physics on the WL measurements can be estimated quantitatively as described in Section 6.3, and is found to be below the statistical uncertainty. On the other hand, systematic uncertainties of the SZ-derived mass is somewhat unpredictable since the physics in a cluster is complicated, and can be larger than statistical error. For example, at first Reese et al. [82] reported different SZ-derived mass,  $M_{500\rho_c}^{SZ} = 0.73 \pm 0.10 \times 10^{15} M_{\odot}$ , using the virial theorem *without* surface pressure correction. The difference of the assumption of dynamical equilibrium can yield such a bias, which is actually larger than statistical error. Among a series of cluster mass estimators such as SZ, X-ray, and velocity dispersion, only WL does not rely on dynamical equilibrium, suggesting it may be safer mass estimator.

## 6.5 Scaling Relation

Marrone et al. [53] reported scaling relation between WL mass and spherically-

integrated Compton- $y$  parameter, using observables of 18 galaxy clusters at  $z \sim 0.2^5$ , as shown in Fig. 6.1 as a cyan dashed line. Also data points used for deriving the scaling relation are plotted as cyan dots.

Marrone et al. [53] compared their scaling relation between integrated Compton- $y$  parameter and WL mass with other scaling relations. They first compared the scaling relation between integrated Compton- $y$  parameter and X-ray derived mass given by Andersson et al. [6], which is shown as a black dashed line in Fig. 6.1. Andersson et al. [6] selected a sample consisting of 15 clusters from the SZ observation of 178-deg<sup>2</sup> sky surveyed by the SPT, and conducted X-ray follow-up observations using Chandra and XMM-Newton. The sample has wide range of redshift from  $z \sim 0.3$  to  $z \sim 1$  with the mean redshift of 0.67. They estimated the spherically-integrated Compton- $y$  parameter using a density profile derived from their own X-ray observations and assuming universal temperature profile derived by Vikhlinin et al. [98]. Secondly, they compared the scaling relation between integrated Compton- $y$  parameter and mass, both of which are derived from X-ray observables [7], as shown in a black dotted line in Fig. 6.1, using same X-ray samples to derive the universal pressure profile used by Reese et al. [82] and Marrone et al. [53].

We added  $M_{500\rho_c}$  (our WL mass estimate) derived in Section 6.4, and  $M_{500\rho_c}^{SZ}$  and  $M_{500\rho_c}^{N-MWL}$  derived by Reese et al. [82] that are also described in Section 6.4. These error bars show their statistical errors. Our result is consistent with all the scaling relations. However, it is closer to the scaling relation derived by Andersson et al. [6] than that of Marrone et al. [53]. Since the error bar is large, we cannot make a strong statement. The main difference between Andersson et al. [6] and Marrone et al. [53] is that the former used high-redshift clusters while the latter used only low-redshift clusters. To test these scaling relations, more cluster samples in high-redshift are needed. Fortunately, among systematic errors due to physics described in 6.3, halo triaxiality and projection effect will be suppressed if a lot of clusters are used. Thus WL measurements are expected to give a robust scaling relation between SZ signals and cluster mass.

## 6.6 Cosmological Implications

### 6.6.1 Exclusion Curve

Finally we test the  $\Lambda$ CDM paradigm, using  $M$ - $z$  exclusion curve described in Section 2.2. As discussed in Section 2.2, we should correct for Eddington bias. Mortonson et al. [62] gave the equation to calculate the bias as

$$\Delta \ln M = \frac{\gamma}{2} \sigma_{\ln M}^2 \quad (6.8)$$

---

<sup>5</sup>They used same universal pressure profile as Reese et al. [82] used.

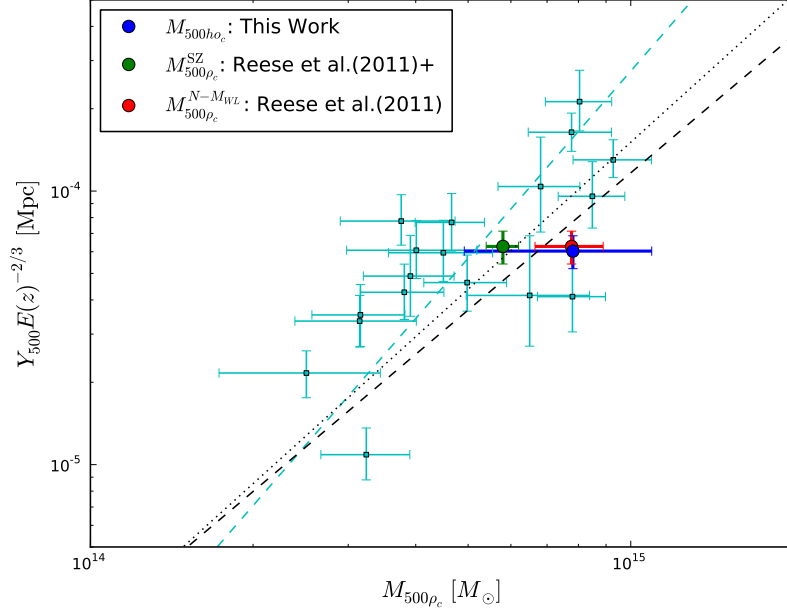


Figure 6.1: Scaling relations between cluster mass and integrated Compton- $y$  parameter. A cyan dashed line is the scaling relation derived by Marrone et al. [53]. Cyan dots show clusters used for deriving the scaling relation. A blue dot is ACTJ0022 whose WL mass is measured by this work and integrated Compton- $y$  parameter is taken from Reese et al. [82]. A green dot is again ACTJ0022 whose integrated Compton- $y$  parameter is same as the blue dot but mass is inferred from integrated Compton- $y$  parameter. A red dot is also ACTJ0022 whose integrated Compton- $y$  parameter is same as the blue dot but mass is inferred from scaling relation between cluster richness and weak lensing mass. The latter two dots are shifted by a factor of 1.04 from the blue dot. A black dashed line is the scaling relation between integrated Compton- $y$  parameter and mass derived from X-ray observables that is derived by using clusters selected by the SPT [6]. A black dotted line is the scaling relation between integrated Compton- $y$  parameter calculated from X-ray observables and mass also derived from X-ray observables [7].

where  $\gamma$  is the local logarithmic slope of the mass function  $dn/d\ln M \propto M^\gamma$ . To find  $\sigma_{\ln}^2 M$  for ACTJ0022, we estimated it as a half of the width of the  $\pm 1\sigma$  statistical error on the mass divided by the central value.  $\gamma$  is calculated from the fitting formula provided by Mortonson et al. [62]<sup>6</sup>. The bias-corrected mass  $M'$  is calculated by  $M' = \exp(1/2\gamma\sigma_{\ln M}^2)M$ . After the correction, the central mass value is reduced from  $0.72 \times 10^{15} M_\odot/h$  to  $0.47 \times 10^{15} M_\odot/h$  ( $0.82 \times 10^{15} M_\odot/h$  to  $0.30 \times 10^{15} M_\odot/h$ ) when the concentration parameter is free (fixed).

We plotted the mass and the exclusion curve for joint 95% CL with sky coverage of 200 deg<sup>2</sup> where ACTJ0022 is the brightest SZ source. To draw the curve, the fitting formula is used. Circle and diamond points denote the mass without and with the concentration parameter fixed, respectively, and red open and black solid points denote with and without Eddington bias correction. When Eddington bias is not corrected, the mass with the concentration parameter fixed exceeds the exclusion curve if we include the statistical error. However, after Eddington bias is corrected, the mass is well below the exclusion curve. Note that for the mass with fixed concentration parameter, Eddington bias correction is large since it has larger statistical error. Thus ACTJ0022 is consistent with the  $\Lambda$ CDM model and existing data sets.

## 6.6.2 Comparison with previous works

In addition to the test done by Mortonson et al. [62] as shown in Fig. 2.2 in Section 2.2, there have been three works which tested the  $\Lambda$ CDM with the exclusion curve. As discussed in Section 2.2, in order to test the  $\Lambda$ CDM with the exclusion curve, it is important that the survey region, or sky coverage, is well-defined. Another important point is to use an unbiased mass estimate. There are several observables to derive cluster mass such as X-ray, SZ, galaxy velocity dispersion, and WL. Among them, only WL does not need any dynamical assumption such as virial theorem and hydrostatic equilibrium, which enables us to estimate cluster mass including dark matter directly.

Williamson et al. [101] reported an SZ-selected sample of the most massive galaxy clusters in the 2500 deg<sup>2</sup> of the SPT survey. They derived mass of 26 clusters from SZ signals based on the scaling relation between SZ detection significance and mass determined by simulations. None of them exceeds the exclusion curve with the sky coverage of 2500 deg<sup>2</sup> for 95% joint CL. Note that in their work the survey region is well-defined.

Jee et al. [36] carried out WL measurements of 22 high-redshift galaxy clusters, as noted in Section 6.1. The most massive cluster in their sample, CL J1226+3332, exceeds the exclusion curve with the sky coverage of 100 deg<sup>2</sup> for 95% CL, and

---

<sup>6</sup>The code is available from <http://background.uchicago.edu/abundance/>.

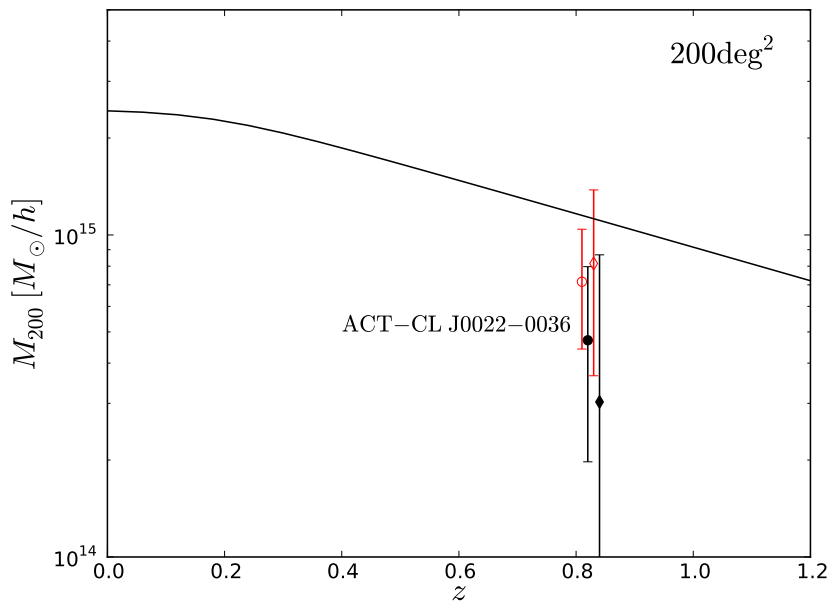


Figure 6.2:  $\Lambda$ CDM exclusion curve for joint 95% CL with sky coverage 200 deg<sup>2</sup> and the WL mass of ACTJ0022 which is measured by this work. Circle and diamond points denote the mass without and with the concentration parameter fixed, respectively, and red open and black solid points denote with and without Eddington bias correction. Each point is offset in redshift by 0.01 for clarity. The mass of ACTJ0022 is within the  $\Lambda$ CDM paradigm.

masses of other three massive clusters exceed the exclusion curve with the same sky coverage for 80% CL. However, they selected the clusters from different surveys, which means the sky coverage is not well-defined. In fact, when they compared the mass with the exclusion curve with 300 deg<sup>2</sup> sky coverage, none of them exceeded the exclusion curve for 95% CL, although two of them exceeded the curve for 80% CL.

Menanteau et al. [58] explored a high-redshift extremely massive cluster, ACT-CL J0102-4915 “El Gordo”, which was originally reported by Marriage et al. [52] as a particularly strong SZ detection at a frequency of 148 GHz with photometric redshift of 0.75. ACT-CL J0102-4915 was expected to be one of the most massive clusters in the survey area of 755 deg<sup>2</sup> that consists of 455 deg<sup>2</sup> of southern sky and 300 deg<sup>2</sup> along the equator observed by the ACT until 2009. Note that ACT-CL J0102-4915 is not reachable from the Subaru Telescope, as it is at southern sky. The cluster sample provided by the SPT described above [101] includes ACT-CL J0102-4915. They reported the cluster as the most significant detection on a 2500 deg<sup>2</sup> survey. They reported the mass  $M_{200} = (1.89 \pm 0.29(\text{stat.}) \pm 0.35(\text{syst.})) \times 10^{15} M_{\odot} h_{70}^{-1}$ , where  $h_{70}$  is defined as  $H_0 = 70h_{70} \text{ km s}^{-1} \text{ Mpc}^{-1}$ , and photometric redshift of 0.78. Menanteau et al. [58] carried out optical spectroscopy, which yielded spectroscopic redshift of 0.87. They also reported the cluster mass that is obtained by combining mass estimates which are inferred from velocity dispersion, x-ray observables, and SZ observables,  $M_{200} = (2.16 \pm 0.32) \times 10^{15} M_{\odot} h_{70}^{-1}$ . The spectroscopic redshift and cluster mass, which are higher than these originally used in Williamson et al. [101], gave a tension to the cluster when testing the  $\Lambda$ CDM with the exclusion curve. The cluster mass is almost at the exclusion curve with 2800 deg<sup>2</sup> (the combined survey area of the ACT and SPT region of which 455 deg<sup>2</sup> is observed by both the ACT and SPT). They concluded that this cluster is clearly rare but it is not massive or early enough to put significant pressure on the standard cosmological model.

Our work is unique in the following aspects. First, the survey region is already well-defined since ACTJ0022 is the most significant SZ source in 200 deg<sup>2</sup> equatorial region observed by the ACT. Second, the WL observable is used for mass estimation, which provides a direct cluster mass estimate. Hence, this work is the first  $\Lambda$ CDM exclusion test with an extreme massive cluster, which uses a well-defined survey region and direct mass estimate by WL.

# Chapter 7

## Conclusions

We carried out a WL mass measurement of the high-redshift cluster ACTJ0022, which was discovered by the SZ survey covering 200 deg<sup>2</sup> of the sky conducted by the ACT and has the highest SN in the survey region. We analyzed the data using the pipeline currently being developed for HSC, the next generation wide-field prime focus camera of the Subaru Telescope. For galaxy shape measurement, we used the EGL method, which models PSF and galaxies by two-dimensional basis functions to extract their shape information. Since this method adopts model fitting we can naturally extend the method to a multiple-exposure simultaneous fit, which enables us to check quality of exposures in terms of shape measurement. Photometric redshifts were used for clean separation of background galaxies. Systematic uncertainties were carefully investigated, and we obtained

$$M_{200} = (0.72^{+0.33(\text{stat.})}_{-0.27} +^{0.12(\text{syst.})}_{-0.06}) \times 10^{15} M_{\odot}/h. \quad (7.1)$$

This result agrees with the mass estimated from SZ signal [82], the mass estimated from the scaling relation between cluster richness and WL mass [82], and scaling relation between WL mass and SZ observables derived from 18 other clusters at low redshift ( $z = 0.15 - 0.3$ ) [53].

We tested the  $\Lambda$ CDM model with this high-redshift, massive cluster, using the framework provided by Mortonson et al. [62]. We compared the WL mass with the exclusion curve which requires cluster mass and redshift to rule out the  $\Lambda$ CDM at 95% CL. Clearly the observed mass is within the exclusion curve, and does not violate the  $\Lambda$ CDM model.

This study has proved that the WL mass measurements of high-redshift galaxy clusters is possible and provides the first step toward establishing the scaling relation between SZ signals and cluster mass at high redshift that can be used for improving cosmological constraints by combining the ACT/ACTPol and HSC. This combination will enable us to explore the universe up to high redshift of  $z \sim 0.8$  and trace the evolution of the universe from the beginning of cosmic acceleration

to the present. Since other surveys are not reachable to such a high redshift range, our study exemplifies the uniqueness of the combination of the ACT/ACTPol and HSC.

# Appendix A

## Hyper Suprime-Cam

Hyper Suprime Cam (HSC) is the next generation wide-field prime focus camera of the 8.2-m Subaru Telescope located at the summit of Mauna Kea. The HSC has a 1.5-degree-diameter field of view, which is 7 times larger than that of its predecessor Suprime-Cam[60]. To cover the large field of view, 116 pieces of 2k x 4k fully depleted CCDs are employed. The total number of pixels amounts to 1 Giga pixels. The unique capability of the Subaru Telescope such as photon collecting power, excellent image quality, and wide field of view at prime focus, enables the HSC to conduct wide, deep survey.

The cross section of the HSC is shown in Fig. A.1. The height of HSC is about 3 m. The light focused by 8-m primary mirror goes through wide field corrector [48], which consists of 7 lenses and placed in lens barrel shown as a red part in Fig. A.1, and a filter placed in between the last lens and focal plane. Filters are stored in the filter exchanger when they are not used. We plan to use 5 broad band filters and several narrow band filters. The broadband filters consist of  $g'$ ,  $r'$ ,  $i'$ ,  $z'$  from Sloan Digital Sky Survey system [30] and one more red band  $y$  at  $\sim 1\mu\text{m}$ .

Fig.A.2 shows the focal plane of the HSC. We employ 116 CCDs. Among these CCDs, 112 CCDs are used for scientific purpose<sup>1</sup>, while 4 CCDs are used for telescope guiding. The CCDs are manufactured by Hamamatsu Photonics K.K. [42] whose pixel size is 2k x 4k. Each CCD has 4 outputs. The CCD is fully depleted so that it has high sensitivity around longer wavelength; quantum efficiency of the CCD is about twice as that of CCDs formerly used in the Suprime-Cam manufactured by MIT/LL[42]. Thus the HSC can observe high redshift objects at high efficiency. The CCDs are placed in dewar and cooled down to -100 degrees Celsius to suppress dark count.

The electronics of the HSC are divided into two parts; Front-end Electronics (FEE), the analog part of the electronics, and Back-end Electronics (BEE), the

---

<sup>1</sup>Actually 8 CCDs out of the 112 CCDs are used for auto focus.

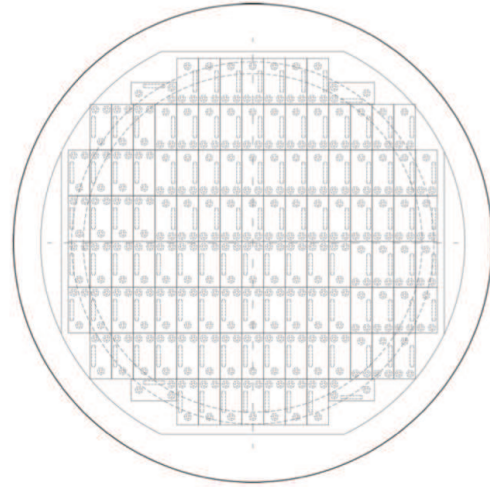
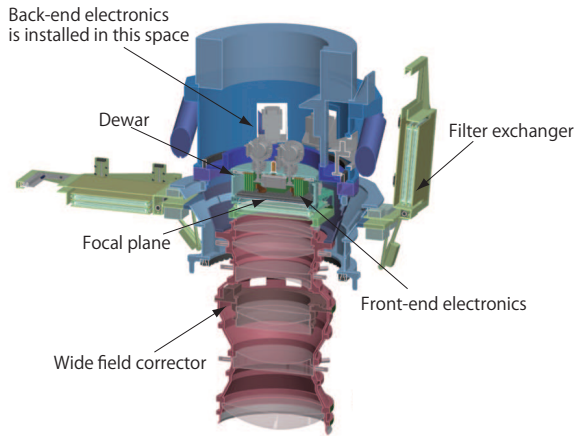


Figure A.1: Cross section of the HSC.

Figure A.2: Focal plane of the HSC.

Survey	Area [deg <sup>2</sup> ]	Depth [AB, $5\sigma$ , 2'']	Key Sciences
Wide	1500-2000	grizy ( $i \sim 25.8$ )	Cosmology, Clusters, QSOs
Deep	$\sim 30$	grizy+NBs ( $i \sim 27.2$ )	Galaxies, QSO/AGN, Clusters, SNe
Ultra-Deep	$\sim 2$ HSC FoVs	grizy ( $i \sim 28$ )	high-z galaxies (LAEs, LBGs), SNe

Table A.1: Survey layers of HSC.

analog part of the electronics. The FEE is placed in the dewar together with the CCDs. Analog signals from CCDs are digitized into 16-bit by the FEE. Then the BEE, which is placed outside of the dewar, receives the digital signals and sends them to data acquisition computer in a observation room via Gigabit Ethernet. The Electronics allow for reading out all the CCD within  $\sim 10$  seconds at fast readout operation mode.

The HSC is expected to see the first light at the beginning of 2012, and start its survey from 2013. The survey is divided into three layers; wide, deep, and ultra-deep, as summarized in Table A.1. From a viewpoint of cosmology, the wide layer enables us to carry out weak lensing survey with excellent image quality. Such a deep, wide data set is unique in the world, which allows for putting a constraint on the nature of dark energy with high precision through cosmic shear. In addition, the HSC plans to collaborate with ACT and its successive project ACTPol. This combination allows us to explore the nature of dark energy at high-redshift via cluster abundance.

# Appendix B

## Details of Elliptical Gauss-Laguerre Method

In this section, we give detail calculations of the EGL method, especially convolution of PSF and galaxy model:

$$I^{\text{model}}(\mathbf{x}) = \sum_{i,j} b_i^* b_j \left[ \psi_i^{\sigma^*} \otimes \psi_j^{\sigma_g E} \right] (\mathbf{x}). \quad (\text{B.1})$$

Since this convolution is performed in same coordinate to use relation,

$$\left[ \psi_i^{\sigma^*} \otimes \psi_j^{\sigma_g} \right] (\mathbf{x}) = \sum_k C_{ij}^k \psi_k^{\sigma^o} (\mathbf{x}), \quad (\text{B.2})$$

we conform the coordinate of  $\psi^{\sigma^*}(\mathbf{x})$  to that of  $\psi^{\sigma_g E}(\mathbf{x})$  (i.e.  $\psi^{\sigma_g}(\mathbf{E}^{-1}\mathbf{x})$ ):

$$\psi_i^{\sigma^*}(\mathbf{x}) = \sum_j E_{ij}^{-1} \psi_j^{\sigma^*}(\mathbf{E}^{-1}\mathbf{x}). \quad (\text{B.3})$$

The calculations of convolution matrix in Eq (B.2) are given in Section B.2 and those of transformation matrix in Eq. (B.3) are given in Section B.3 and Section B.4.

## B.1 Rising and Lowering Operator for Gauss-Laguerre Function

Since GLs are basis of two-dimensional harmonic oscillator, they have the following properties:

$$\begin{aligned}
a_p^\sigma &= \frac{1}{2} \left[ \frac{x-iy}{\sigma} + \sigma \left( \frac{\partial}{\partial x} - i \frac{\partial}{\partial y} \right) \right], & a_p^\sigma \psi_{pq}^\sigma &= \sqrt{p} \psi_{(p-1)q}^\sigma, \\
a_p^{\sigma\dagger} &= \frac{1}{2} \left[ \frac{x+iy}{\sigma} - \sigma \left( \frac{\partial}{\partial x} + i \frac{\partial}{\partial y} \right) \right], & a_p^{\sigma\dagger} \psi_{pq}^\sigma &= \sqrt{p+1} \psi_{(p+1)q}^\sigma, \\
a_q^\sigma &= \frac{1}{2} \left[ \frac{x+iy}{\sigma} + \sigma \left( \frac{\partial}{\partial x} + i \frac{\partial}{\partial y} \right) \right], & a_q^\sigma \psi_{pq}^\sigma &= \sqrt{q} \psi_{p(q-1)}^\sigma, \\
a_q^{\sigma\dagger} &= \frac{1}{2} \left[ \frac{x-iy}{\sigma} - \sigma \left( \frac{\partial}{\partial x} - i \frac{\partial}{\partial y} \right) \right], & a_q^{\sigma\dagger} \psi_{pq}^\sigma &= \sqrt{q+1} \psi_{p(q+1)}^\sigma.
\end{aligned} \tag{B.4}$$

## B.2 Convolution Matrix for Gauss Laguerre Function

The observed galaxy intensity  $I_o(\mathbf{x})$  is convolution of galaxy intrinsic intensity  $I_i(\mathbf{x})$  and PSF intensity  $I_\star(\mathbf{x})$ :

$$I_o(\mathbf{x}) = I_i(\mathbf{x}) \otimes I_\star(\mathbf{x}) = \int d^2x' I_i(\mathbf{x}') \otimes I_\star(\mathbf{x} - \mathbf{x}'). \tag{B.5}$$

If we perform Fourier transformation as

$$\tilde{I}(\mathbf{k}) = \frac{1}{2\pi} \int d^2x I(\mathbf{x}) e^{-i\mathbf{k}\cdot\mathbf{x}}, \tag{B.6}$$

$$I(\mathbf{x}) = \frac{1}{2\pi} \int d^2k \tilde{I}(\mathbf{k}) e^{i\mathbf{k}\cdot\mathbf{x}}, \tag{B.7}$$

the convolution of GLs

$$\psi_{p_i q_i}^{\sigma_i} \otimes \psi_{p_\star q_\star}^{\sigma_\star} = \sum C_{p_o q_o}^{p_i q_i p_\star q_\star} \psi_{p_o q_o}^{\sigma_o} \tag{B.8}$$

can be also written as

$$2\pi \tilde{\psi}_{p_i q_i}^{\sigma_i} \tilde{\psi}_{p_\star q_\star}^{\sigma_\star} = \sum C_{p_o q_o}^{p_i q_i p_\star q_\star} \tilde{\psi}_{p_o q_o}^{\sigma_o}. \tag{B.9}$$

In Fourier space, rising and lowering operator is defined such as

$$a_p^{\sigma\dagger} \tilde{\psi} = \frac{-i}{2} \left[ \sigma(k_x + ik_y) - \frac{1}{\sigma} \left( \frac{\partial}{\partial k_x} + i \frac{\partial}{\partial k_y} \right) \right] \tilde{\psi} \equiv \tilde{a}_p^{\sigma\dagger} \tilde{\psi}. \tag{B.10}$$

The rising operator  $\tilde{a}_q^{\sigma\dagger}$  is similarly obtained by changing  $\sigma \rightarrow 1/\sigma$  of  $a_q^{\sigma\dagger}$  and adding a factor of  $-i$  to it. Since Fourier transform of  $\psi_{00}^\sigma$  is written as

$$\tilde{\psi}_{00}^\sigma = \frac{1}{\sqrt{\pi}} e^{-k^2 \sigma^2 / 2}, \quad (\text{B.11})$$

we have

$$\tilde{\psi}_{pq}^\sigma(k, \phi) = \frac{(-i)^m}{\sqrt{\pi}} \sqrt{\frac{q!}{p!}} (k\sigma)^m e^{im\phi} e^{-k^2 \sigma^2 / 2} L_q^{(m)}(k^2 \sigma^2), \quad (\text{B.12})$$

Operating the raising factor, we can obtain

$$\sigma_o \tilde{a}_p^{\sigma_o\dagger} \tilde{I}_o = (\sigma_i \tilde{a}_p^{\sigma_i\dagger} \tilde{I}_i) \tilde{I}_\star + \tilde{I}_i (\sigma_\star \tilde{a}_p^{\sigma_\star\dagger} \tilde{I}_\star) \quad (\text{B.13})$$

under the condition of  $\sigma_o^2 = \sigma_i^2 + \sigma_\star^2$ . Therefore the recursion relation for the coefficient  $C_{p_o q_o}^{p_i q_i p_\star q_\star}$  can be written as

$$\sigma_\star \sqrt{p_\star + 1} C_{p_o q_o}^{p_i q_i (p_\star+1) q_\star} = \sigma_o \sqrt{p_o} C_{(p_o-1) q_o}^{p_i q_i p_\star q_\star} - \sigma_i \sqrt{p_i + 1} C_{p_o q_o}^{(p_i+1) q_i p_\star q_\star}. \quad (\text{B.14})$$

The equivalent recursion relation in the case of the lower operator is

$$\sigma_o \sqrt{p_o + 1} C_{(p_o+1) q_o}^{p_i q_i p_\star q_\star} = \sigma_i \sqrt{p_i} C_{p_o q_o}^{(p_i-1) q_i p_\star q_\star} + \sigma_\star \sqrt{p_\star} C_{p_o q_o}^{p_i q_i (p_\star-1) q_\star}. \quad (\text{B.15})$$

The corresponding recursion relation for  $q$  is written by replacing  $p$  with  $q$  in above two equations. Since these recursion relations of  $p$  are independent with these of  $q$ , and *vice versa*, we can divide the components of the tensor  $C$  into the  $p$ - and  $q$ -factor:

$$C_{p_o q_o}^{p_i q_i p_\star q_\star} = 2\sqrt{\pi} f(p_o, p_i, p_\star) f(q_o, q_i, q_\star). \quad (\text{B.16})$$

Once we know  $C_{00}^{p_i q_i p_\star q_\star}$ , all the components of  $C$  can be derived by using Eq. (B.15). From Eq. (B.14)

$$\begin{aligned} f(0, p_i, p_\star) &= -\frac{\sigma_i}{\sigma_\star} \sqrt{\frac{p_i + 1}{p_\star}} f(0, p_i + 1, p_\star - 1) = \dots \\ &= \sqrt{\frac{(p_i + p_\star)!}{p_i! p_\star!}} \left(-\frac{\sigma_i}{\sigma_\star}\right)^{p_\star} f(0, p_i + p_\star, 0) \end{aligned} \quad (\text{B.17})$$

On the other hand, the direct calculation of  $k$ -space Laguerre functions yields

$$2\pi \tilde{\psi}_{p_i q_i}^{\sigma_i} \tilde{\psi}_{00}^{\sigma_\star} = 2\sqrt{\pi} \sum_{p_o=0}^{p_i} \sum_{q_o=0}^{q_i} \sqrt{\frac{p_i! q_i!}{p_o! q_o!}} \times \frac{D^{(p_o+q_o)/2} (1-D)^{q_i-q_o}}{(q_i - q_o)!} \tilde{\psi}_{p_o q_o}^{\sigma_o}, \quad (\text{B.18})$$

where the sum runs under the condition that  $p_o - q_o = m_i$ , and  $D \equiv \sigma_i^2/\sigma_0^2$ . Here we make use of the property of Laguerre polynomial

$$L_q^{(m)}(\alpha x) = \sum_{k=0}^q \binom{q+m}{q-k} \alpha^k (a-\alpha)^{q-k} L_k^{(m)}(x). \quad (\text{B.19})$$

The component of  $C$  whose  $p_\star$  and  $q_\star$  are both zero can be expressed as

$$C_{p_o q_o}^{p_i q_i 00} = 2\sqrt{\pi} \sqrt{\binom{p_i}{p_o} \binom{q_i}{q_o}} D^{(p_o+q_o)/2} \times (1-D)^{(p_i-p_o+q_i-q_o)/2} \quad (\text{B.20})$$

$$\Rightarrow f(p_o, p_i, 0) = \sqrt{\binom{p_i}{p_o}} D^{p_o/2} \times (1-D)^{(p_i-p_o)/2} \quad (\text{B.21})$$

$$\Rightarrow f(0, p_i, 0) = (1-D)^{p_i/2}. \quad (\text{B.22})$$

Therefore Eq. (B.17) becomes

$$f(0, p_i, p_\star) = (-1)^{p_\star} \sqrt{\frac{(p_i+p_\star)!}{p_i! p_\star!}} D^{p_\star/2} (1-D)^{p_i/2}. \quad (\text{B.23})$$

Hence all the components of the tensor  $C$  are summarized as

$$C_{p_o q_o}^{p_i q_i p_\star q_\star} = 2\sqrt{\pi} f(p_o, p_i, p_\star) f(q_o, q_i, q_\star) \quad (\text{B.24})$$

$$\begin{aligned} f(p_o+1, p_i, p_\star) &= \sqrt{D} \sqrt{\frac{p_i}{p_o+1}} f(p_o, p_i-1, p_\star) \\ &\quad + \sqrt{1-D} \sqrt{\frac{p_\star}{p_o+1}} f(p_o, p_i, p_\star-1) \end{aligned} \quad (\text{B.25})$$

$$f(0, p_i, p_\star) = (-1)^{p_\star} \sqrt{\frac{(p_i+p_\star)!}{p_i! p_\star!}} (1-D)^{p_i/2} D^{p_\star/2}. \quad (\text{B.26})$$

Furthermore, in the phase of implementation, we used the following recursion relation derived from Eq. (B.26) in order to avoid overflow due to factorial calculation:

$$f(0, p_i, p_\star) = -\sqrt{D} \sqrt{\frac{p_i+p_\star}{p_\star}} f(0, p_i, p_\star-1). \quad (\text{B.27})$$

### B.3 Transformation Matrices

In general, we define a transformation  $\mathbf{E}$  on the image by

$$\mathbf{E}I(\mathbf{x}) \equiv I(\mathbf{E}^{-1}\mathbf{x}). \quad (\text{B.28})$$

Given an original image  $I(\mathbf{x}) = \sum b_{pq} \psi_{pq}^\sigma(\mathbf{x})$ , the transformed image can be represented as

$$\mathbf{E}I(\mathbf{x}) = \sum b'_{pq} \psi_{pq}^\sigma(\mathbf{x}). \quad (\text{B.29})$$

We can express  $\mathbf{E}$  as a matrix operation on  $\mathbf{b}$ :

$$\mathbf{b}' = \mathbf{E}\mathbf{b}, \quad (\text{B.30})$$

$$b'_{p'q'} = \sum_{pq} E_{p'q'}^{pq} b_{pq}. \quad (\text{B.31})$$

Using this expression,

$$\mathbf{E}I = \sum_{pq} b'_{pq} \psi_{pq}^\sigma = \sum_{pq} E_{p'q'}^{pq} b_{pq} \psi_{p'q'}^\sigma, \quad (\text{B.32})$$

$$\Rightarrow \mathbf{E}\psi_{pq} = \sum_{p'q'} E_{p'q'}^{pq} \psi_{p'q'}^\sigma. \quad (\text{B.33})$$

Each element of the transformation matrix is written as

$$E_{p'q'}^{pq} = \sigma^2 \int d^2x (\mathbf{E}\psi_{pq}^\sigma) \bar{\psi}_{p'q'}^\sigma. \quad (\text{B.34})$$

Next we introduce transformed raising and lowering operators. For a rising operator for the original eigenfunctions,

$$\begin{aligned} \mathbf{E}(a_p^{\sigma\dagger} \psi_{pq}) &= \mathbf{E}(\sqrt{p+1} \psi_{p+1,q}) \\ &= \sqrt{p+1} \sum_{p'q'} E_{p'q'}^{p+1,q} \psi_{p'q'}^\sigma \\ &\equiv \hat{a}_p^{\sigma\dagger} \sum_{p'q'} E_{p'q'}^{p,q} \psi_{p'q'}^\sigma \\ &= \hat{a}_p^{\sigma\dagger} (\mathbf{E}\psi_{pq}). \end{aligned} \quad (\text{B.35})$$

Thus, the transformed raising and lowering operators are defined as

$$\hat{a}_p^\sigma (\mathbf{E}\psi_{pq}) = \mathbf{E}(a_p^\sigma \psi_{pq}), \quad (\text{B.36})$$

$$\hat{a}_p^{\sigma\dagger} (\mathbf{E}\psi_{pq}) = \mathbf{E}(a_p^{\sigma\dagger} \psi_{pq}), \quad (\text{B.37})$$

$$\hat{a}_q^\sigma (\mathbf{E}\psi_{pq}) = \mathbf{E}(a_q^\sigma \psi_{pq}), \quad (\text{B.38})$$

$$\hat{a}_q^{\sigma\dagger} (\mathbf{E}\psi_{pq}) = \mathbf{E}(a_q^{\sigma\dagger} \psi_{pq}). \quad (\text{B.39})$$

In the EGL method, we use two transformation matrices which describe dilation ( $\mathbf{D}_\mu$ ) and shear ( $\mathbf{S}_{\eta,\beta}$ ). Note that we do not need translation for making use of the convolution matrix derived in Section B.2.

## B.4 Formulae of Transformation Matrices

### B.4.1 Dilution

The dilution operation is defined by

$$\mathbf{D}_\mu I(x, y) = I(e^{-\mu}x, e^{-\mu}y). \quad (\text{B.40})$$

We derive recursion relations of  $\mathbf{D}_\mu$ . First we represent diluted raising and lowering operators by original raising and lowering operators. For example, in the case of diluted lowering operator for  $p$ ,

$$\begin{aligned} \hat{a}_p^\sigma(\mathbf{D}_\mu I) &= \mathbf{D}_\mu(a_p^\sigma I) \\ &= \mathbf{D}_\mu\left(\frac{1}{2}\left[\frac{x-iy}{\sigma} + \sigma\left(\frac{\partial}{\partial x} - i\frac{\partial}{\partial y}\right)\right]I(x, y)\right) \\ &= \frac{1}{2}\left[e^{-\mu}\frac{x-iy}{\sigma} + e^\mu\sigma\left(\frac{\partial}{\partial x} - i\frac{\partial}{\partial y}\right)\right]I(e^{-\mu}x, e^{-\mu}y) \\ &= \frac{1}{2}\left[e^{-\mu}(a_p^\sigma + a_q^{\sigma\dagger}) + e^\mu(a_p^\sigma - a_q^{\sigma\dagger})\right]I(e^{-\mu}x, e^{-\mu}y) \end{aligned} \quad (\text{B.41})$$

$$\Rightarrow \hat{a}_p^\sigma = \cosh \mu a_p^\sigma - \sinh \mu a_q^{\sigma\dagger}. \quad (\text{B.42})$$

By similar calculations, we get the corresponding relation for  $q$  as

$$\hat{a}_q^\sigma = -\sinh \mu a_p^{\sigma\dagger} + \cosh \mu a_q^\sigma. \quad (\text{B.43})$$

Next, we derive recursion relations of  $\mathbf{D}_\mu$  by applying these equations to Eq. (B.33):

$$\sqrt{p}D_{p'q'}^{(p-1)q} = \cosh \mu \sqrt{p'+1}D_{(p'+1)q'}^{pq} - \sinh \mu \sqrt{q'}D_{p'(q'-1)}^{pq}, \quad (\text{B.44})$$

$$\sqrt{q}D_{p'q'}^{p(q-1)} = -\sinh \mu \sqrt{p'}D_{(p'-1)q'}^{pq} + \cosh \mu \sqrt{q'+1}D_{p'(q'+1)}^{pq}. \quad (\text{B.45})$$

Substituting  $q' = 0$  to Eq. (B.44), we get

$$D_{p'0}^{pq} = \frac{1}{\sqrt{p'}} \operatorname{sech} \mu \sqrt{p} D_{(p'-1)0}^{(p-1)q}. \quad (\text{B.46})$$

From Eq. (B.45)

$$D_{p'q'}^{pq} = \frac{1}{\sqrt{q'}} \left( \operatorname{sech} \mu \sqrt{q} D_{p'(q'-1)}^{p(q-1)} + \tanh \mu \sqrt{p'} D_{(p'-1)(q'-1)}^{pq} \right). \quad (\text{B.47})$$

We can calculate all the elements of  $\mathbf{D}_\mu$  from the recursion relations (Eq. (B.46) and Eq. (B.47)) if  $D_{00}^{pq}$  is known, which can be directly calculated by using Eq. (B.34):

$$\begin{aligned}
D_{00}^{pq} &= \sigma^2 \int d^2x (\mathbf{D}_\mu \psi_{pq}^\sigma) \bar{\psi}_{00}^\sigma \\
&= \sigma^2 \int d^2x \left( \frac{(-1)^q}{\sqrt{\pi}\sigma^2} \sqrt{\frac{q!}{p!}} \left( \frac{ze^{-\mu}}{\sigma} \right)^m e^{-\frac{x^2+y^2}{2\sigma^2}} e^{-2\mu} L_q^{(m)} \left( \frac{r^2 e^{-2\mu}}{\sigma^2} \right) \right) \\
&\quad \times \left( \frac{1}{\sqrt{\pi}\sigma^2} e^{-\frac{x^2+y^2}{2\sigma^2}} \right) \\
&= \sigma^2 \int d^2x \left( \frac{(-1)^q}{\sqrt{\pi}\sigma^2} \sqrt{\frac{q!}{p!}} e^{-m\mu} \left( \frac{z}{\sigma} \sqrt{\frac{e^{-2\mu}+1}{2}} \right)^m \left( \frac{e^{-2\mu}+1}{2} \right)^{-m/2} \right. \\
&\quad \left. e^{-\frac{x^2+y^2}{2\sigma^2} \times \frac{e^{-2\mu}+1}{2}} \sum_{k=0}^q \binom{q+m}{q-k} \left( \frac{2}{e^{2\mu}+1} \right)^k \left( 1 - \frac{2}{e^{2\mu}+1} \right)^{q-k} \right. \\
&\quad \left. L_k^{(m)} \left( \frac{r^2}{\sigma^2} \times \frac{e^{-2\mu}+1}{2} \right) \right) \left( \frac{1}{\sqrt{\pi}\sigma^2} e^{-\frac{x^2+y^2}{2\sigma^2} \times \frac{e^{-2\mu}+1}{2}} \right) \\
&= (-1)^q \sigma^2 \sqrt{\frac{q!}{p!}} e^{-m\mu} \left( \frac{e^{-2\mu}+1}{2} \right)^{-(m+2)/2} \sum_{k=0}^q \binom{q+m}{q-k} \left( \frac{2}{e^{2\mu}+1} \right)^k \\
&\quad \left( \frac{e^{2\mu}-1}{e^{2\mu}+1} \right)^{q-k} \sqrt{\frac{(m+k)!}{k!}} \int d^2x' \psi_{00}^\sigma(\mathbf{x}') \bar{\psi}_{(m+k)k}^\sigma(\mathbf{x}') \\
&= e^\mu \operatorname{sech} \mu (-\tanh \mu)^q \delta_{pq}, \tag{B.48}
\end{aligned}$$

where  $\mathbf{x}' = \sqrt{\frac{e^{-2\mu}+1}{2}} \mathbf{x}$  and we use Eq. (B.19).

## B.4.2 Shear

The shear transformation matrix can be divided into a shear oriented on the  $x$ -axis and two rotations

$$\mathbf{S}_{\eta,\beta} = \mathbf{R}_\beta \mathbf{S}_\eta \mathbf{R}_{-\beta}. \tag{B.49}$$

We calculate matrix  $\mathbf{S}_\eta$  and  $\mathbf{B}_\beta$  respectively in the following sections.

### Shear Oriented along the $x$ -axis

The shear oriented on the  $x$ -axis gives

$$\mathbf{S}_\eta I(x, y) = I(e^{-\eta/2}x, e^{\eta/2}y), \tag{B.50}$$

where  $\eta$  is parametrized as  $\eta = 2 \tanh^{-1}(g)$  ( $g$  is defined in Section 4.1.2). First we represent sheared lowering operators by original operators in the same way as

dilution. In the case of  $a_p^\sigma$ , the calculation is like

$$\hat{a}_p^\sigma(\mathbf{S}_\eta I) = \mathbf{S}_\eta(a_p^\sigma I) \quad (\text{B.51})$$

$$\begin{aligned} &= \frac{1}{2} \left[ \frac{e^{-\eta/2}x - e^{\eta/2}iy}{\sigma} + \sigma \left( e^{\eta/2} \frac{\partial}{\partial x} - e^{-\eta/2}i \frac{\partial}{\partial y} \right) \right] I(e^{-\eta/2}x, e^{\eta/2}y) \\ &= \frac{1}{2} \left[ e^{-\eta/2}(a_p^{\sigma\dagger} + a_p^\sigma) - e^{\eta/2}(a_p^{\sigma\dagger} - a_p^\sigma) \right] I(e^{-\eta/2}x, e^{\eta/2}y), \end{aligned}$$

$$\Rightarrow \hat{a}_p^\sigma = -\sinh(\eta/2)a_p^{\sigma\dagger} + \cosh(\eta/2)a_p^\sigma, \quad (\text{B.52})$$

Applying this equations to the definition of a transformation matrix (Eq. (B.33)), we obtain

$$\sqrt{p}S_{p'q'}^{(p-1)q} = -\sinh(\eta/2)\sqrt{p'}S_{(p'-1)q'}^{pq} + \cosh(\eta/2)\sqrt{p'+1}S_{(p'+1)q'}^{pq}. \quad (\text{B.53})$$

The recursion relation for  $q$  is obtained by replacing  $p$  of above equation with  $q$ . Noting that the recursion relation for  $p$  can be represented only using  $p-$  operators, which is also the case for that for  $q$ , and both of the recursion relations have the same form, a matrix element can be divided in  $p-$ dependent and  $q-$ dependent parts such as

$$S_{p'q'}^{pq} = f(p, p')f(q, q'). \quad (\text{B.54})$$

Hence Eq. (B.53) can be written as

$$f(p, p') = \frac{1}{\sqrt{p'}} \left[ \text{sech}(\eta/2)\sqrt{p}f(p-1, p'-1) + \tanh(\eta/2)\sqrt{p'-1}f(p, p'-2) \right]. \quad (\text{B.55})$$

The corresponding relation for  $q$  is expressed by replacing  $p$  with  $q$ . Using Eq. (B.55), we can derive all  $f(p, p')$  if  $f(p, 0)$  is known. Here direct calculation of  $S_{00}^{p0}$  gives

$$\begin{aligned} S_{00}^{p0} &= \sigma^2 \int d^2x (\mathbf{S}_\eta \psi_{p0}^\sigma) \bar{\psi}_{00}^\sigma \\ &= \sigma^2 \int d^2x \left( \frac{1}{\sqrt{\pi}\sigma^2} \sqrt{\frac{1}{p!}} \left( \frac{e^{-\eta/2}x + ie^{\eta/2}y}{\sigma} \right)^p e^{-\frac{\epsilon^{-\eta}x^2 + \epsilon^{\eta}y^2}{2\sigma^2}} L_0^{(p)} \left( \frac{x^2 e^{-\eta} + y^2 e^{\eta}}{\sigma^2} \right) \right) \\ &\quad \times \left( \frac{1}{\sqrt{\pi}\sigma^2} e^{-\frac{x^2 + y^2}{2\sigma^2}} \right). \end{aligned} \quad (\text{B.56})$$

Next putting  $a = \frac{e^{-\eta}+1}{2\sigma^2}$  and  $b = \frac{e^{\eta}+1}{2\sigma^2}$ , and making use of

$$\int x^m e^{-ax^2} dx = \frac{1}{2} (1 + (-1)^m) a^{\frac{1}{2} - \frac{m}{2}} \Gamma\left(\frac{m-1}{2}\right), \quad (\text{B.57})$$

where  $a > 0$  and  $m$  is an integer,  $S_{00}^{p0}$  becomes

$$\begin{aligned}
S_{00}^{p0} &= \frac{1}{\pi\sigma^{p+2}\sqrt{p!}} \int d^2x \sum_{k=0}^p \binom{p}{k} (e^{-\eta/2}x)^{p-k} (ie^{\eta/2}y)^k e^{-(ax^2+by^2)} \\
&= \frac{1}{\pi\sigma^{p+2}\sqrt{p!}} \sum_{k=0}^p \binom{p}{k} i^k e^{-\eta(p-k)/2} e^{\eta k/2} \\
&\quad \times \frac{1}{2} (1 + (-1)^{(p-k)}) a^{-\frac{1}{2} - \frac{p-k}{2}} \Gamma\left(\frac{p-k-1}{2}\right) \\
&\quad \times \frac{1}{2} (1 + (-1)^k) b^{-\frac{1}{2} - \frac{k}{2}} \Gamma\left(\frac{k-1}{2}\right). \tag{B.58}
\end{aligned}$$

This calculation shows if  $p-k$  and  $k$  is even  $S_{00}^{p0}$  is non-zero, and otherwise  $S_{00}^{p0}$  is zero. In other words, if  $p$  is even  $S_{00}^{p0}$  is non-zero and if  $p$  is odd  $S_{00}^{p0}$  is zero. The following calculation is in the case of  $p$  is even.

$$\begin{aligned}
S_{00}^{p0} &= \frac{2^{p/2}}{\sqrt{p!}} \operatorname{sech}\left(\frac{\eta}{2}\right) \sum_{k=0, \text{even}}^p \binom{p}{k} \left(\frac{p-k-1}{2}\right)! \left(\frac{k-1}{2}\right)! \\
&\quad i^k (e^\eta + 1)^{-\frac{p-k}{2}} (e^{-\eta} + 1)^{-\frac{k}{2}} \\
&= \frac{(p-1)!!}{\sqrt{p!}} \operatorname{sech}\left(\frac{\eta}{2}\right) \sum_{k/2=0}^{p/2} \binom{p/2}{k/2} \left(\frac{1}{e^\eta + 1}\right)^{\frac{p}{2} - \frac{k}{2}} \left(-\frac{1}{e^{-\eta} + 1}\right)^{\frac{k}{2}} \\
&= \frac{\sqrt{p!}}{(p/2)!} \operatorname{sech}\left(\frac{\eta}{2}\right) \left(-\frac{\tanh(\eta/2)}{2}\right)^{p/2}. \tag{B.59}
\end{aligned}$$

From the fact that  $S_{00}^{p0} = f(p, 0)f(0, 0)$  and the symmetry between  $p$  and  $q$ , we get

$$f(p, 0) = \frac{\sqrt{p!}}{(p/2)!} \sqrt{\operatorname{sech}\left(\frac{\eta}{2}\right)} \left(-\frac{\tanh(\eta/2)}{2}\right)^{p/2}. \tag{B.60}$$

## Rotation

We define an anti-clockwise rotation as

$$\mathbf{R}_\beta I(x, y) = I(\cos \beta x - \sin \beta y, \sin \beta x + \cos \beta y). \tag{B.61}$$

We represent rotated lowering operators by original operators.

$$\begin{aligned}
\hat{a}_p^{\sigma\dagger}(\mathbf{R}_\beta I) &= \mathbf{R}_\beta(a_p^{\sigma\dagger} I) \\
&= \frac{1}{2} \left[ \frac{(\cos \beta x - \sin \beta y) + i(\sin \beta x + \cos \beta y)}{\sigma} \right. \\
&\quad \left. - \sigma \left( \left( \cos \beta \frac{\partial}{\partial x} - \sin \beta \frac{\partial}{\partial y} \right) + i \left( \sin \beta \frac{\partial}{\partial x} + \cos \beta \frac{\partial}{\partial y} \right) \right) \right] \\
&\quad \times I(\cos \beta x - \sin \beta y, \sin \beta x + \cos \beta y) \\
&= e^{i\beta} a_p^{\sigma\dagger} I(\cos \beta x - \sin \beta y, \sin \beta x + \cos \beta y) \\
\Rightarrow \hat{a}_p^{\sigma\dagger} &= e^{i\beta} a_p^{\sigma\dagger} \tag{B.62}
\end{aligned}$$

Applying this equations to the definition of a transformation matrix (Eq. (B.33)), we obtain

$$\sqrt{p+1} R_{(p'+1)q'}^{(p+1)q} = \sqrt{p'+1} e^{i\beta} R_{p'q'}^{pq}. \tag{B.63}$$

The corresponding equation for  $q$  is

$$\sqrt{q+1} R_{p'(q'+1)}^{p(q+1)} = \sqrt{q'+1} e^{-i\beta} R_{p'q'}^{pq}. \tag{B.64}$$

From the fact that

$$\begin{aligned}
R_{00}^{00} &= \sigma^2 \int d^2 x (\mathbf{R}_\beta \psi_{00}^\sigma) \bar{\psi}_{00}^\sigma \\
&= \sigma^2 \int d^2 x \psi_{00}^\sigma \bar{\psi}_{00}^\sigma = 1, \tag{B.65}
\end{aligned}$$

and

$$\begin{aligned}
R_{00}^{p0} &= \sigma^2 \int d^2 x (\mathbf{R}_\beta \psi_{p0}^\sigma) \bar{\psi}_{00}^\sigma \\
&= \sigma^2 e^{ip\beta} \int d^2 x \psi_{p0}^\sigma \bar{\psi}_{00}^\sigma = 0, \tag{B.66}
\end{aligned}$$

$$R_{p'0}^{00} = R_{00}^{0q} = R_{0q'}^{00} = 0, \tag{B.67}$$

we obtain

$$R_{p'q'}^{pq} = e^{i(p-q)\beta} \delta_{pp'} \delta_{qq'}. \tag{B.68}$$

## Shear

From Eq.(B.49) we obtain the matrix of shear transformation as

$$\begin{aligned}
(\mathbf{S}_{\eta,\beta})_{p'q'}^{pq} &= (\mathbf{R}_\beta \mathbf{S}_\eta \mathbf{R}_{-\beta})_{p'q'}^{pq} \\
&= S_{p'q'}^{pq} e^{i(p-q-p'+q')\beta}. \tag{B.69}
\end{aligned}$$

# Appendix C

## Sunyaev-Zel'dovich Effect

### C.1 What is the Sunyaev-Zel'dovich Effect?

Hot gas in a cluster can be observed through its effect on CMB. A CMB photon gains energy by inverse Compton scattering with energetic electrons in the hot gas. As a result, the CMB photon is slightly blue-shifted which is observed as the tiny temperature difference from CMB temperature,  $T_{\text{CMB}} = 2.725$  K. This effect is called thermal SZ effect. As shown in Fig. C.2, the thermal SZ effect causes a decrease in the CMB intensity at frequencies  $\lesssim 218$  GHz and an increase at higher frequencies.

Using dimensionless frequency  $x \equiv hv/k_bT_{\text{CMB}}$ , the spectral distortion is expressed as temperature difference;

$$\frac{\Delta T}{T_{\text{CMB}}} = f(x)y = f(x) \int \frac{k_B T_e}{m_e c^2} n_e \sigma_T c dt, \quad (\text{C.1})$$

where  $y$  is called Compton- $y$  parameter where the integral is carried out along the line of sight.  $T_e$ ,  $m_e$ , and  $n_e$  is temperature, mass, and density of electron in the

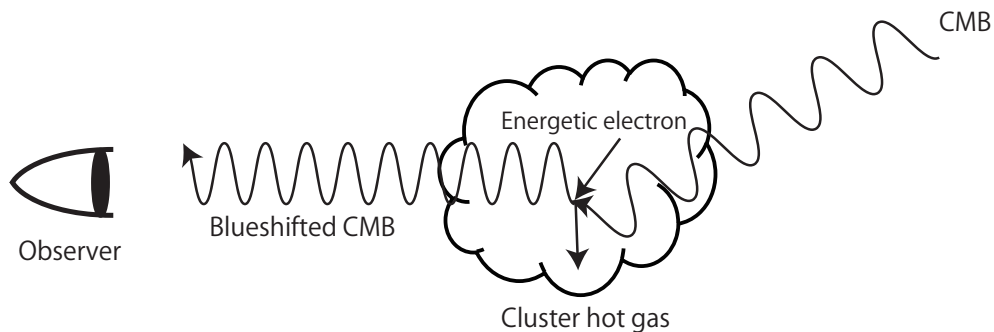


Figure C.1: Schematic of thermal SZ effect.

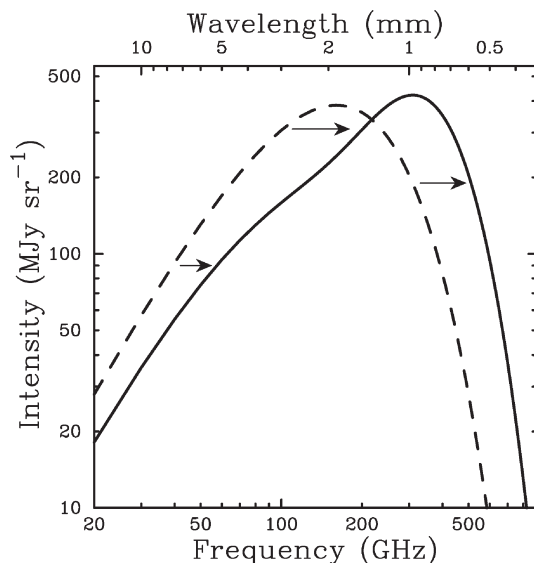


Figure C.2: CMB spectrum of original (dashed line) and distorted by SZ effect (solid line). This figure is taken from Carlstrom et al. [20].

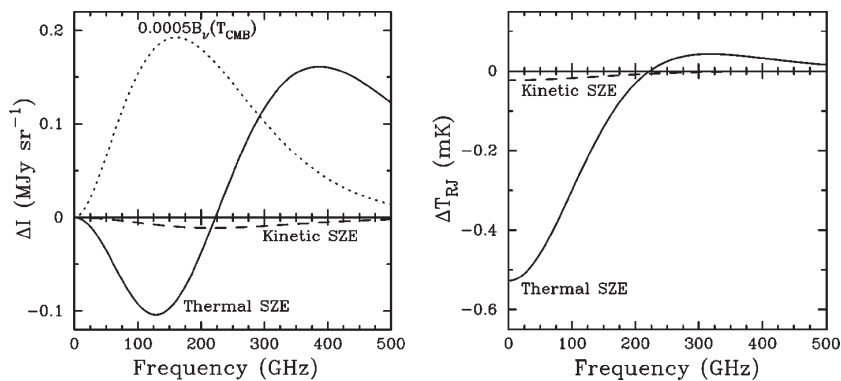


Figure C.3: Spectral distortion of CMB radiation due to SZ effect. The left panel shows intensity and the right panel shows temperature. Thick solid line shows thermal SZ effect and dashed line shows kinetic SZ effect. For reference thermal spectrum of CMB scaled by 0.0005 is shown by the dotted line in the left panel. The assumed cluster properties are an electron temperature of 10 keV, a Compton- $y$  parameter of  $10^{-4}$ , and a peculiar velocity of 500 km/s. This figure is taken from Carlstrom et al. [20].

hot gas.  $\sigma_T$  is cross section of Thomson scattering. The spectral dependence of the thermal SZ effect is

$$f(x) = \left[ x \frac{e^x + 1}{e^x - 1} - 4 \right] (1 + \delta_{\text{SZE}}(x, T_e)), \quad (\text{C.2})$$

where  $\delta_{\text{SZE}}(x, T_e)$  is the relativistic correction. Note that at  $\nu = 218$  GHz Eq. (C.2) becomes zero. In terms of intensity difference, the spectral distortion is written as

$$\Delta I_{\text{SZE}} = g(x) I_0 y, \quad (\text{C.3})$$

where  $I_0 = 2(k_B T_{\text{CMB}})^2 / (hc)^2$  and

$$g(x) = \frac{x^4 e^x}{(e^x - 1)^2} \left[ x \frac{e^x + 1}{e^x - 1} - 4 \right] (1 + \delta_{\text{SZE}}(x, T_e)). \quad (\text{C.4})$$

Again, at  $\nu = 218$  GHz Eq. (C.4) becomes zero. When observers use interferometer, thermal SZ effect is observed as intensity difference. On the other hand, temperature difference can be observed through bolometer. The Compton- $y$  parameter is often used as SZ observable.

It is worth noting that the thermal SZ effect does not depend on redshift, as shown in Eq. (C.2) and Eq. (C.4), which means that potentially clusters can be observed regardless of its redshift. This unique feature makes it possible to investigate high-redshift universe.

Another effect from hot gas of a cluster is called kinetic SZ effect, which is caused by bulk motion of a cluster with respect to the CMB rest frame. In nonrelativistic limit the spectral signature of the kinetic SZ effect is written as

$$\frac{\Delta T}{T_{\text{CMB}}} \sim \tau_T \frac{v}{c}, \quad (\text{C.5})$$

where  $\tau_t = \int n_e \sigma_T dl$  is optical depth and  $v$  is the cluster velocity along the line of sight.

A typical spectral distortion due to the thermal and kinetic SZ effect is shown in Fig. C.3. The temperature difference is as small as  $\sim 0.1$  mK, and the kinetic SZ effect is  $\sim 10$  times smaller than the thermal SZ effect.

To compare with other cluster observables such as WL mass, X-ray, and velocity dispersion, spherically integrated Compton- $y$  parameter is often used, which can be written as

$$Y_{\text{sph}} = \frac{k_B \sigma_T}{m_e c^2} \int n_e(r) T_e(r) dV \quad (\text{C.6})$$

$$= \frac{\sigma_T}{m_e c^2} \int P(r) dV \quad (\text{C.7})$$



Figure C.4: Picture of ACT. The height of the telescope is 12 m.

Note that in general deprojection of observed SZ profile is needed to calculate  $Y_{\text{sph}}$ , as its integrand is three-dimensional profile. For example, universal pressure profile derived by Arnaud et al. [7] is often used by recent works [53][82]. Similarly the density and temperature profile from X-ray observations can be used to guess SZ signals by using Eq. C.7[7].

## C.2 Atacama Cosmology Telescope

Atacama Cosmology Telescope (ACT) [94] is the project to measure small-scale CMB anisotropies and detect clusters of galaxies through the SZ effect. The picture of ACT is shown in Fig. C.4. The telescope is located at Cerro Toco in the Atacama Desert at an altitude of 5190 m to carry out observations with small atmospheric disturbance. In order to detect the SZ effect efficiently, observations are made in three frequencies (148 GHz, 218 GHz, 227 GHz) with a field of view of  $22' \times 26'$ . The telescope was commissioned in 2007, and started SZ survey from 2008.

A 6 m off-axis Gregorian telescope gathers millimeter wave from sky to a cryogenic camera called Millimeter Bolometer Array Camera (MBAC). The MBAC has three 1024 element ( $32 \times 32$ ) detector arrays. Each array is dedicated to one frequency. Detector spacing is  $\sim 40''$  in horizontal and  $\sim 50''$  in vertical. The bolometers are cooled down to  $\sim 500$  mK to obtain sensitivity enough to measure the SZ effect. The achieved sensitivities of 148 GHz, 218 GHz, and 277 GHz were  $\sim 31 \mu\text{K s}^{1/2}$ ,  $\sim 47 \mu\text{K s}^{1/2}$ , and  $\sim 191 \mu\text{K s}^{1/2}$ , respectively.

The achieved beam parameters are summarized in Table C.1, and as an example the observed Compton- $y$  parameter of ACTJ0022 is shown in Fig. C.5.

Frequency	148 GHz	218 GHz	277 GHz
Major FWHM(')	$1.401 \pm 0.003$	$1.012 \pm 0.001$	$0.891 \pm 0.04$
Minor FWHM(')	$1.336 \pm 0.001$	$0.991 \pm 0.001$	$0.858 \pm 0.005$
Axis angle( $^{\circ}$ )	$66 \pm 1$	$45 \pm 2$	$66 \pm 10$

Table C.1: Summary of beam parameters of ACT. This table is taken from Swetz et al. [94].

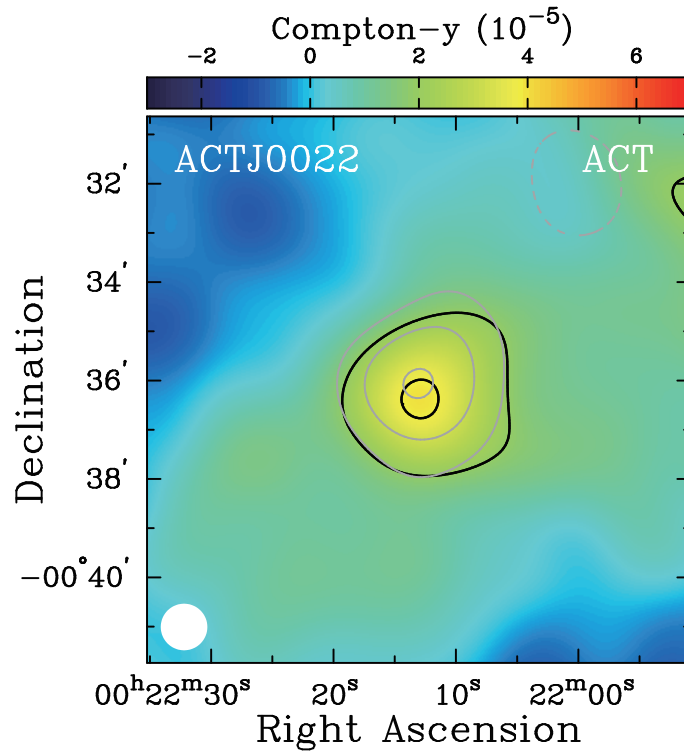


Figure C.5: The Compton- $y$  parameter observed by the ACT. This figure is taken from Reese et al. [82].

# Bibliography

- [1] <http://www.naoj.org/Observing/Telescope/index.html>.
- [2] K. N. Abazajian, et al. The Seventh Data Release of the Sloan Digital Sky Survey. *ApJS*, 182:543, 2009.
- [3] M. Abramowitz and I. A. Stegun. *Handbook of mathematical functions : with formulas, graphs, and mathematical tables*. 1970.
- [4] H. Aihara, et al. The Eighth Data Release of the Sloan Digital Sky Survey: First Data from SDSS-III. *ApJS*, 193:29, 2011.
- [5] C. Alard and R. H. Lupton. A Method for Optimal Image Subtraction. *ApJ*, 503:325, 1998.
- [6] K. Andersson, et al. X-Ray Properties of the First Sunyaev-Zel'dovich Effect Selected Galaxy Cluster Sample from the South Pole Telescope. *ApJ*, 738:48, 2011.
- [7] M. Arnaud, et al. The universal galaxy cluster pressure profile from a representative sample of nearby systems (REXCESS) and the  $Y_{SZ} - M_{500}$  relation. *A&A*, 517:A92, 2010.
- [8] S. Arnouts, et al. Measuring and modelling the redshift evolution of clustering: the Hubble Deep Field North. *MNRAS*, 310:540–556, 1999.
- [9] M. Bartelmann and P. Schneider. Weak gravitational lensing. *Phys. Rep.*, 340:291–472, 2001.
- [10] G. M. Bernstein and M. Jarvis. Shapes and Shears, Stars and Smears: Optimal Measurements for Weak Lensing. *AJ*, 123:583–618, 2002.
- [11] E. Bertin and S. Arnouts. SExtractor: Software for source extraction. *A&AS*, 117:393–404, 1996.
- [12] M. S. Bessell. UBVRI passbands. *PASP*, 102:1181–1199, 1990.

- [13] C. Bildfell, et al. Resurrecting the red from the dead: optical properties of BCGs in X-ray luminous clusters. *MNRAS*, 389:1637–1654, 2008.
- [14] J. Bosch. Galaxy Modeling with Compound Elliptical Shapelets. *AJ*, 140: 870–879, 2010.
- [15] S. Bridle, et al. Handbook for the GREAT08 Challenge: An image analysis competition for cosmological lensing. *Annals of Applied Statistics*, 3:6–37, 2009.
- [16] S. Bridle et al. Results of the GREAT08 Challenge: an image analysis competition for cosmological lensing. *MNRAS*, 405:2044–2061, 2010.
- [17] T. Broadhurst, et al. The Surprisingly Steep Mass Profile of A1689, from a Lensing Analysis of Subaru Images. *ApJ*, 619:L143–L146, 2005.
- [18] M. Brodwin, et al. SPT-CL J0546-5345: A Massive  $z>1$  Galaxy Cluster Selected Via the Sunyaev-Zel’dovich Effect with the South Pole Telescope. *ApJ*, 721:90–97, 2010.
- [19] J. A. Cardelli, et al. The relationship between infrared, optical, and ultraviolet extinction. *ApJ*, 345:245–256, 1989.
- [20] J. E. Carlstrom, et al. Cosmology with the Sunyaev-Zel’dovich Effect. *ARA&A*, 40:643–680, 2002.
- [21] J. E. Carlstrom, et al. The 10 Meter South Pole Telescope. *PASP*, 123: 568–581, 2011.
- [22] F. Castelli and R. L. Kurucz. New Grids of ATLAS9 Model Atmospheres. *ArXiv Astrophysics e-prints*, 2004.
- [23] D. Clowe, et al. Weak lensing mass reconstructions of the ESO Distant Cluster Survey. *A&A*, 451:395–408, 2006.
- [24] G. D. Coleman, et al. Colors and magnitudes predicted for high redshift galaxies. *ApJS*, 43:393–416, 1980.
- [25] A. W. J. Cousins. VRI Photometry of E and F Region Stars [errata: 1978MNSSA..37...35C, 1980MNSSA..39...32C]. *Monthly Notes of the Astronomical Society of South Africa*, 37:8–+, 1978.
- [26] A. R. Duffy, et al. Dark matter halo concentrations in the Wilkinson Microwave Anisotropy Probe year 5 cosmology. *MNRAS*, 390:L64–L68, 2008.

- [27] D. J. Eisenstein, et al. SDSS-III: Massive Spectroscopic Surveys of the Distant Universe, the Milky Way, and Extra-Solar Planetary Systems. *AJ*, 142:72, 2011.
- [28] J. W. Fowler, et al. Optical design of the Atacama Cosmology Telescope and the Millimeter Bolometric Array Camera. *Appl. Opt.*, 46:3444–3454, 2007.
- [29] D. L. Fried. Optical Resolution Through a Randomly Inhomogeneous Medium for Very Long and Very Short Exposures. *Journal of the Optical Society of America (1917-1983)*, 56:1372–+, 1966.
- [30] M. Fukugita, et al. The Sloan Digital Sky Survey Photometric System. *AJ*, 111:1748–+, 1996.
- [31] N. Hand, et al. The Atacama Cosmology Telescope: Detection of Sunyaev-Zel'Dovich Decrement in Groups and Clusters Associated with Luminous Red Galaxies. *ApJ*, 736:39, 2011.
- [32] C. M. Hirata, et al. Galaxy-galaxy weak lensing in the Sloan Digital Sky Survey: intrinsic alignments and shear calibration errors. *MNRAS*, 353:529–549, 2004.
- [33] O. Ilbert, et al. Accurate photometric redshifts for the CFHT legacy survey calibrated using the VIMOS VLT deep survey. *A&A*, 457:841–856, 2006.
- [34] O. Ilbert, et al. Cosmos Photometric Redshifts with 30-Bands for 2-deg<sup>2</sup>. *ApJ*, 690:1236–1249, 2009.
- [35] M. Iye, et al. Current Performance and On-Going Improvements of the 8.2 m Subaru Telescope. *PASJ*, 56:381–397, 2004.
- [36] M. J. Jee, et al. Scaling Relations and Overabundance of Massive Clusters at  $z > \sim 1$  from Weak-lensing Studies with the Hubble Space Telescope. *ApJ*, 737:59, 2011.
- [37] Y. P. Jing and Y. Suto. Triaxial Modeling of Halo Density Profiles with High-Resolution N-Body Simulations. *ApJ*, 574:538–553, 2002.
- [38] H. L. Johnson and W. W. Morgan. Fundamental stellar photometry for standards of spectral type on the revised system of the Yerkes spectral atlas. *ApJ*, 117:313–+, 1953.
- [39] I. T. Jolliffe. *Principal component analysis*. 1986.

- [40] N. Kaiser, et al. A Method for Weak Lensing Observations. *ApJ*, 449:460, 1995.
- [41] Y. Kamata, et al. Evaluation of the fully-depleted back-illuminated CCD for Subaru Suprime-Cam. In *Society of Photo-Optical Instrumentation Engineers (SPIE) Conference Series*, volume 7021 of *Society of Photo-Optical Instrumentation Engineers (SPIE) Conference Series*, 2008.
- [42] Yukiko Kamata, et al. Characterization and performance of hyper suprimecam ccd. volume 7742, page 774229. SPIE, 2010. URL <http://link.aip.org/link/?PSI/7742/774229/1>.
- [43] R. C. Kennicutt, Jr. A spectrophotometric atlas of galaxies. *ApJS*, 79:255–284, 1992.
- [44] R. Kessler, et al. First-Year Sloan Digital Sky Survey-II Supernova Results: Hubble Diagram and Cosmological Parameters. *ApJS*, 185:32–84, 2009.
- [45] T. Kitayama and Y. Suto. Constraints on the Fluctuation Amplitude and Density Parameter from X-Ray Cluster Number Counts. *ApJ*, 490:557, 1997.
- [46] B. P. Koester, et al. A MaxBCG Catalog of 13,823 Galaxy Clusters from the Sloan Digital Sky Survey. *ApJ*, 660:239–255, 2007.
- [47] E. Komatsu, et al. Seven-year Wilkinson Microwave Anisotropy Probe (WMAP) Observations: Cosmological Interpretation. *ApJS*, 192:18, 2011.
- [48] Y. Komiyama, et al. Hyper Suprime-Cam: camera design. In *Society of Photo-Optical Instrumentation Engineers (SPIE) Conference Series*, volume 7735 of *Society of Photo-Optical Instrumentation Engineers (SPIE) Conference Series*, 2010.
- [49] D. Larson, et al. Seven-year Wilkinson Microwave Anisotropy Probe (WMAP) Observations: Power Spectra and WMAP-derived Parameters. *ApJS*, 192:16, 2011.
- [50] G. A. Luppino and N. Kaiser. Detection of Weak Lensing by a Cluster of Galaxies at  $Z = 0.83$ . *ApJ*, 475:20, 1997.
- [51] K. Madsen, et al. *Methods for non-linear least squares problems, 2nd edition*. 2004.
- [52] T. A. Marriage, et al. The Atacama Cosmology Telescope: Sunyaev-Zel’dovich-Selected Galaxy Clusters at 148 GHz in the 2008 Survey. *ApJ*, 737:61, 2011.

- [53] D. P. Marrone, et al. LoCuSS: The Sunyaev-Zel'dovich Effect and Weak Lensing Mass Scaling Relation. *ArXiv e-prints*, 2011.
- [54] R. Massey and A. Refregier. Polar shapelets. *MNRAS*, 363:197–210, 2005.
- [55] R. Massey et al. The Shear Testing Programme 2: Factors affecting high-precision weak-lensing analyses. *MNRAS*, 376:13–38, 2007.
- [56] P. Melchior, et al. Limitations on shapelet-based weak-lensing measurements. *A&A*, 510:A75+, 2010.
- [57] F. Menanteau, et al. Southern Cosmology Survey. II. Massive Optically Selected Clusters from 70 Square Degrees of the Sunyaev-Zel'dovich Effect Common Survey Area. *ApJS*, 191:340–351, 2010.
- [58] F. Menanteau, et al. The Atacama Cosmology Telescope: ACT-CL J0102-4915 "El Gordo," a Massive Merging Cluster at Redshift 0.87. *ArXiv e-prints*, 2011.
- [59] J. Miralda-Escude. The correlation function of galaxy ellipticities produced by gravitational lensing. *ApJ*, 380:1–8, 1991.
- [60] S. Miyazaki, et al. Subaru Prime Focus Camera – Suprime-Cam. *PASJ*, 54: 833–853, 2002.
- [61] A. F. J. Moffat. A Theoretical Investigation of Focal Stellar Images in the Photographic Emulsion and Application to Photographic Photometry. *A&A*, 3:455–+, 1969.
- [62] M. J. Mortonson, et al. Simultaneous falsification of  $\Lambda$ CDM and quintessence with massive, distant clusters. *Phys. Rev. D*, 83(2):023015, 2011.
- [63] T. Mroczkowski. A New Approach to Obtaining Cluster Mass from Sunyaev-Zel'dovich Effect Observations. *ApJ*, 728:L35, 2011.
- [64] R. Nakajima and G. Bernstein. Shear Recovery Accuracy in Weak-Lensing Analysis with the Elliptical Gauss-Laguerre Method. *AJ*, 133:1763–1779, 2007.
- [65] T. T. Nakamura and Y. Suto. Strong Gravitational Lensing and Velocity Function as Tools to Probe Cosmological Parameters — Current Constraints and Future Predictions —. *Progress of Theoretical Physics*, 97:49, 1997.
- [66] H. Nakaya, et al. New Focal Plane Array Controller for the Instruments of the Subaru Telescope. *PASP*, 118:478–488, 2006.

- [67] H. Nakaya, et al. Hyper Suprime-Cam: CCD readout electronics. In *Society of Photo-Optical Instrumentation Engineers (SPIE) Conference Series*, volume 7014 of *Society of Photo-Optical Instrumentation Engineers (SPIE) Conference Series*, 2008.
- [68] J. F. Navarro, et al. The Structure of Cold Dark Matter Halos. *ApJ*, 462:563, 1996.
- [69] M. D. Niemack, et al. ACTPol: a polarization-sensitive receiver for the Atacama Cosmology Telescope. In *Society of Photo-Optical Instrumentation Engineers (SPIE) Conference Series*, volume 7741 of *Society of Photo-Optical Instrumentation Engineers (SPIE) Conference Series*, 2010.
- [70] A. J. Nishizawa, et al. A Clipping Method to Mitigate the Impact of Catastrophic Photometric Redshift Errors on Weak Lensing Tomography. *ApJ*, 718:1252–1265, 2010.
- [71] C. Oaxaca Wright and T. G. Brainerd. Gravitational Lensing by NFW Halos. *ArXiv Astrophysics e-prints*, 1999.
- [72] J. E. O’Donnell.  $R_{nu}$ -dependent optical and near-ultraviolet extinction. *ApJ*, 422:158–163, 1994.
- [73] M. Oguri and M. Takada. Combining cluster observables and stacked weak lensing to probe dark energy: Self-calibration of systematic uncertainties. *Phys. Rev. D*, 83(2):023008, 2011.
- [74] M. Oguri, et al. Can the Steep Mass Profile of A1689 Be Explained by a Triaxial Dark Halo? *ApJ*, 632:841–846, 2005.
- [75] M. Oguri, et al. Combined strong and weak lensing analysis of 28 clusters from the Sloan Giant Arcs Survey. *MNRAS*, page 2189, 2012.
- [76] N. Okabe, et al. LoCuSS: Subaru Weak Lensing Study of 30 Galaxy Clusters. *PASJ*, 62:811–, 2010.
- [77] W. J. Percival, et al. Measuring the Baryon Acoustic Oscillation scale using the Sloan Digital Sky Survey and 2dF Galaxy Redshift Survey. *MNRAS*, 381:1053–1066, 2007.
- [78] W. J. Percival, et al. Baryon acoustic oscillations in the Sloan Digital Sky Survey Data Release 7 galaxy sample. *MNRAS*, 401:2148–2168, 2010.
- [79] S. Perlmutter, et al. Measurements of Omega and Lambda from 42 High-Redshift Supernovae. *ApJ*, 517:565–586, 1999.

- [80] W. H. Press and P. Schechter. Formation of Galaxies and Clusters of Galaxies by Self-Similar Gravitational Condensation. *ApJ*, 187:425–438, 1974.
- [81] R. Racine. The Telescope Point Spread Function. *PASP*, 108:699–+, 1996.
- [82] E. D. Reese, et al. The Atacama Cosmology Telescope: High-Resolution Sunyaev-Zel’dovich Array Observations of ACT SZE-selected Clusters from the Equatorial Strip. *ArXiv e-prints*, 2011.
- [83] A. Refregier. Shapelets - I. A method for image analysis. *MNRAS*, 338:35–47, 2003.
- [84] A. G. Riess, et al. Observational Evidence from Supernovae for an Accelerating Universe and a Cosmological Constant. *AJ*, 116:1009–1038, 1998.
- [85] A. G. Riess, et al. A Redetermination of the Hubble Constant with the Hubble Space Telescope from a Differential Distance Ladder. *ApJ*, 699:539–563, 2009.
- [86] E. Rozo, et al. Constraining the Scatter in the Mass-richness Relation of maxBCG Clusters with Weak Lensing and X-ray Data. *ApJ*, 699:768–781, 2009.
- [87] D. J. Schlegel, et al. Maps of Dust Infrared Emission for Use in Estimation of Reddening and Cosmic Microwave Background Radiation Foregrounds. *ApJ*, 500:525–+, 1998.
- [88] N. Sehgal, et al. The Atacama Cosmology Telescope: Cosmology from Galaxy Clusters Detected via the Sunyaev-Zel’dovich Effect. *ApJ*, 732:44, 2011.
- [89] R. E. Smith, et al. Stable clustering, the halo model and non-linear cosmological power spectra. *MNRAS*, 341:1311–1332, 2003.
- [90] G. F. Smoot, et al. Structure in the COBE differential microwave radiometer first-year maps. *ApJ*, 396:L1–L5, 1992.
- [91] D. N. Spergel, et al. First-Year Wilkinson Microwave Anisotropy Probe (WMAP) Observations: Determination of Cosmological Parameters. *ApJS*, 148:175–194, 2003.
- [92] J. P. Stott, et al. The XMM Cluster Survey: The Build-up of Stellar Mass in Brightest Cluster Galaxies at High Redshift. *ApJ*, 718:23–30, 2010.
- [93] R. A. Sunyaev and Y. B. Zeldovich. The Observations of Relic Radiation as a Test of the Nature of X-Ray Radiation from the Clusters of Galaxies. *Comments on Astrophysics and Space Physics*, 4:173, 1972.

- [94] D. S. Swetz, et al. Overview of the Atacama Cosmology Telescope: Receiver, Instrumentation, and Telescope Systems. *ApJS*, 194:41, 2011.
- [95] J. Tinker, et al. Toward a Halo Mass Function for Precision Cosmology: The Limits of Universality. *ApJ*, 688:709–728, 2008.
- [96] K. Umetsu and T. Futamase. Detection of Dark Matter Concentrations in the Field of Cl 1604+4304 from Weak Lensing Analysis. *ApJ*, 539:L5–L8, 2000.
- [97] F. C. van den Bosch, et al. The phase-space parameters of the brightest halo galaxies. *MNRAS*, 361:1203–1215, 2005.
- [98] A. Vikhlinin, et al. Chandra Sample of Nearby Relaxed Galaxy Clusters: Mass, Gas Fraction, and Mass-Temperature Relation. *ApJ*, 640:691–709, 2006.
- [99] A. Vikhlinin, et al. Chandra Cluster Cosmology Project III: Cosmological Parameter Constraints. *ApJ*, 692:1060–1074, 2009.
- [100] G. M. Voit. Tracing cosmic evolution with clusters of galaxies. *Reviews of Modern Physics*, 77:207–258, 2005.
- [101] R. Williamson, et al. A Sunyaev-Zel’dovich-selected Sample of the Most Massive Galaxy Clusters in the 2500 deg<sup>2</sup> South Pole Telescope Survey. *ApJ*, 738:139, 2011.
- [102] Y. B. Zeldovich and R. A. Sunyaev. The Interaction of Matter and Radiation in a Hot-Model Universe. *Ap&SS*, 4:301–316, 1969.